LATERAL ANALYSIS OF GAS REINJECTION COMPRESSORS WITH UNCERTAINTIES ON BEARINGS COEFFICIENTS

Raphael Nascimento Cisneiros

Dissertação de Mestrado apresentada ao Programa de Pós-graduação em Engenharia Mecânica, COPPE, da Universidade Federal do Rio de Janeiro, como parte dos requisitos necessários à obtenção do título de Mestre em Engenharia Mecânica.

Orientador: Thiago Gamboa Ritto

Rio de Janeiro
Maio de 2019

LATERAL ANALYSIS OF GAS REINJECTION COMPRESSORS WITH UNCERTAINTIES ON BEARINGS COEFFICIENTS

Raphael Nascimento Cisneiros

DISSERTAÇÃO SUBMETIDA AO CORPO DOCENTE DO INSTITUTO ALBERTO LUIZ COIMBRA DE PÓS-GRADUAÇÃO E PESQUISA DE ENGENHARIA (COPPE) DA UNIVERSIDADE FEDERAL DO RIO DE JANEIRO COMO PARTE DOS REQUISITOS NECESSÁRIOS PARA A OBTENÇÃO DO GRAU DE MESTRE EM CIÊNCIAS EM ENGENHARIA MECÂNICA.

Examinada por:

Prof. Thiago Gamboa Ritto, D.Sc.

Prof. Fernando Augusto de Noronha Castro Pinto, Dr.-Ing.

Prof. Helio Fiori de Castro, D.Sc.

RIO DE JANEIRO, RJ – BRASIL
MAIO DE 2019

Cisneiros, Raphael Nascimento

Lateral analysis of Gas Reinjection Compressors with Uncertainties on Bearings Coefficients/Raphael Nascimento Cisneiros. – Rio de Janeiro: UFRJ/COPPE, 2019.

XVI, 130 p.: il.; 29, 7cm.

Orientador: Thiago Gamboa Ritto

Dissertação (mestrado) – UFRJ/COPPE/Programa de Engenharia Mecânica, 2019.

Referências Bibliográficas: p. 110 – 112.

1. compressor. 2. rotordynamics. 3. uncertanties. 4. reliability. I. Ritto, Thiago Gamboa. II. Universidade Federal do Rio de Janeiro, COPPE, Programa de Engenharia Mecânica. III. Título.

Agradecimentos

Gostaria de agradecer a muitas pessoas que fizeram parte da minha caminhada para a conclusão do mestrado.

Primeiramente, ao meu orientador Thiago Ritto que sempre me motivou, sinalizou caminhos e sempre foi crítico de uma forma muito construtiva.

Também gostaria de agradecer ao meu antigo gerente Davi Teves que viabilizou meu ingresso no mestrado. Da mesma forma também agradeço ao meu gestor atual Cláudio Carvalho que me recebeu muito bem e compreendeu a importância do mestrado para agregar conhecimento ao trabalho.

Gostaria de agradecer a alguns colegas como Raphael Timbó que sempre foi prestativo e simpático me ajudando com informações importantes para a realização da minha dissertação de mestrado, assim como Leonardo Valero, Camila Gomes e Thiago Apolinário pelo companheirismo e parceria durante a etapa das disciplinas.

Agradeço a meu pai (in memoriam) pelo amor e pela confiança depositada em mim mesmo ainda muito criança e até pela minha escolha de cursar Engenharia Mecânica pois eu sabia da sua admiração por essa profissão.

Agradeço a meu avô Cláudio (in memoriam) que sempre foi como um segundo pai para mim e a minha avó Maria de Lourdes.

Agradeço a minha mãe pelo amor incondicional dado a mim e aos meus irmãos e pela inspiração que sempre foi pelo seu exemplo. Através das suas batalhas pessoais e da decisão do retorno a sua profissão de medicina me mostrou dentre tantas coisas que a resiliência, o estudo e o conhecimento são o caminho para a busca da realização profissional.

Agradeço aos meus irmãos e parceiros Caio, Túlio, Caio George, Rafael Lima e Franklin pela amizade e companheirismo de uma vida e durante essa caminhada acadêmica também assim como meus demais amigos.

Por fim, a minha companheira Ana Paula que mais do que ninguém sabe a dedicação que empenhei entre o trabalho e os estudos e que abdicou da minha companhia incontáveis vezes, absorveu as demandas da casa, evitou dividir suas preocupações diárias de forma unilateral para que eu não perdesse o foco, me apoiando de forma irrestrita durantes esses três anos de mestrado e sempre com muito amor, compreensão e afeto.

Resumo da Dissertação apresentada à COPPE/UFRJ como parte dos requisitos necessários para a obtenção do grau de Mestre em Ciências (M.Sc.)

ANÁLISE LATERAL DE COMPRESSORES DE REINJEÇÃO DE GÁS COM INCERTEZAS NOS COEFICIENTES DOS MANCAIS

Raphael Nascimento Cisneiros

Maio/2019

Orientador: Thiago Gamboa Ritto

Programa: Engenharia Mecânica

Os mancais "tilting pad" adicionam rigidez e são a maior fonte de amortecimento para um sistema rotor-impelidor-mancal. Os coeficientes de rigidez e amortecimento dos mancais possuem incertezas que impactam no projeto mecânico destas máquinas. Esta dissertação se propõe ao estudo de dois compressores projetados para reinjeção de gás em reservatórios de petróleo. Um modelo estocástico foi construído para simular o comportamento rotodinâmico e um modelo Termo-Elasto-Hidroddinâmico foi utilizado para os mancais com um nível de incerteza associado ao cálculo dos seus coeficientes. O modelo estocástico proporciona uma ferramenta aplicável a indústria para prever a confiabilidade da máquina numa fase anterior a sua fabricação e portanto evitar os custos de fabricação de máquinas cujos testes possam ser rejeitados e que sua vida útil não seja comprometida. Para tal, diferentes cenários de desbalanceamento das máquinas foram criados compatíveis com o ciclo de vida numa plataforma de petróleo. As normas da API (American Petroleum Institute) foram utilizadas como critérios de aceitação da rotodinâmica dos compressores. Por fim, os métodos de confiabilidade FORM e Importance Sampling foram utilizados para avaliar os diferentes cenários apresentados às máquinas para a estimativa da probabilidade de não atendimento aos critérios da API 617 [4] e para redução do tempo computacional.

Abstract of Dissertation presented to COPPE/UFRJ as a partial fulfillment of the requirements for the degree of Master of Science (M.Sc.)

LATERAL ANALYSIS OF GAS REINJECTION COMPRESSORS WITH UNCERTAINTIES ON BEARINGS COEFFICIENTS

Raphael Nascimento Cisneiros

May/2019

Advisor: Thiago Gamboa Ritto

Department: Mechanical Engineering

The tilting pad bearings add stiffness and are the main source of damping to a rotor-impeller-bearing system. The bearing stiffness and damping coefficients have uncertanties which impacts on these machines mechanical integrity design. This thesis studies two compressors used in gas reinjection at oil reservoirs. An stochastic model is constructed to simulate the compressors rotor dynamic behavior and a Thermo-Elasto-Hydrodynamic model is applied to the tilting pad bearings with a level of uncertanties related to the coefficients calculation. These stochastic models provide the industry a useful tool to antecipate whether the machine is reliable to be manufactured and therefore to avoid the costs of unsucessfull factory acceptance tests and the machine life cycle will not be compromised. Hence, some scenarios of unbalance magnitudes were built according to a variety of severity levels feasible in oil and gas industry. The API (American Petroluem institute) standards are used as rotordynamic acceptance criteria. The reliability methods, First-Order Reliability Method and Importance Sampling, are used to evaluate these machines different scenarios in the calculation of the probability of not meeting API 617 [4] criteria and to save computational effort.

Contents

List of Figures

List of Tables

List of Abbreviations

AF	Amplification Factor, p. 8, 10
A_{max}	Maximum Probe Response Amplitude Over The Range of N_{ma} to N_{mc}, p. 10
A_{v_1}	Mechanical Vibration Test Limit, p. 10, 11, 37, 40, 42, 45, 47, 49, 59, 81
C_v	Coefficient of Variation, p. 35, 40, 42, 45, 64, 83, 86, 90, 93
N_{ma}	Minimum Allowable Speed, p. 9–11, 37, 39, 42, 45, 47, 81
N_{mc}	Maximum Continuous Speed, p. 7, 9, 11, 35
SM_a	Actual Separation Margin Between Operational Speed and Critical Speed, p. 8, 9, 35, 40, 81
SM_r	Separation margin required between operational speed and critical speed, p. 9
SM_r	Separation margin required between operational speed and critical speed , p. 8, 10, 35, 81
S_{cc}	Scale Factor for Close Clearance Check, p. 11, 104
U_a	Input Unbalance, p. 8
U_r	Maximum Allowable Residual Unbalance, p. 7, 8, 96
β	Safety index, p. 62, 69, 71
ε_{LOO}	Leave-One-Out Cross-Validation Error, p. 78, 81, 84, 88, 91
CDF	Cumulative Distribution Function, p. 65, 67
DE	Drive-End side, p. 29, 45
FORM	First-Order Reliability Method, p. 65, 69, 73, 74, 81–83, 85–87, 90, 92, 94, 95, 98, 99, 102

IS	Importance Sampling, p. 72, 82, 86, 90, 93, 98, 102
MPP	Most Probable Point, p. 69, 76
NDE	Non-Drive-End side, p. 29
PCE	Polynomial Chaos Expansion, p. 77, 81, 84, 88, 91
PDF	Probability Density Function, p. 27, 32, 35, 42, 47, 49, 57, 66, 69, 96, 104
TEHD	Thermo-Elasto-Hydrodynamic, p. 19, 22, 23, 30, 50

Chapter 1

Introduction

1.1 Motivation

The world energy increasing demand led the oil and gas industry to offshore production. The Brazilian offshore production is growing in the last few years due to pre-salt reservoirs which have a high content of gas. The oil and gas industry avoids to burn the gas as the world environmental concerns have grown in the last few decades. Some of the gas meets market demands which imply on transportation and refinement. The reinjection into the reservoir is another available possibility. Gas reinjection leads to an increase in oil wells production and therefore has been a solution for many offshore applications. The gas produced needs to achieve a high-pressure level for reinjection purposes.

The centrifugal compressors for these applications require high speeds for slender shafts which affect the lateral vibration. The compressor design, according to API 617 [4] standard, requires a lateral analysis, which basically is the evaluation of the machine lateral critical speeds and the rotor unbalance response. The compressor model accounts for bearing parameters, stiffness, and damping. The bearing models have uncertainties that rely on turbulence effects, heat transfer hypothesis, dimension simplifications, which are likely to influence the compressor rotordynamic design conformity to oil and gas standards. For instance, the operational speed margin to critical speed and the vibration limit.

1.2 Dissertation goals

The dissertation goals are to build a model of lateral rotor vibration, compare the response of two different gas reinjection compressors with uncertainties on bearings coefficients, investigate whether these uncertainties impact on rotordynamic design acceptance criteria according to API 617 [4] requirements and then apply reliability

methods to compute the probability of not achieving a given criterion.

The First Order Reliability Method and Importance Sampling are the reliability methods selected to evaluate the compressors probability of failure, i.e., not meeting API 617 [4] criteria.

1.3 Centrifugal compressors

Centrifugal compressor was a French invention. Late 19^{th} century Professor Auguste Rateau tested a single stage prototype which became the first of this turbomachinery conception. The equipment compressed $0.5m^3/s$ of atmospheric air to a discharge pressure of 1.5bar (LÜDTKE [1]).

Nowadays some applications to single shaft centrifugal compressors are:

- Petroleum refining: hydrotreating, hydrocracking.
- Petro-chemical processing: ammonia syngas, methanol syngas, NH_3 refrigeration, ethylene, urea.
- Gas field operations: gas lift, gas reinjection.
- Chemical industries: chlorine.

Gas reinjection into oil reservoir usually demands higher discharge pressures than other applications; therefore, tends to be more critical during operation. Typically, from 300 up to 600 bar.

Figure 1.1 shows the aerodynamically active components of a single-shaft compressor. The suction of the gas is through nozzle A; the flow accelerates in plenum inlet B; the impeller C transfers mechanical energy to the gas which means an increase of pressure, temperature, and velocity; flow deceleration occurs in the diffuser D which results in an increase of pressure and temperature. Figure 1.1 shows a side-stream J between two stages with an additional suction nozzle H which depends on the compressor design. At the end, a volute K, a flow channel whose area increases along the circumference in the direction of rotation, is followed by a conical exit diffuser L. The diffuser is the last component where the gas is subjected to a pressure increase. The final component is the discharge nozzle M.

The impellers arrangements are either inline or back-to-back. The most simple one is ordering the components in one section along the flow path with the inlet nozzle and discharge nozzle on opposite sides. Figure 1.2 shows the described inline compressor. For compressors with more than two sections it is possible to reduce resultant axial thrust with a back-to-back impellers arrangement. Figure 1.3 shows this type of turbomachinery.

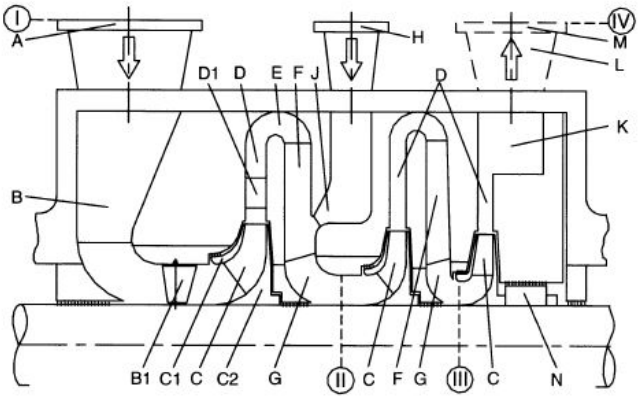

Figure 1.1: Compressor aerodynamics components LÜDTKE [1].

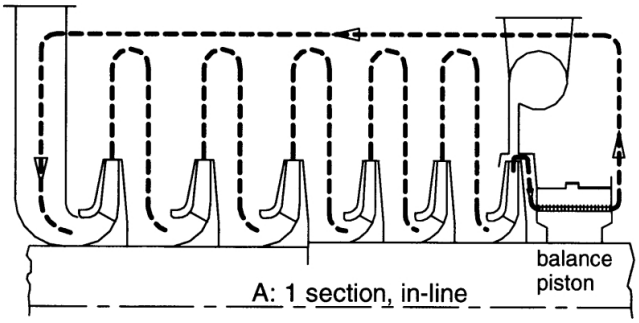

Figure 1.2: Inline compressor LÜDTKE [1].

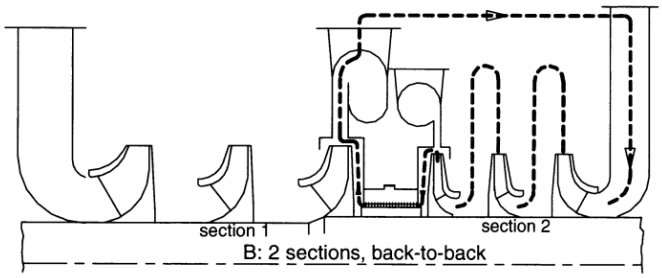

Figure 1.3: Back-to-back compressor LÜDTKE [1].

1.4 Tilting pad bearings

An essential component of a rotordynamic analysis is the bearing. For centrifugal compressors, fluid film bearings usually support radial and axial loads. Tilting pad journal bearing shown in fig. 1.4 are fluid film bearings whose state-of-the-art design has advanced tremendously in the last 60 years (API 684 [3]).

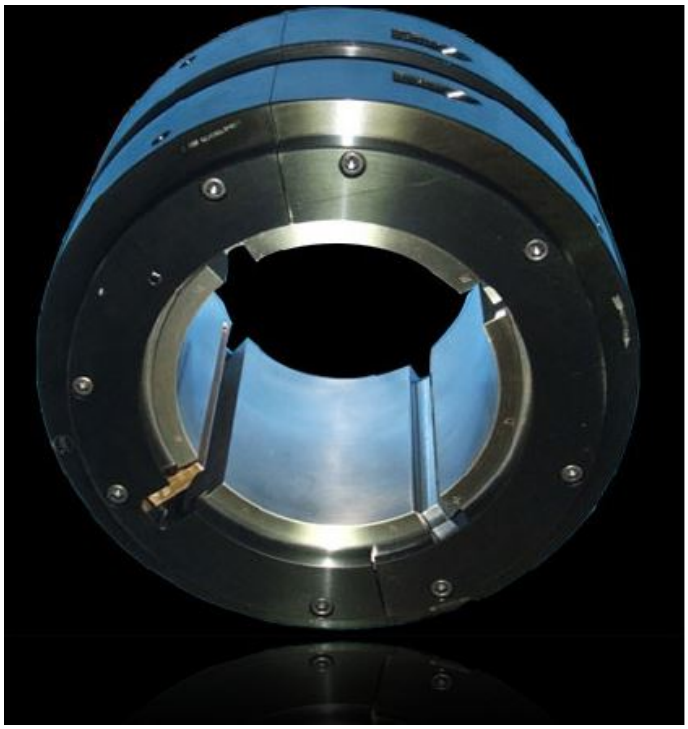

Figure 1.4: Tilting pad bearing DIMOND [2].

One advantage of tilting pad bearings to fixed geometry bearings is the more distributed pressure profile with the pads which decreases cross-coupled terms and yields superior stability characteristics. The many design parameters to change dynamic characteristics such as pad load orientation, pivot offset, pad preload, and pad axial length are a great advantage as well.

Figure 1.5 illustrates pad load orientation, pad preload, and pivot offset $\alpha = \phi_p/\chi$, where ϕ_p is the arc length from the pad leading edge to the pivot, and χ is the pad arc length.

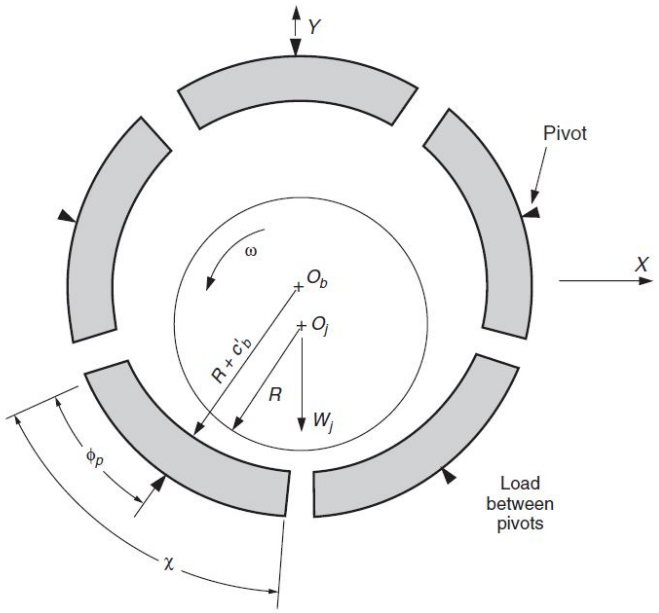

Figure 1.5: Five-pad tilting pad bearing schematic API 684 [3].

The pad preload is defined by

$$m = 1 - \left(\frac{c_b}{c_p}\right) \tag{1.1}$$

where c_b is the assembled bearing clearance and c_p, pad clearance, as shown by fig. 1.6. This figure shows O_p as the pad geometric center, O_j the journal geometric center, R_p the pad radius and R_b the bearing radius as well.

These parameters help to provide different dynamic behavior. For instance, directing the load between pivot implies more symmetric stiffness coefficients. However, asymmetry associated with the load on the pivot configuration provides superior stability. Another parameter discussed is pivot offset which is centrally pivoted when $\alpha = 0.5$. Offset pivots increase bearing stiffness and film thickness. However, large offsets decrease operating film temperatures.

Notice that zero preload occurs when pad clearance equals the assembled bearing clearance. Pad preload arises when pad and journal centers do not coincide. Usually, pad preload varies from 0% to 50%. Reducing preload over these range increases bearing damping whereas bearing stiffness remains practically constant. For a decreasing bearing assembled clearance with constant preload, both bearing stiffness and damping increase. However, a more rigid bearing reduces the effectiveness of shaft damping. Figure 1.7 shows the relation between preload, bearing clearance, stiffness, and damping discussed.

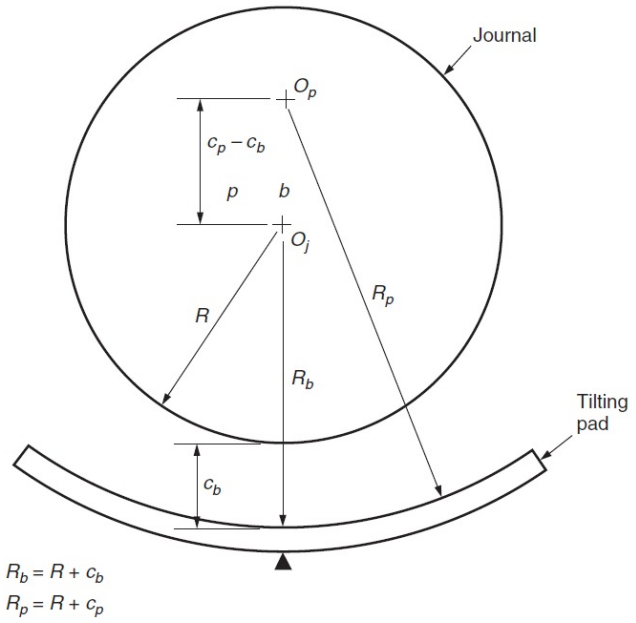

Figure 1.6: Preloaded pad API 684 [3].

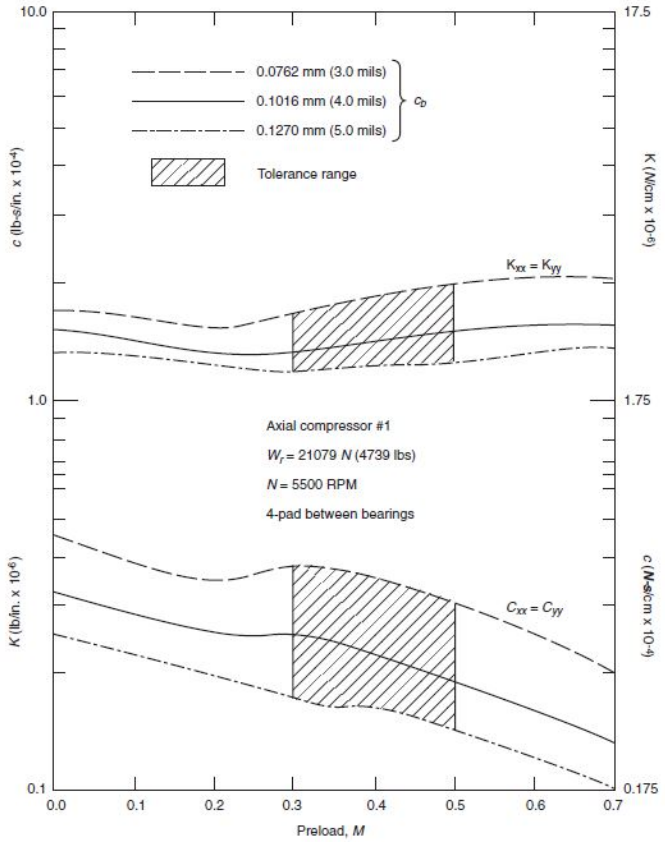

Figure 1.7: Stiffness and damping vs. preload and bearing clearance API 684 [3].

1.5 Uncertanties on bearing coefficients

Some experimental verification was carried out to estimate how accurate the bearing models were developed over the years. DMOCHOWSKI and BROCKWELL [8] considered a 76mm diameter 5-pad tilting pad bearing. They concluded that bearing coefficients measured presented an error in the range of ±5% to ±11% for stiffness and a range of ±5% to ±17% for damping.

WYGANT *et al.* [9] presented measured dynamic coefficients for a 70mm diameter 5-pad tilting pad. For "rocker-back" and "spherical seated" pad pivots test results lead to uncertainty levels ranging from 8% to 45% for the translational stiffness and 6% to 82% for the translational damping.

Chapter 2

Lateral analysis criteria

The lateral analysis detailed by API 617 [4] may be divided into two parts:

1. Undamped analysis
2. Damped unbalance rotor response analysis

The first analysis identifies the undamped critical speeds and determines their mode shapes.

After the identification of the mode shapes the analyst shall lead a damped unbalance response within 0 to 150% of the maximum continuous speed, N_{mc}. The unbalance shall be located based on the mode shapes determined by the undamped analysis. For instance, in between bearing machines whose mode shapes correspond to those represented by fig. 2.1 the imbalance locates at mid-span to excite the first bending mode and close to each bearing in the anti-node to excite the second bending mode. The unbalance magnitude shall be two times the maximum allowable residual unbalance, U_r (g-mm), which depends on journal static load W (kg) and Maximum Continuous Speed N_{mc} (rpm).

$$U_r = 6350\frac{W}{N_{mc}} \tag{2.1}$$

where 6350 is in $\left[\frac{\text{g-mm-rpm}}{\text{kg}}\right]$ unit.

According to API 617 [4], every machine shall have a permissible residual unbalance since a zero out-of-balance is not physically applicable. The higher operational speed of machines is, the higher the shaft vibrations will be due to unbalance forces. However, the higher rotor mass is for constant unbalance forces, the lower the vibrations are, and therefore the permissible residual unbalance can reach higher levels. Hence, users and manufacturers developed balance grades, i.e., residual unbalance tolerances that respect balance machines sensitivity which ranges from 5 μm to 10 μm (API 684 [3]). The fifth edition of API 617 [4] proposed this residual unbalance criterion and is still valid to machines up to 25000 rpm. Throughout the last

decades, the compressors increased the shaft speeds whereas the balance machines capabilities increased, in agreement with eq. (2.1).

Centrifugal compressor permissible tolerance is equivalent to 0.7 G (API 684 [3]) in ISO standards. ISO 21940-11 [10] defines the balance grade as $G = e_{perm}\Omega$ where e_{perm} (mm) is the permissible mass eccentricity, and Ω (rad/s) the shaft speed. For instance, 0.7 (mm/s) designates a G 0.7 balance quality grade. Then, the compressor balance grade of G 0.7 multiplied by journal static load W (kg), divided by shaft speed Ω (rpm) and considerations of unit conversion factors leads to eq. (2.1). Notice that fig. 2.1 first bending mode shows the input unbalance U_a as twice Maximum Allowable Residual Unbalance U_r (oz-in) for the rotor mass W in lbm which yields $U_a(\text{g-mm}) = 2 \times 6350W(\text{kg})/N_{mc}(\text{rpm})$ in previous units.

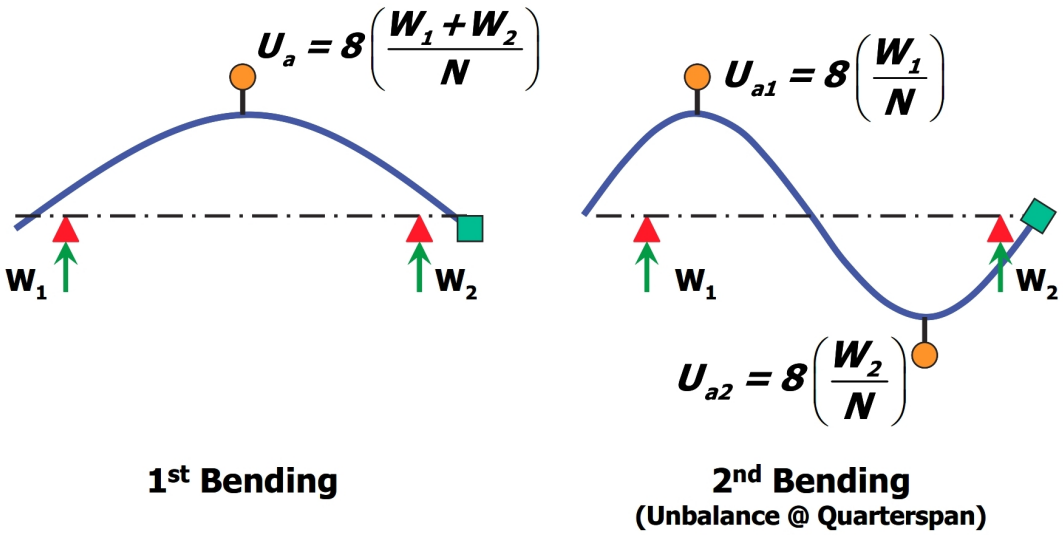

Figure 2.1: Typical mode shapes and corresponding unbalance API 617 [4].

2.1 API acceptance criteria

The rotodynamic acceptance criteria are the requirements to be met in a damped unbalance rotor response analysis. The requirements play an important role in preventing the machine from catastrophic failure during the equipment life cycle. In this section, the three criteria with regards to this analysis will be presented.

1. The damped unbalanced response analysis shall indicate that the machine meets the following requirement: $SM_a \geq SM_r$, i.e., a separation margin (SM) from critical speed to operational speed shall be established.

   The margin requirement depends on how much the structure is excited at a particular critical speed, N_c. This concept is enlightened with regards to the Amplification Factor, AF, given by

$$AF = \frac{N_c}{N_2 - N_1} \tag{2.2}$$

Notice that N_2 and N_1 define the bandwidth which is the frequency range for a "$\sqrt{2}$" decrease of vibration amplitude on a particular critical speed (MEIROVITCH [11]).

Figure 2.2 illustrates separation margin requirement for critical speeds over the operating speed range, e.g., S_{a1} is the actual separation margin from the first critical.

For a critical speed lower than operating speed range , SM_a yields:

$$SM_a(\%) = 100 \times \frac{N_{ma} - N_c}{N_{ma}} \tag{2.3}$$

where N_{ma} is the minimum allowable speed and N_c the critical speed.

When the critical speed is above operating speed range , SM_a yields:

$$SM_a(\%) = 100 \times \frac{N_c - N_{mc}}{N_{mc}} \tag{2.4}$$

where N_{mc} is the maximum continuos speed.

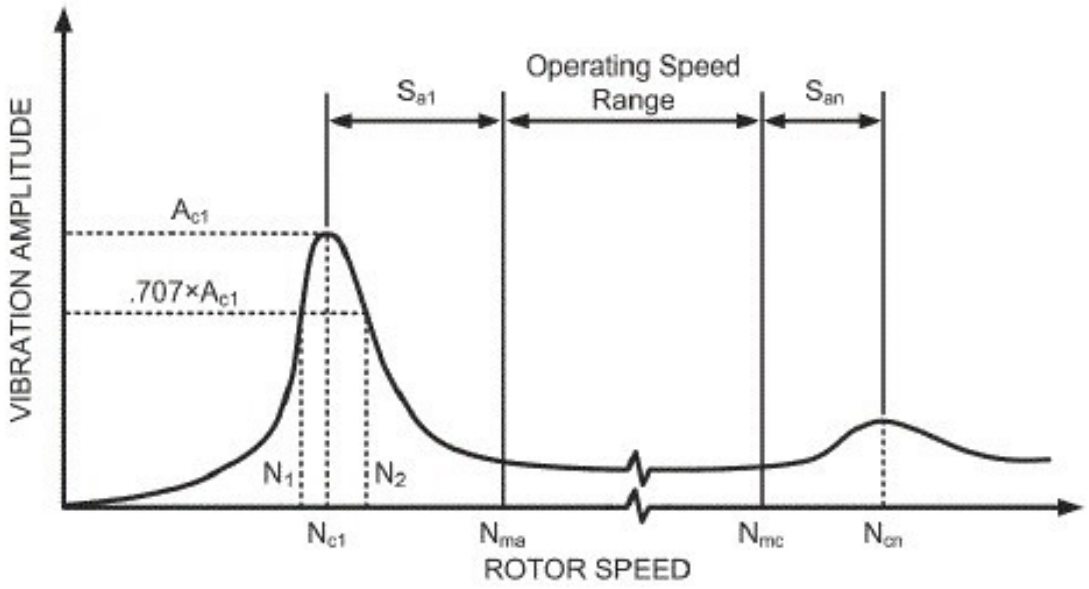

Figure 2.2: Separation margin requirement API 617 [4].

The required separation margin (SM_r) to operational speed is empirical and based on the experience of manufacturers and owners of compressors in the oil

and gas industry. Nonetheless, it is possible to understand the physical meaning of each equation and assume specific values of the Amplification Factor (AF) to illustrate it.

If AF at a particular critical speed is greater than or equal to 2.5 and that critical speed is below minimum allowable speed, N_{ma}, the required separation margin, SM_r, is given by

$$SM_r = 17\left(1 - \frac{1}{AF - 1.5}\right) \tag{2.5}$$

If AF is still greater or equal to 2.5 and that critical speed is above maximum continuous speed, N_{mc}, the required separation margin, SM_r, yields

$$SM_r = 10 + 17\left(1 - \frac{1}{AF - 1.5}\right) \tag{2.6}$$

Otherwise, for lower AF than 2.5 there is no separation margin requirement and the rotor is considered critically damped.

Notice that eq. (2.5) defines separation margin up to 17%, and eq. (2.6) up to 27% with lower damped critical speed along with higher separation margin. The second critical is usually associated with higher responses and therefore, requires an increased separation margin. At the lower limit, for AF close to 2.5, there is no required separation margin in eq. (2.5), and for eq. (2.6) the required separation margin is above 10%. In summary, for noncritically damped and flexible rotors the required separation margin to the first critical speed is within 0% to 17%, and within 10% to 27% to the second critical speed, which stresses a safer operational margin to higher critical speed. The higher response for critical speed above the operational speed is related to higher unbalance forces for the same unbalance magnitude.

Required separation margin equations provide a safety factor from critical to operational speeds. API 617 [4] first edition required the first critical at least 10% below any operational speed, and for the second critical 20% over the maximum continuous speed for flexible shafts. The fourth edition changed the separation margin for the first critical to 15% and the Amplification Factor, AF became a concern and could not exceed 8. The last edition combines the critical speed AF and the separation margin in one equation.

2. The maximum calculated unbalanced response over operational speed range A_{max} at each vibration probe, for each unbalance amount and case as specified in API 617 [4] shall not exceed the vibration limit A_{v_1} or 12.7μm, whichever

is less, over the operational speed range (N_{ma} to N_{mc}) as shown in fig. 2.3. Notice that the peak within operational speed is only illustrative and the maximum vibration amplitude in the speed range does not represent a critical speed.

The vibration limit A_{v_1} (μm) is related to maximum continuous speed N_{mc} (rpm) and is given by

$$A_{v_1} = 12.7\sqrt{\frac{12000}{N_{mc}}} \tag{2.7}$$

A_{v_1} is an empirical value based on users and developers experience. API 617 [4] first edition launched a vibration limit within the operational speed for rotors whose Maximum Continuous Speed N_{mc} was over 6000 rpm as 19.05μm. The third edition established eq. (2.7) as a requirement except from the vibration limit that could not exceed $25.4\mu m$. Therefore, the vibration limit A_{v_1} has been used as a standard since 1973 and has been proved reasonable over the last few decades.

3. For each unbalance amount and case as specified by API 617 [4] standard the calculated major-axis zero-to-peak response amplitudes shall be checked the minimum clearance between stationary and rotating machine parts. Figure 2.3 indicates through the resonance peak $2 \times Ur$ the probable minimum clearance rotor speed. The close clearance response shall be multiplied by a scale factor S_{cc} which is defined by

$$S_{cc} = \frac{A_{v_1}}{A_{max}} \tag{2.8}$$

where A_max is the maximum probe response within operational speed range.

The scaled response shall be less than 75% minimum running clearance over the range from zero to $150\%N_{mc}$. Usually running clearance is different from assembled clearance due to centrifugal/thermal growth, non-concentricity of the stator to the bearings, rotor sag, etc.

Notice that multiplication to the scale factor S_{cc} considers the response to be linear and therefore, evaluates the maximum amplitude if the vibration limit A_{v1} were achieved. The 25% margin below minimum running clearance is a safety factor that has been used since API 617 [4] fifth edition.

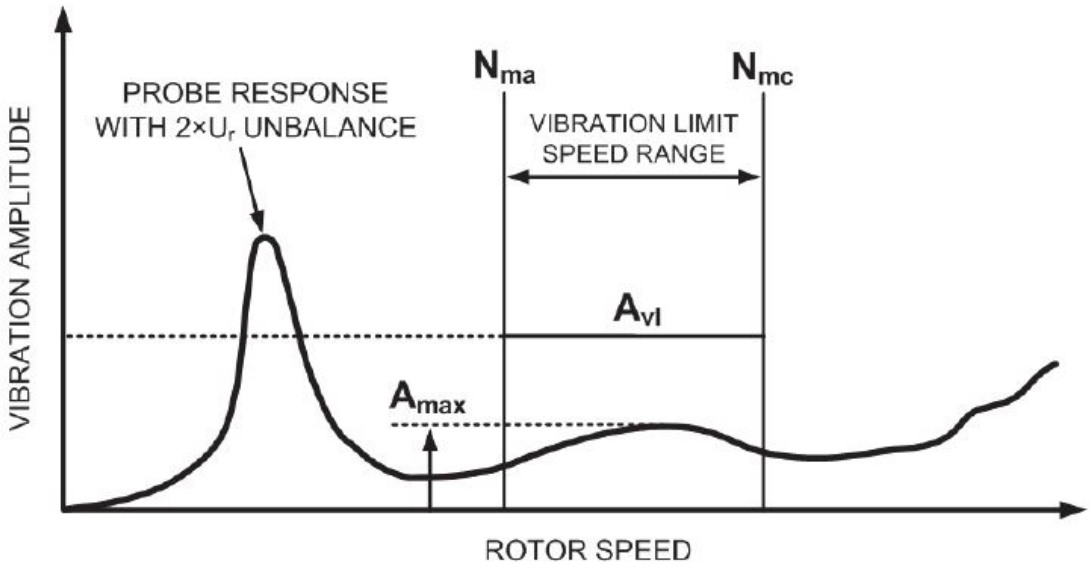

Figure 2.3: Plot of Applicable Speed Range of Vibration Limit API 617 [4].

Chapter 3

Model Development

3.1 Elements

In order to analyze the lateral vibration of a rotor, it requires the equation of motion and the elements matrices. The finite element method is an approach to derive the equation. Through the definition of the finite element mesh and the degrees of freedom on each node, the elements may be expressed by energy equations, and hence, the application of Lagrange's equations derives the elements matrices.

3.1.1 Disk

The disk is modeled based on kinetic energy due to translational and rotational motion. The total energy to a rigid and symmetric disk with small angular displacements is only kinetic and may be defined by (LALANNE and FERRARIS [12])

$$T_d = \frac{1}{2}m_d(\dot{u}^2 + \dot{v}^2) + \frac{1}{2}I_d(\dot{\theta}^2 + \dot{\psi}^2) + \frac{1}{2}I_p(\Omega^2 - 2\Omega\dot{\psi}\theta) \tag{3.1}$$

where I_p is the polar moment of inertia about the shaft; I_d is the diametral moment of inertia about an axis perpendicular to the shaft line; m_d the disk mass; and angles with respective angular velocities as shown by fig. 3.1.

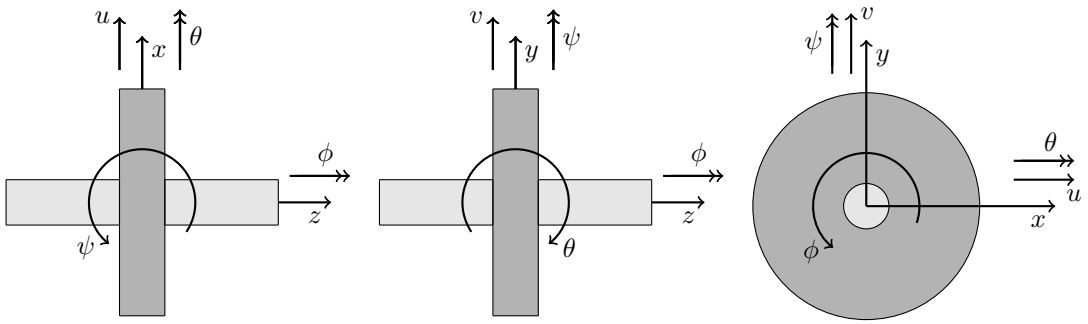

(a) xz plane (b) yz plane (c) xy plane

Figure 3.1: Coordinates of a rotor-disk-bearing system

Applying Lagrange's equations the inertia terms arises. Hence, the mass matrix for the disk is

$$\mathbf{M}_e = \begin{bmatrix} m_d & 0 & 0 & 0 \\ 0 & m_d & 0 & 0 \\ 0 & 0 & I_d & 0 \\ 0 & 0 & 0 & I_d \end{bmatrix} \tag{3.2}$$

and the gyroscopic matrix,

$$\mathbf{G}_e = \begin{bmatrix} 0 & 0 & 0 & 0 \\ 0 & 0 & 0 & 0 \\ 0 & 0 & 0 & I_p \\ 0 & 0 & -I_p & 0 \end{bmatrix} \tag{3.3}$$

where the displacement vector is $[u\ v\ \theta\ \psi]^T$ as the degrees of freedom shown in fig. 3.1.

A more detailed explanation is on appendix A.

3.1.2 Shaft

The shaft elements are modeled based on Timoshenko beam, i.e., shear effect and rotary inertia are included. Figure 3.2 shows the angle β_e which represents the difference between the plane of the beam cross-section and the normal to the beam centerline after deformation. The angle which the beam cross-section rotates due to deformation, ψ_e, the shear angle β_e and the slope of the centerline $\partial u_e/\partial \xi$ are related by the equation:

$$\psi_e(\xi, t) = \frac{\partial u_e(\xi, t)}{\partial \xi} + \beta_e(\xi, t) \tag{3.4}$$

where u_e is the lateral displacement.

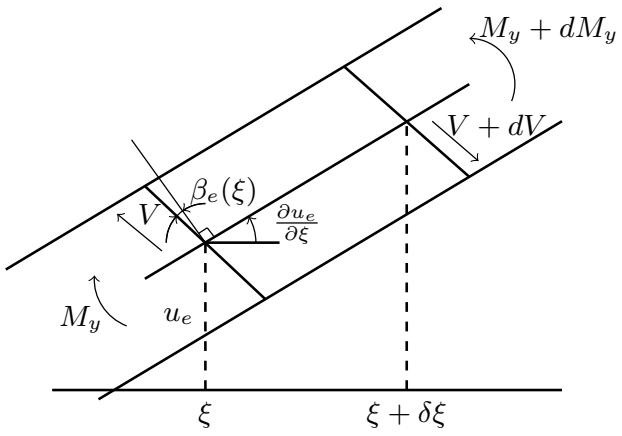

Figure 3.2: Small section of a Timoshenko beam at plane XZ.

Figure 3.3 shows local coordinates, $u_{e1}(t)$, $\psi_{e1}(t)$, $u_{e2}(t)$, $\psi_{e2}(t)$.

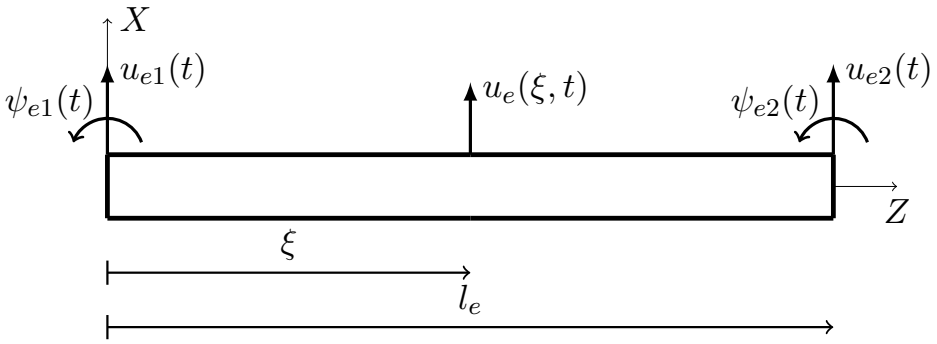

Figure 3.3: Local coordinates for beam element at plane XZ.

The momentum equilibrium for the Timoshenko's beam shown in fig. 3.2 yields

$$\frac{\partial}{\partial \xi}\left(E_e I_e(\xi)\frac{\partial \psi_e(\xi,t)}{\partial \xi}\right) = \kappa_e G_e A_e \beta_e(\xi,t) \tag{3.5}$$

where I_e is the cross-sectional area moment of inertia about the Y axis, A_e the cross section area, κ_e the shear constant that depends on the shape of the cross section of the beam and G_e is the shear modulus, with $G_e = E_e/2(1+\nu_e)$, where ν_e is Poisson's ratio. The shear constant compensates the model assumption that a plane section remains plane after displacement. For circular solid shaft shear constant may be given by eq. (3.6) (FRISWELL [13]).

$$\kappa_e = \frac{6(1+\nu_e)}{(7+6\nu_e)} \tag{3.6}$$

Notice that eq. (3.5) neglects inertia term.

The methodology to find the element matrices in the equation of motion will consider energy assumptions. The matrices are the stiffness,

mass and gyroscopic for the Timoshenko beam element. The displacement vector will consider YZ plane (fig. 3.4) as well and therefore, $\mathbf{q}_e = [u_{e1}(t)\ v_{e1}(t)\ \theta_{e1}(t)\ \psi_{e1}(t)\ u_{e2}(t)\ v_{e2}(t)\ \theta_{e2}(t)\ \psi_{e2}(t)]^T$.

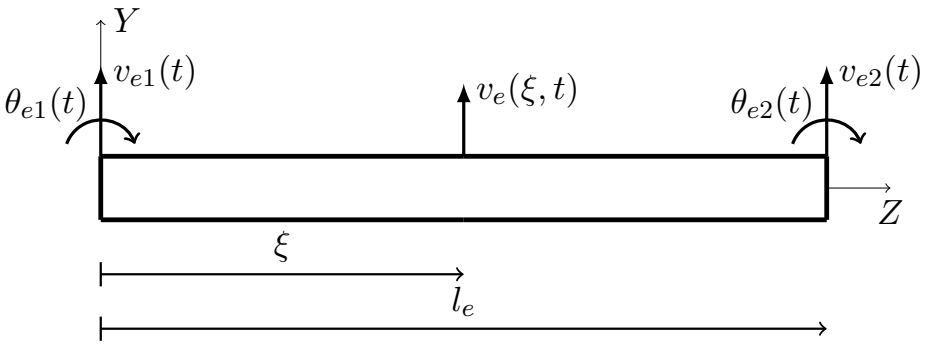

Figure 3.4: Local coordinates for beam element at plane YZ.

- Firstly, the strain energy which considers both stress and shear terms may be defined by

$$\begin{aligned} U_e =& \frac{1}{2}E_eI_e\int_0^{l_e}\left(\frac{\partial u_e(\xi,t)}{\partial\xi}\right)^2 d\xi + \frac{1}{2}\kappa_e^2 G_eA_e\int_0^{l_e}\beta_e^2(\xi,t)\,d\xi \\ &+\frac{1}{2}E_eI_e\int_0^{l_e}\left(\frac{\partial v_e(\xi,t)}{\partial\xi}\right)^2 d\xi + \frac{1}{2}\kappa_e^2 G_eA_e\int_0^{l_e}\beta_e'^2(\xi,t)\,d\xi \end{aligned} \tag{3.7}$$

  where the shaft is assumed to be symmetric in XZ and YZ planes and β_e' is the shear angle in YZ plane.

  Substitution of Timoshenko beam equations into eq. (3.7) and the application of Lagrange's equations "$\frac{d}{dt}(\frac{\partial}{\partial\dot{q}_{e_i}}) - \frac{\partial}{\partial q_{e_i}}$ "yields the stiffness matrix

$$\mathbf{K}_e = \frac{E_eI_e}{(1+\Phi_e)l_e^3}\begin{bmatrix} 12 & 0 & 0 & 6l_E & -12 & 0 & 0 & 6l_e \\ 0 & 12 & -6l_e & 0 & 0 & -12 & -6l_e & 0 \\ 0 & -6l_e & l_e^2(4+\Phi_e) & 0 & 0 & 6l_e & l_e^2(2-\Phi_e) & 0 \\ 6l_e & 0 & 0 & l_e^2(4+\Phi_e) & -6l_e & 0 & 0 & l_e^2(2-\Phi_e) \\ -12 & 0 & 0 & -6l_e & 12 & 0 & 0 & -6l_e \\ 0 & -12 & 6l_e & 0 & 0 & 12 & 6l_e & 0 \\ 0 & -6l_e & l_e^2(2-\Phi_e) & 0 & 0 & 6l_e & l_e^2(4+\Phi_e) & 0 \\ 6l_e & 0 & 0 & l_e^2(2-\Phi_e) & -6l_e & 0 & 0 & l_e^2(4+\Phi_e) \end{bmatrix} \tag{3.8}$$

- Kinetic energy for a Timoshenko beam element is similar to a disk as in

eq. (3.1). It applies translational, rotary inertia, constant term and gyroscopic effects as shown in eq. (3.9)

$$T_{Se} = \frac{\rho_e A_e}{2} \int_0^{l_e} (\dot{u}_e^2 + \dot{v}_e^2) d\xi + \frac{\rho_e I_e}{2} \int_0^{l_e} (\dot{\psi}_e^2 + \dot{\theta}_e^2) d\xi + \rho_e I_e l_e \Omega^2 - 2\rho_e I_e \Omega \int_0^{l_e} \dot{\psi}_e \theta_e d\xi \tag{3.9}$$

where ρ_e is shaft density.

Handling eq. (3.9), neglecting gyroscopic effects and the application of Lagrange's equations produces the mass matrix

$$\mathbf{M}_e = \frac{\rho_e A_e l_e}{840(1+\Phi_e)^2} \begin{bmatrix} m_1 & 0 & 0 & m_2 & m_3 & 0 & 0 & m_4 \\ 0 & m_1 & -m_2 & 0 & 0 & m_3 & -m_4 & 0 \\ 0 & -m_2 & m_5 & 0 & 0 & +m_4 & m_6 & 0 \\ m_2 & 0 & 0 & m_5 & -m_4 & 0 & 0 & m_6 \\ m_3 & 0 & 0 & -m_4 & m_1 & 0 & 0 & -m_2 \\ 0 & m_3 & m_4 & 0 & 0 & m_1 & m_2 & 0 \\ 0 & -m_4 & m_6 & 0 & 0 & m_2 & m_5 & 0 \\ m_4 & 0 & 0 & m_6 & -m_2 & 0 & 0 & m_5 \end{bmatrix}$$

$$+ \frac{\rho_e I_e}{30(1+\Phi_e)^2 l_e} \begin{bmatrix} m_7 & 0 & 0 & m_8 & -m_7 & 0 & 0 & m_8 \\ 0 & m_7 & -m_8 & 0 & 0 & -m_7 & -m_8 & 0 \\ 0 & -m_8 & m_9 & 0 & 0 & m_8 & m_{10} & 0 \\ m_8 & 0 & 0 & m_9 & -m_8 & 0 & 0 & m_{10} \\ -m_7 & 0 & 0 & -m_8 & m_7 & 0 & 0 & -m_8 \\ 0 & -m_7 & m_8 & 0 & 0 & m_7 & m_8 & 0 \\ 0 & -m_8 & m_{10} & 0 & 0 & m_8 & m_9 & 0 \\ m_8 & 0 & 0 & m_{10} & -m_8 & 0 & 0 & m_9 \end{bmatrix} \tag{3.10}$$

where

$$m_1 = 312 + 588\Phi_e + 280\Phi_e^2 \tag{3.11}$$
$$m_2 = (44 + 77\Phi_e + 35\Phi_e^2)l_e \tag{3.12}$$
$$m_3 = 108 + 252\Phi_e + 140\Phi_e^2 \tag{3.13}$$
$$m_4 = -(26 + 63\Phi_e + 35\Phi_e^2)l_e \tag{3.14}$$
$$m_5 = (8 + 14\Phi_e + 7\Phi_e^2)l_e^2 \tag{3.15}$$
$$m_6 = -(6 + 14\Phi_e + 7\Phi_e^2)l_e^2 \tag{3.16}$$
$$m_7 = 36 \tag{3.17}$$
$$m_8 = (3 - 15\Phi_e)l_e \tag{3.18}$$
$$m_9 = (4 + 5\Phi_e + 10\Phi_e^2)l_e^2 \tag{3.19}$$
$$m_{10} = (-1 - 5\Phi_e + 5\Phi_e^2)l_e^2 \tag{3.20}$$

- The last term in eq. (3.9) represents gyroscopic effects. The kinetic energy contribution due gyroscopic effects is stressed in eq. (3.21).

$$T_{Ge} = -2\rho_e I_e \Omega \int_0^{l_e} \dot{\psi}_e(\xi, t)\theta_e(\xi, t)\, d\xi \tag{3.21}$$

  Development of this energy equation and the application of Lagrange's equations follows the gyroscopic matrix:

$$\mathbf{G}_e = \frac{\rho_e I_e}{15(1+\Phi_e)^2 l_e} \begin{bmatrix} 0 & g_1 & -g_2 & 0 & 0 & -g_1 & -g_2 & 0 \\ -g_1 & 0 & 0 & -g_2 & g_1 & 0 & 0 & -g_2 \\ g_2 & 0 & 0 & g_3 & -g_2 & 0 & 0 & g_4 \\ 0 & g_2 & -g_3 & 0 & 0 & -g_2 & -g_4 & 0 \\ & -g_1 & g_2 & 0 & 0 & g_1 & g_2 & 0 \\ g_1 & 0 & 0 & g_2 & -g_1 & 0 & 0 & g_2 \\ g_2 & 0 & 0 & g_4 & -g_2 & 0 & 0 & g_3 \\ 0 & g_2 & -g_4 & 0 & 0 & -g_2 & -g_3 & 0 \end{bmatrix} \tag{3.22}$$

where

$$g_1 = 36 \tag{3.23}$$

$$g_2 = (3 - 15\Phi_e)l_e \tag{3.24}$$

$$g_3 = (4 + 5\phi_e + 10\phi_e^2)l_e^2 \tag{3.25}$$

$$g_4 = (-1 - 5\phi_e + 5\phi_e^2)l_e^2 \tag{3.26}$$

$$\tag{3.27}$$

For a detailed explanation regarding the element matrices calculations see appendix A.

3.1.3 Bearing

The forces working on the shaft due to bearing damping and stiffness effects may be written as

$$\begin{bmatrix} F_u \\ F_v \end{bmatrix} = - \begin{bmatrix} k_{uu} & k_{uv} \\ k_{vu} & k_{vv} \end{bmatrix} \begin{bmatrix} u \\ v \end{bmatrix} - \begin{bmatrix} c_{uu} & c_{uv} \\ c_{vu} & c_{vv} \end{bmatrix} \begin{bmatrix} \dot{u} \\ \dot{v} \end{bmatrix} \tag{3.28}$$

Hence for the local coordinate vector $[u, v]^T$,

$$\mathbf{K}_e = \begin{bmatrix} k_{uu} & k_{uv} \\ k_{vu} & k_{vv} \end{bmatrix} \tag{3.29}$$

$$\mathbf{C}_e = \begin{bmatrix} c_{uu} & c_{uv} \\ c_{vu} & c_{vv} \end{bmatrix} \tag{3.30}$$

where $\mathbf{K}_e$ and $\mathbf{C}_e$ relates to stiffness and damping element matrix, respectively. The dynamic coefficients are obtained from a Taylor series expansion on the fluid forces from the pressure profile, which in turn comes from the Reynolds equation solution.

Since a tilting pad is a fluid film bearing the software XRLTC^2 (from Texas A&M Turbomachinery Laboratorium) which performs a computational fluid dynamic and MAXBRG (from University of Virginia) which conducts a thermo-elasto-hydrodynamic (TEHD) analysis may estimate the bearing coefficients.

Reynolds Equation

In order to estimate the bearing coefficients, the software listed are based on computer fluid dynamic analysis. Within this section, a brief explanation is summarized regarding tilting pad lubrication theory evolving hydrodynamic, energy and deformation effects (DIMOND [2]).

The local coordinates for a single pad bearing are shown in fig. 3.5 which represents a free body diagram with stiffness and damping effects.

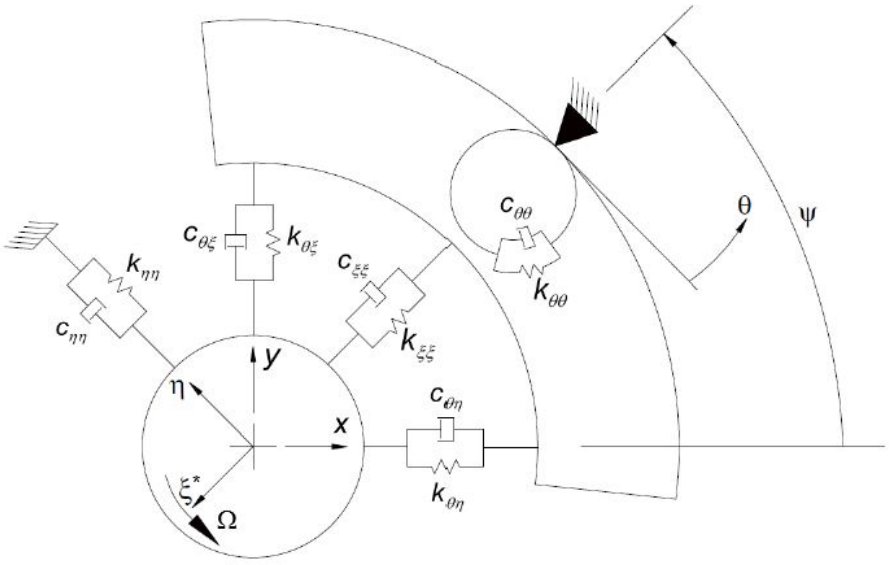

Figure 3.5: Pad rotational and shaft translational degrees of freedom.

Reynolds equation combines Navier-Stokes and the continuity equation. For bearing analysis the model is enhanced with turbulence effects through an eddy-viscosity model and some terms are neglected due to geometry. Equation (3.31) is the generalized Reynolds equation which assumes that the pressure profile is constant across the lubricating film, i.e. neglecting $\partial p/\partial \xi^*$ as well.

$$\frac{\partial}{\partial \eta}\left\{h^3\Gamma(\eta, z, Re^*)\frac{\partial p}{\partial \eta}\right\} + \frac{\partial}{\partial \eta}\left\{h^3\Gamma(\eta, z, Re^*)\frac{\partial p}{\partial z}\right\} = -UG(\eta, z, Re^*)\frac{\partial h}{\partial \eta} \qquad (3.31)$$

where h denotes lubricating film thickness, η shaft displacement perpendicular to pivot (pad local coordinate system), z axial direction, p developed pressure, U fluid velocity due to rotating motion of bearing surface, Re^* Reduced Reynold number which considers turbulent effects, G effective cross-film viscosity and Γ, effective cross-film viscosity. G and Γ are given by

$$G(\eta, z, Re^*) = \frac{1}{\chi_1(\eta, 1, z, Re^*)} \int_0^1 \chi_1(\eta, 1, z, Re^*) d\xi^* \tag{3.32}$$

$$\Gamma(\eta, z, Re^*) = \int_0^1 \left[\chi_2(\eta, \xi^*, z, Re^*) - \frac{\chi_2(\eta, 1, z, Re^*)}{\chi_1(\eta, 1, z, Re^*)} \chi_1(\eta, 1, z, Re^*) \right] d\xi^* \tag{3.33}$$

$$\chi_1(\eta, \xi^*, z) = \int_0^{\xi^*} \frac{1}{\mu_e(\eta, \xi', z, Re^*)} d\xi^{*'} \tag{3.34}$$

$$\chi_2(\eta, \xi^*, z, Re^*) = \int_0^{\xi^*} \frac{\xi^{*'}}{\mu_e(\eta, \xi^{*'}, z, Re^*)} d\xi^{*'} \tag{3.35}$$

where ξ^* is the shaft displacement parallel to pivot (pad local coordinate system), $\xi^{*'}$ dimensionless shaft displacement parallel to pivot (pad local coordinate) and μ_e, the effective lubricant dynamic viscosity corrected for turbulence.

The flow profile in the bearing is expressed by

$$\begin{aligned} u^*(\eta, \xi^*, z) =& \frac{\partial p}{\partial \eta} \chi_2(\eta, \xi^*, z, Re^*) \\ &+ \left\{ \frac{U}{\chi_1(\eta, h, z, Re^*)} - \frac{\partial p}{\partial \eta} \left[\frac{\chi_2(\eta, h, z, Re^*)}{\chi_1(\eta, h, z, Re^*)} \right] \right\} \chi_1(\eta, h, z, Re^*) \end{aligned} \tag{3.36}$$

$$w^*(\eta, \xi^*, z, Re^*) = \frac{\partial p}{\partial z} \chi_2(\eta, \xi^*, z, Re^*) - \frac{\partial p}{\partial z} \left[\frac{\chi_2(\eta, h, z, Re^*)}{\chi_1(\eta, h, z, Re^*)} \right] \chi_1(\eta, h, z, Re^*) \tag{3.37}$$

where $u*$ and $w*$ are local fluid velocity along rotation and axial direction, respectively. Hence, the solution of equations results in the pressure field in the lubricating film and the net forces in the bearing.

Turbulence Modelling

The turbulence is modeled using eddy viscosity law which represents the effective viscosity and the eddy viscosity ϵ_m by ([14])

$$\mu_e(\eta, \xi^*, z) = \mu \left(1 + \frac{\epsilon_m}{\nu_l} \right) \tag{3.38}$$

$$\frac{\epsilon_m}{\nu_l} = \kappa \left[\xi^+ - \delta_l^+ \tanh \left(\frac{\xi^+}{\delta_l^+} \right) \right] \tag{3.39}$$

where ν_l is the lubricant kinematic viscosity, μ is the fluid dynamic viscosity, $\kappa = 0.4$, $\delta_l^+ = 10.7$ and ξ^+ the non-dimensional distance from the wall, whose expression is given by

$$\xi^+ = \frac{\xi^*}{\nu_l} \sqrt{\frac{|\tau|}{\rho_l}} \tag{3.40}$$

$$\tau = \mu_e \sqrt{\left(\frac{\partial u^*}{\partial \xi^*}\right)^2 + \left(\frac{\partial w^*}{\partial \xi^*}\right)^2} \tag{3.41}$$

For flow regime transition a scaling factor δ is added to modify the eddy viscosity and is expressed by

$$\delta = \begin{cases} 0.0, & (Re_h)_{max} \leq Re_L; \\ 1.0 - \left[\frac{Re_H - (Re_h)_{max}}{Re_H - Re_L}\right]^{1/8}, & Re_L \leq (Re_h)_{max} \leq Re_H; \\ 1.0, & Re_H \leq (Re_h)_{max}. \end{cases} \tag{3.42}$$

where Re_h is the local Reynolds number, Re_L the Reynolds number which represents the transition from laminar flow and Re_H the transition to turbulent flow. The assumption of the values for both critical numbers of Reynolds are 500 and 1000 which are adopted by articles and dissertations reviewed on this section.

Analogue to viscosity the effective heat conductivity is corrected due to turbulence effects which yields

$$k_e = \nu_l \left(\frac{1}{Pr} + \frac{1}{Pr^{(t)}} \frac{\epsilon_m}{\nu_l}\right) \tag{3.43}$$

where Pr is Prandt number and $Pr^{(t)}$ is normally used as 0.769 (HE and ALLAIRE [14]).

Energy Equation

The developed pressure in bearings is actually coupled to temperature due to the lubricant dynamic viscosity μ and viscous shear. The generalized energy equation is then presented in eq. (3.44) whose first order terms represent heat convection, the second order terms represent heat conductions and the last term, heat generation due to viscous shear (HE and ALLAIRE [14]).

$$\rho_l C_p \left(u^* \frac{\partial T}{\partial \eta} + v^* \frac{\partial T}{\partial \xi^*}\right) = \frac{\partial}{\partial \eta}\left(k \frac{\partial T}{\partial \eta}\right) + \frac{\partial}{\partial \xi^*}\left(k_e \frac{\partial T}{\partial \eta}\right) + \mu_e \left[\left(\frac{\partial u^*}{\partial \xi^*}\right)^2 + \left(\frac{\partial w^*}{\partial \xi^*}\right)^2\right] \tag{3.44}$$

where ρ_l is the lubricant density, C_p lubricant specific heat, T lubricant temperature, v^* local fluid velocity in film thickness direction, k lubricant heat conductivity, k_e lubricant effective heat conductivity (corrected for turbulence), μ_e effective lubricant dynamic viscosity (corrected for turbulence).

Deformation Equation

The Thermo-Elasto-Hydrodynamic (TEHD) analysis may include the pad deformation. The eq. (3.45) first term is the internal strain energy, the second term is the thermal strain energy and the last term represents the pressure work (HE [15])

$$\int_V \delta\{u\}^T[D]^T[E][D]\{u\}dV - \int_V \delta\{u\}^T[D]^T[E][D]\{\varepsilon_0\}dV - \int_S \delta\{u\}^T PdA = 0 \tag{3.45}$$

where $\{u\}$ is the displacement vector, $\delta\{u\}$ the virtual displacement vector, $[D]$ derivative matrix, $[E]$ property matrix for plane strain, ε_0 and P the pressure.

In addition to pad deformation, the pivot deformation may be considered for heavy mechanical loads based on Hertzian contact stress analysis (DIMOND [2]).

The solution of these equations is carried out by finite element analysis and the search algorithm for the bearing coefficients is based on the perturbed Reynolds equation which is reduced to two translational degrees of freedom.

Thermo-Elasto-Hydrodynamic Algorithm

Figure 3.6 shows a flowchart which details the steps on a TEHD algorithm. The iterative process begins with initial values for viscosity and heat conductivity. The hydrodynamic section is the next step which is carried out by a finite element analysis. The bearing is regular flooded, and the boundary conditions are the pressure supply, the ambient pressure in the axial edges, $\frac{\partial p}{\partial \eta}$ which equals zero in the cavitation zone and the cavitation pressure. The Reynolds and the Turbulence equations iteratively determine the pressure field. Then, the pad tilt angle is evaluated for a static moment equilibrium about every single pivot. The journal position is searched by Newton-Raphson method which considers the force equilibrium equations.

The next section is the Thermo analysis which is carried out considering the generalized energy equation by the finite element method. The film and the pad are solved in one mesh grid. This analysis will assume that fluid velocities, heat conductivity, and heat generation are axially averaged; temperature of the groove between pads is a mixing model and a normal flooded condition without axial flow. The boundary conditions derive from the normal flooded condition. The pressure field from the Reynolds equation is used to evaluate the viscous shear term of the energy equation.

The journal temperature is considered an average of the film temperature. Once the temperature is evaluated, the viscosity and heat conductivity are set up to the hydrodynamic analysis until the pressure field, and the temperature converge. The deformation shown in the Figure 3.6 is the last in the TEHD iteration due to the

impact on the film thickness. This analysis assumes the pad to be a rectangle, and no journal and shell deformations are considered. Lastly, once the pressure field and the temperature converge it is carried out the perturbed Reynolds equation to every degree of freedom which results in the stiffness coefficients. The damping coefficient comes from the perturbed Reynolds equation to every velocity from the degrees of freedom. The last step is the reduction to horizontal and vertical degrees of freedom which may be to synchronous or non-synchronous speed. For unbalance response the synchronous coefficients are chosen.

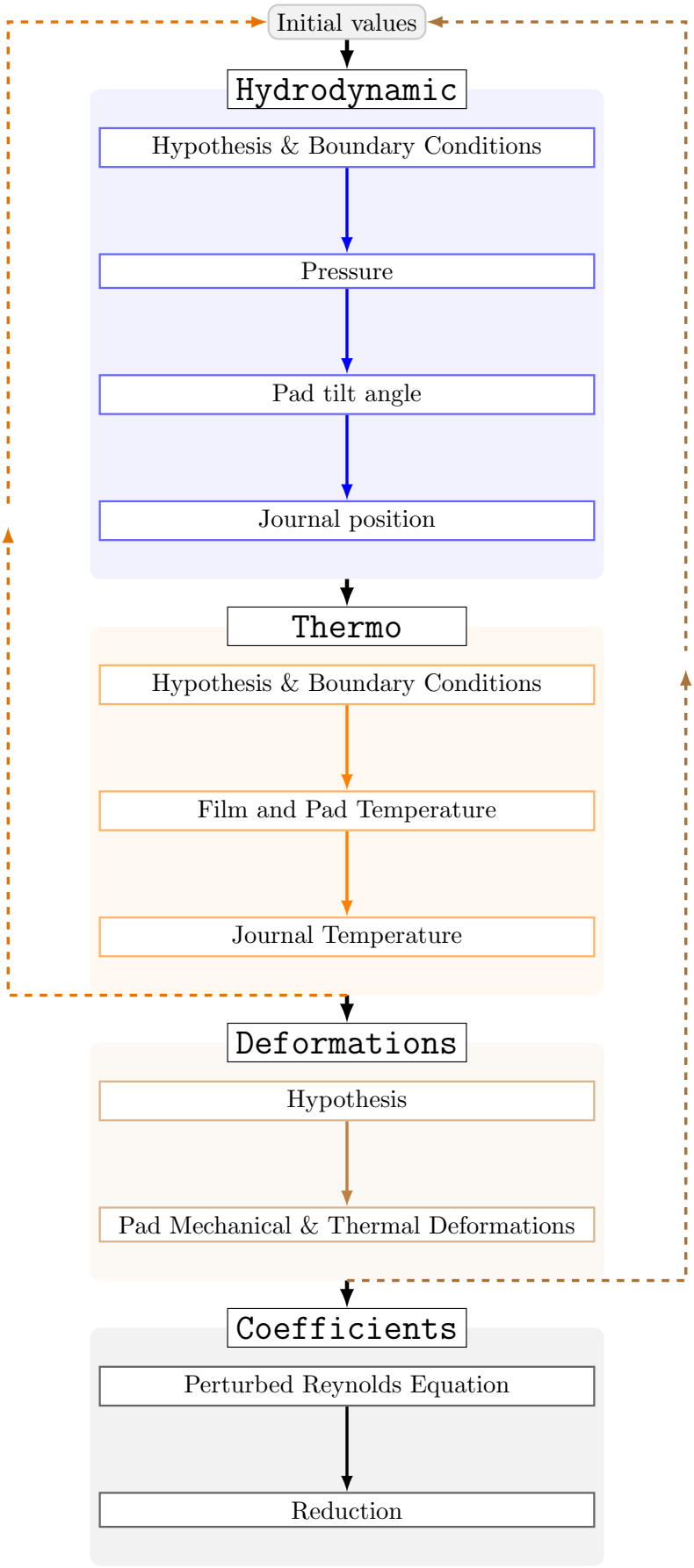

Figure 3.6: Thermo-Elasto-Hydrodynamic (TEHD) algotithm flowchart.

3.2 Deterministic equations

3.2.1 Damped free vibration

The partial differential equation which represents the full equation of motion of the linearized assembled system for a damped free vibration is defined by eq. (3.46) (FRISWELL [13]).

$$\mathbf{M}\ddot{\mathbf{q}}(t) + \mathbf{C}(\Omega)\dot{\mathbf{q}}(t) + \Omega\mathbf{G}\dot{\mathbf{q}}(t) + \mathbf{K}(\Omega)\mathbf{q}(t) = \mathbf{0} \tag{3.46}$$

where $\mathbf{M}$ is the mass matrix, $\mathbf{C}(\Omega)$ damping matrix, $\mathbf{G}$ the gyroscopic matrix, $\mathbf{K}(\Omega)$ stiffness matrix and $\mathbf{q}(t)$ the displacement vector of bearing's centerline.

3.2.2 State-space problem

Handling eq. (3.46) is possible to rewrite the damped free vibration into a state-space form as per eq. (3.47).

$$\dot{\mathbf{Y}}(t) = \begin{bmatrix} \mathbf{0} & \mathbf{I} \\ -\mathbf{M}^{-1}\mathbf{K}(\Omega) & -\mathbf{M}^{-1}\big(\Omega\mathbf{G} + \mathbf{C}(\Omega)\big) \end{bmatrix} \mathbf{Y}(t) \tag{3.47}$$

where

$$\mathbf{Y}(t) = \begin{Bmatrix} \mathbf{q}(t) \\ \dot{\mathbf{q}}(t) \end{Bmatrix} \tag{3.48}$$

The eigenvalue problem for this state-space form yields

$$\lambda\mathbf{Z} = \begin{bmatrix} \mathbf{0} & \mathbf{I} \\ -\mathbf{M}^{-1}\mathbf{K}(\Omega) & -\mathbf{M}^{-1}\big(\Omega\mathbf{G} + \mathbf{C}(\Omega)\big) \end{bmatrix} \mathbf{Z} \tag{3.49}$$

where

$$y(t) = ze^{\lambda t} \tag{3.50}$$

The eigenvalue is defined by eq. (3.51)(INMAN [16]).

$$\lambda_i = -|\xi_i|\omega_{ni} - \omega_{ni}\left(\sqrt{1-\xi_i^2}\right)j \tag{3.51}$$

where λ is the eigenvalue, ω_n natural frequency, ξ damping ratio and z, eigenvector.

3.2.3 Unbalance response

Out-of-balance forces and moments arise from differences between the geometric centerline and mass centerline. Figure 3.7 shows an unbalance mass m_u and the mass eccentricity ε at plane XY plane.

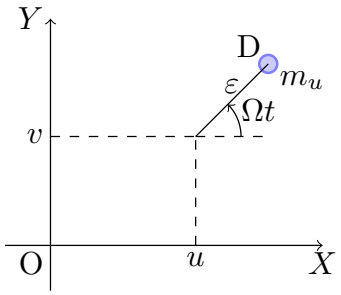

Figure 3.7: Mass unbalance at XY plane.

Then, the displacement of the unbalance mass is

$$\bar{OD} = \begin{Bmatrix} u + \varepsilon \cos \Omega t \\ v + \varepsilon \sin \Omega t \\ 0 \\ 0 \end{Bmatrix} \tag{3.52}$$

From eq. (3.52) the kinetic energy is given by

$$T_u = \frac{m_u}{2}\Big[\dot{u}^2 + \dot{v}^2 + \varepsilon\Omega^2 - 2\dot{u}\Omega\varepsilon \sin \Omega t + 2\dot{v}\Omega\varepsilon \cos \Omega t\Big] \tag{3.53}$$

Application of Lagrange's equations to the kinetic energy produces the centrifugal force, and therefore, the equation of motion is recast as

$$\mathbf{M}\ddot{\mathbf{q}}(t) + \mathbf{C}(\Omega)\dot{\mathbf{q}}(t) + \Omega\mathbf{G}\dot{\mathbf{q}}(t) + \mathbf{K}(\Omega)\mathbf{q}(t) = \mathbf{F}_0 \tag{3.54}$$

where

$$\mathbf{F}_0 = \begin{Bmatrix} \Omega^2 m_u \varepsilon \cos(\Omega t + \delta) \\ \Omega^2 m_u \varepsilon \sin(\Omega t + \delta) \\ 0 \\ 0 \end{Bmatrix} \tag{3.55}$$

and $\mathbf{F}_0$ represents unbalance force for a local coordinate vector $[u\ v\ \theta\ \psi]^T$ and a constant speed Ω. Notice that δ is the unbalance phase.

Handling eq. (3.54) by the use of Fourier transform which states $q(t) = \hat{\mathbf{q}}(\Omega)e^{j\Omega t}$ and $\mathbf{f_0}(\mathbf{t}) = \hat{\mathbf{f}}_\mathbf{0}(\Omega)e^{j\Omega t}$ yields

$$\hat{\mathbf{q}}(\Omega) = \big[\big(\mathbf{K}(\Omega) - \Omega^2\mathbf{M}\big) + j\Omega\big(\Omega\mathbf{G} + \mathbf{C}(\Omega)\big)\big]^{-1}\hat{\mathbf{f}}_0(\Omega) \tag{3.56}$$

where $\hat{\mathbf{q}}(\Omega)$ and $\hat{\mathbf{f}}_0(\Omega)$ are the response and the unbalance force on frequency domain, respectively.

3.3 Stochastic model

3.3.1 Maximum entropy principle

The maximum entropy principle provides a criterion to construct stiffness and damping stochastic models. SHANNON [17] defines entropy equation as

$$S = \int_{-\infty}^{+\infty} f_x(x) \ln[f_x(x)]\, dx \tag{3.57}$$

Thus, the maximum entropy yields

$$f_x(x) = \text{argmax } S\big(f_x(x)\big) \tag{3.58}$$

All prior information should be used. For stiffness and damping, the intervals of the probability density functions, PDF's, are based on errors of experimental data review on chapter 2.

WYGANT *et al.* [9] found uncertainty levels which ranges to 45% for the translational stiffness and 82% for the translational damping as also reviewed on API 684 [3]. Therefore, the stiffness can be considered within $\big[k(\Omega), \big(k(\Omega) + 45\%k(\Omega)\big)\big]$ and damping, $\big[c(\Omega), \big(c(\Omega) + 82\%c(\Omega)\big)\big]$. Application of the maximum entropy principle yields uniform distributions which are given by eq. (3.59) and eq. (3.60).

$$f_k = \mathbb{I}_{[k(\Omega),1.45k(\Omega)]} \frac{1}{0.45k(\Omega)} \tag{3.59}$$

$$f_c = \mathbb{I}_{[c(\Omega),1.82c(\Omega)]} \frac{1}{0.82c(\Omega)} \tag{3.60}$$

where

$$\mathbb{I}_{[a,b]}(x) = \begin{cases} 1, & \text{if } a < x < b \\ 0, & \text{otherwise} \end{cases} \tag{3.61}$$

Notice that a and b represent the range of uniform distributions, i.e, $\mathbf{K}(\Omega)$ and $1.45\mathbf{K}(\Omega)$ for stiffness, and $\mathbf{C}(\Omega)$ and $1.82\mathbf{C}(\Omega)$ for damping, respectively.

The uniform distributions will be applied on the bearings matrices as follows:

$$\mathcal{K}_b(\Omega) = \mathcal{U}_1 \begin{bmatrix} k_{uu}(\Omega) & k_{uv}(\Omega) \\ k_{vu}(\Omega) & k_{vv}(\Omega) \end{bmatrix} + \mathcal{U}_1 \begin{bmatrix} k_{uu}(\Omega) & k_{uv}(\Omega) \\ k_{vu}(\Omega) & k_{vv}(\Omega) \end{bmatrix} \tag{3.62}$$

$$\mathcal{C}_b(\Omega) = \mathcal{U}_2 \begin{bmatrix} c_{uu}(\Omega) & c_{uv}(\Omega) \\ c_{vu}(\Omega) & c_{vv}(\Omega) \end{bmatrix} + \mathcal{U}_2 \begin{bmatrix} c_{uu}(\Omega) & c_{uv}(\Omega) \\ c_{vu}(\Omega) & c_{vv}(\Omega) \end{bmatrix} \tag{3.63}$$

where $\mathcal{K}_b(\Omega)$ is the random stiffness matrix from the bearings, $\mathcal{C}_b(\Omega)$ is the damping

random matrix from the bearings, $\mathcal{U}_1$ random stiffness uniform distribution for the drive-end side and non-drive end side bearing, and $\mathcal{U}_2$ the random damping uniform distribution for the drive-end side and non-drive end side bearing.

3.3.2 Damped free vibration

The stiffness and damping as uncertain parameters imply a stochastic model for the equation of motion. Therefore, Equation (3.46) may be rewritten as

$$\mathbf{M}\ddot{\mathcal{Q}}(t) + \mathcal{C}(\Omega)\dot{\mathcal{Q}}(t) + \Omega\mathbf{G}\dot{\mathcal{Q}}(t) + \mathcal{K}(\Omega)\mathcal{Q}(t) = \mathbf{0} \tag{3.64}$$

Notice that displacement vector $\mathcal{Q}(t)$, damping matrix $\mathcal{C}(\Omega)$ and stiffness matrix $\mathcal{K}(\Omega)$ are random.

3.3.3 State-space problem

Similarly, for damped free vibration state-space equation may be recast as a stochastic model. Hence, the eigenvalue problem becomes random:

$$\Lambda\mathcal{Z} = \begin{bmatrix} \mathbf{0} & \mathbf{I} \\ -\mathbf{M}^{-1}\mathcal{K}(\Omega) & -\mathbf{M}^{-1}\big(\Omega\mathbf{G} + \mathcal{C}(\Omega)\big) \end{bmatrix} \mathcal{Z} \tag{3.65}$$

Notice the random quantities, such as the eigenvector $\mathcal{Z}$, damping matrix $\mathcal{C}(\Omega)$, stiffness matrix $\mathcal{K}(\Omega)$ and eigenvalues Λ.

Thus, eq. (3.51) is recast as

$$\Lambda_i = -|\Xi_i|\omega_{\mathcal{N}i} - \omega_{\mathcal{N}i}\left(\sqrt{1-\Xi_i^2}\right) j \tag{3.66}$$

where Λ is the random eigenvalue, $\omega_{\mathcal{N}}$ random natural frequency and Ξ random damping ratio.

3.3.4 Unbalance response

The stochastic model for the unbalance response which relates to eq. (3.56) is given by

$$\hat{\mathcal{Q}}(\Omega) = \big[\big(\mathcal{K}(\Omega) - \Omega^2\mathbf{M}\big) + j\Omega\big(\Omega\mathbf{G} + \mathcal{C}(\Omega)\big)\big]^{-1}\hat{\mathbf{F}}_0(\Omega) \tag{3.67}$$

where $\hat{\mathcal{Q}}(\Omega)$ is the random response amplitude, $\mathcal{C}(\Omega)$ random damping matrix and $\mathcal{K}(\Omega)$ random stiffness.

Chapter 4

Rotordynamic analysis results

Both compressors investigated in this dissertation are used in the oil & gas industry for gas reinjection into well reservoir on floating production storage and offloading vessel (FPSO).

4.1 Compressor I

Main characteristics of the first rotor are summarized in table table 4.1:

Table 4.1: Rotor I characteristics

	Values
Operating speed range (rpm)	7080-11400
Young modulus (GPa)	206.8
Shear modulus (GPa)	82.7
Shaft density (kg/m^3)	7833.4
Rotor total mass (kg)	250
Rotor length (mm)	1590.8
Impeller thickness (mm)	25
Impeller outer diameter (mm)	318
Impeller inner diameter (mm)	127
Impeller density (kg/m^3)	7700

The rotor material is an alloy, AISI 4340; the impellers (discs), Virgo 38. The model consists of a shaft-line element with 42 nodes as shown in fig. 4.1 which depicts all the diameters along the rotor. At nodes 4 and 39, locates DE and NDE bearings, represented by red rectangles. The vertical blue dash-dotted lines represent the discs (impellers). Notice that this model does not consider the seals.

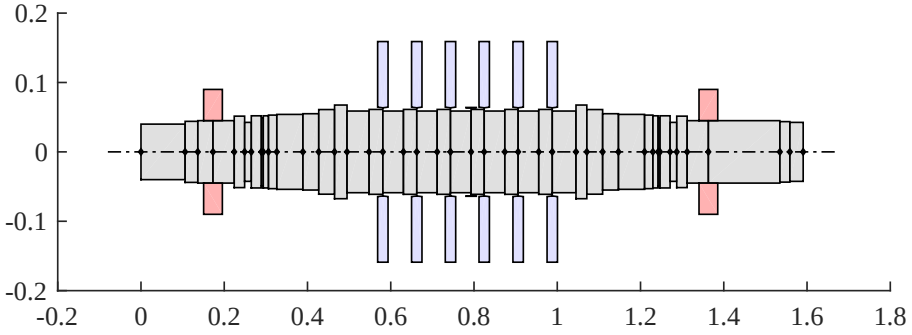

Figure 4.1: Rotor model.

The bearing consists of a tilting pad whose input parameters to the computer fluid dynamics (CFD) analysis is presented in table 4.2:

Table 4.2: Bearing I characteristics

	Values
Bearing type	Flooded
Load type	Load on Pivot
Bearing nominal bore diameter (mm)	90
Bearing length (mm)	39.6
Numbers of pads	5
Pad offset (%)	60
Pad angle (deg)	52
Shaft diameter (mm)	90
Preload	0.645
Diametral clearance (mm)	0.120
Oil type	VG46
Oil inlet temperature (deg)	50
Pivot arrangement	Cylindrical

4.1.1 Deterministic model

The bearing parameters on a deterministic basis need to be provided in order to perform a lateral analysis. These coefficients may be acquired from both XLTRC^2(Texas A&M Engineering Experiment Station) and MAXBRG (University of Virginia) software. The first solves Reynolds equation and the second a thermo-elasto-hydrodynamic (TEHD) as summarized in the last chapter. The thermal effects with heat conduction in the lubricant as wells as pad mechanical and thermal deformation are carried out in the (TEHD) model. Figure 4.2 shows the evaluation for principal axis terms along running speed with regards to the tilting pad bearing model for XLTRC^2 software. Figure 4.3 shows the coefficients for MAXBRG

software. For the second analysis, the damping coefficients are higher along the rotor speed, and the stiffness curve shifts upward. The following studies will assume the MAXBRG coefficients because the model in this software is more complex and realistic.

In general, the stiffness terms increase as shaft speed increments. However, the bearing provides lower damping as rotor accelerates. One explanation would be that the thermal pad deformation decreases the film thickness which increases stiffness and decreases damping to the system. Notice that both stiffness and damping translational terms approximate as the rotor accelerates despite load on pivot bearing yields asymmetric coefficients.

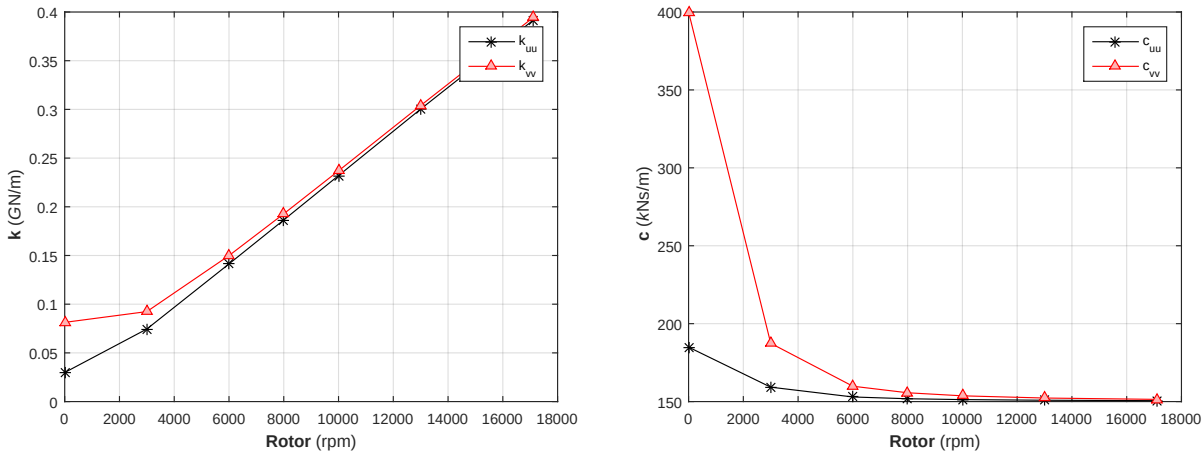

(a) Stiffness × rotor speed.

(b) Damping × rotor speed.

Figure 4.2: Fluid film bearing's parameters - XLTRC²

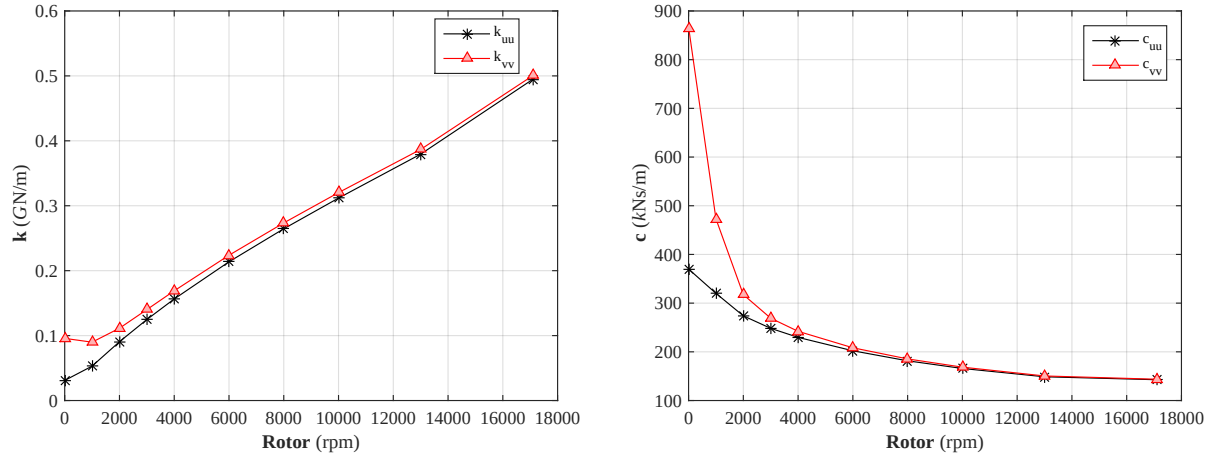

(a) Stiffness × rotor speed.

(b) Damping × rotor speed.

Figure 4.3: Fluid film bearing's parameters - ROMAC

Once the bearing numerical analysis executes accordingly, the definition of the number of nodes takes place to carry out the rotordynamic finite element method.

A Matlab code was written for both the deterministic and the stochastic model.

Figure 4.4 shows that after 40 number of nodes the model achieves convergence for the first critical speed. Therefore, the further stochastic analysis will perform with 42 nodes to spare computational effort.

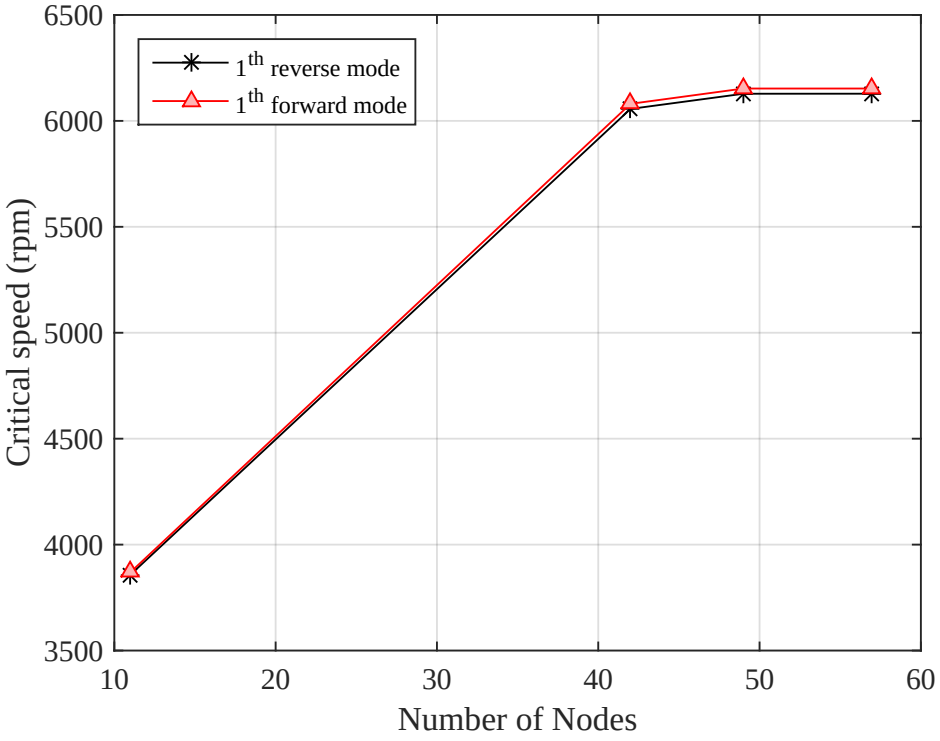

Figure 4.4: Finit element method convergence.

4.1.2 Stochastic model

Monte Carlo

The numerical approach chosen to achieve the output variables probability density functions, $\omega_{\mathcal{N}}$ and $\hat{Q}(\omega)$, is Monte Carlo (RUBINSTEIN and KROESE [18]).

The input to the stochastic model, stiffness, and damping are set as uniform distribution as previously discussed. Therefore, both matrices are built picking a random number for each sample inside the interval proposed. For instance, if the number 1.10 had been picked for stiffness, it would change all stiffness coefficients in the speed range to 10% higher. SILVA [19] developed a stochastic rotor dynamic analysis for correlated coefficients to damper seals. In this paper, the authors constructed a function to represent the coefficients which is a random weighting function of two models of damper seals.

After 500 samples the results for k_{uu} and c_{uu} at 6000 are shown in fig. 4.5, which represents analytical probability density functions f_k and f_c.

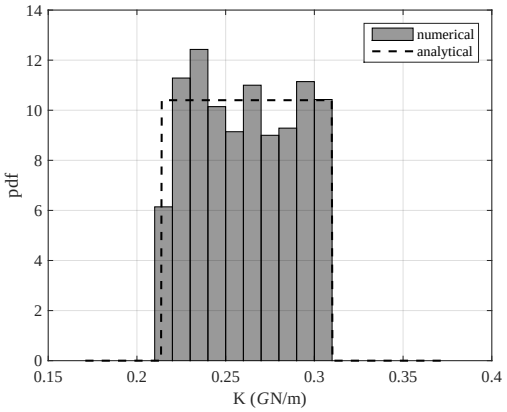

(a) Stiffness probability density function.

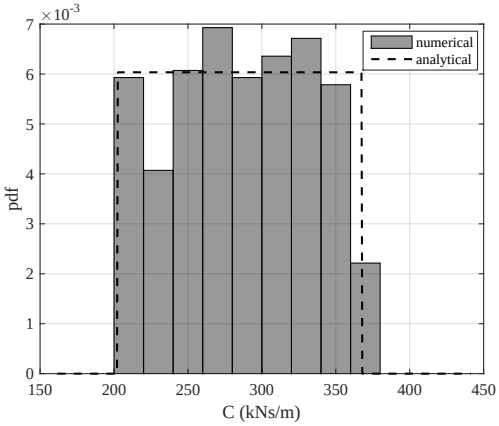

(b) Damping probability density function.

Figure 4.5: Probability density functions (500 samples).

Figure 4.6 shows the translational stiffness and damping terms over the speed range for 500 samples.

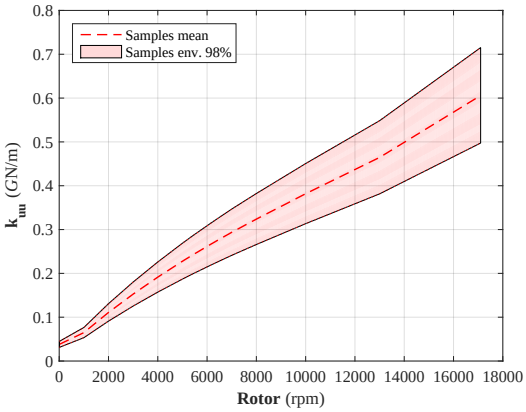

(a) k_{uu} over the speed range.

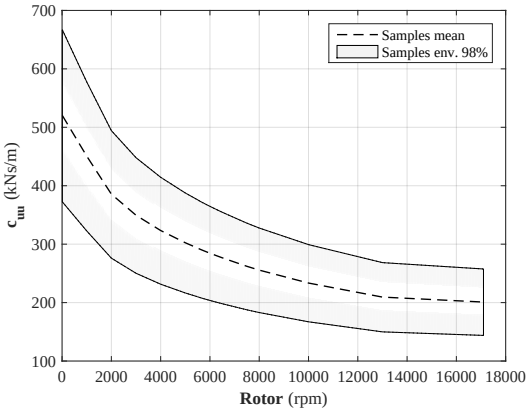

(b) c_{uu} over the speed range

Figure 4.6: Translational terms for 500 samples.

Figure 4.7 shows mean square convergence. Around 500 samples the method has already a reasonable convergence. Notice that the parameter chosen is the forced response amplitude for the fourth node.

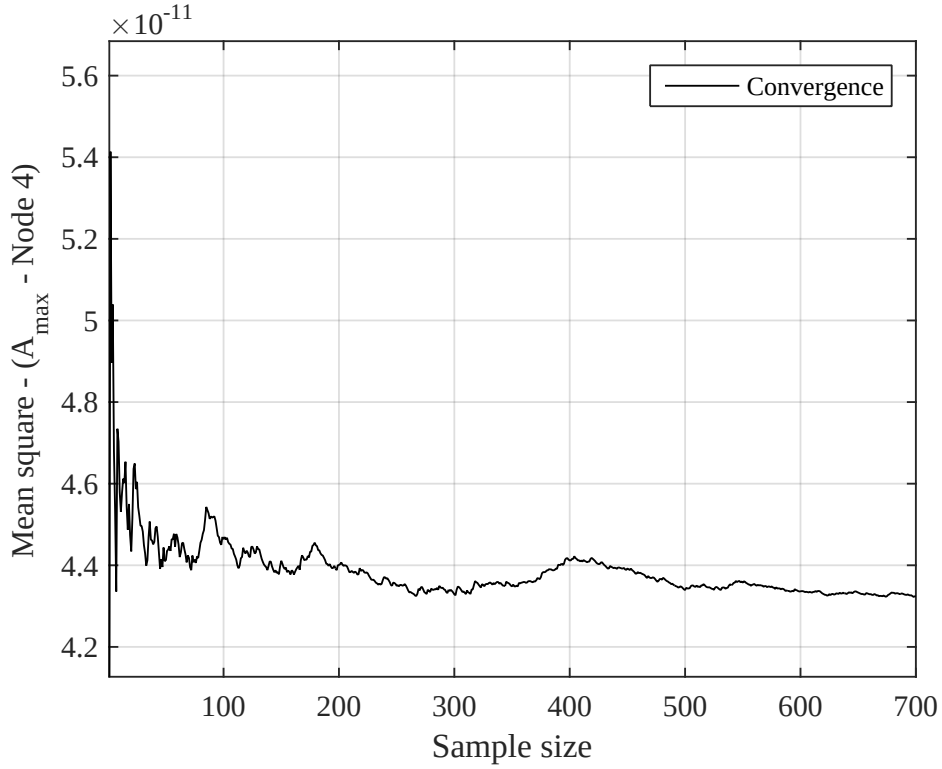

Figure 4.7: Mean square convergence at node's 4 maximum amplitude (500 samples).

Undamped modes

The first analysis which is carried out, seek the first two forward undamped modes. From the state-space problem established on chapter 3 and the uniform distribution of bearing's coefficients, the mode shapes or eigenvectors are evaluated. Figure 4.8 shows the first two forward modes at 6000rpm for 50 samples.

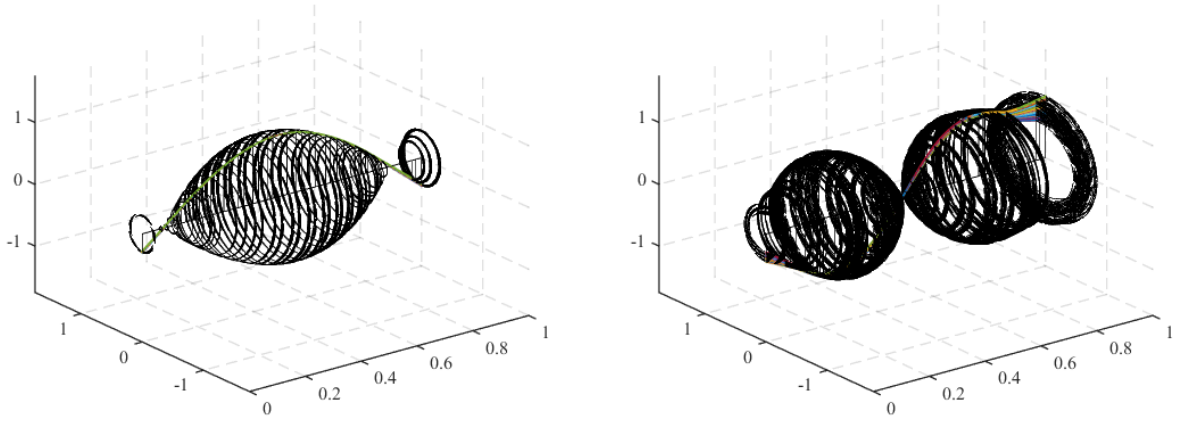

(a) First forward mode.

(b) Second forward mode.

Figure 4.8: Shape modes at 6000 rpm

Regarding the input balance by API 617 [4] standard, the out-of-balance force

to excite the first mode is applied on 22^{th} node which takes place on maximum amplitude. Since second forward mode critical speed occurs after 150% of maximum continuous speed, N_{mc}, which means that influence in oil and gas standard criteria are less critical, further analyses will only excite the first mode.

Uncertain stiffness

Figure 4.9 shows Campbell's diagram, which shows the damped natural frequencies in a free motion within the rotor speed range. Since the stiffness is the random variable, the frequency is stochastic and is shown as a 98% probabilistic envelope for the first forward mode. The red dashed line is 1X speed and therefore, the stochastic critical speed is below the minimum allowable operating speed N_ma .

The damped natural frequency envelope shows a low sensitivity with respect to stiffness distribution.

The second damped natural frequency envelope is higher than the speed range due to low mass value and high stiffness of the rotor, which is related to low bearing span.

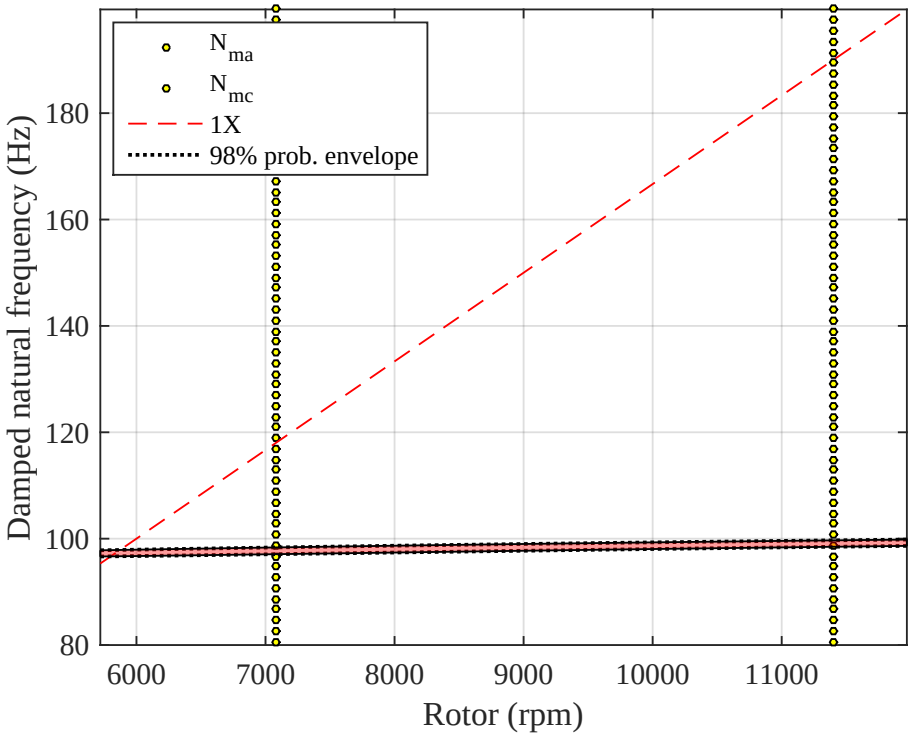

Figure 4.9: Campbell's Diagram for a stochastic damped frequency.

Figure 4.10 shows the Bode plot for the response amplitude of the rotor at the drive-end bearing side. The red dashed line on the top of the plot is the minimum bearing clearance which must be higher than the peak response, i.e., no rub between rotating and stationary parts are allowed in order to prevent damage. API 617 [4]

criterion adds that the scale response which is the multiplication of the peak response by a scale factor S_{cc} shall be within minimum clearance as well. The green horizontal rectangle close to the peak response represents the stochastic scaled response. The vertical rectangle close to the peak response represents required separation margin between operational speed and critical speed SM_r that depends on the amplification factor AF and therefore is stochastic. The grey horizontal dashed line represents the vibration limit A_{v_1} , which is deterministic and should be above the rotor response.

Figure 4.10 shows the 98% envelope of probability for the response amplitude. The maximum amplitude has a reasonable gap from the minimum clearance, red dashed line. Figure 4.11 presents a coefficient of variation, C_v, around 10% over speed range which decreases close to resonance envelope.

Figure 4.10 shows that the required separation margin from critical speed may not meet the API standard criterion. The PDF of both SM_r and SM_a are shown in fig. 4.12. Despite the close distance, a separation margin effectively issues the compressor conformity to this criterion. The deviation of required separation margin can be explained by the effectiveness of the bearing damping when only stiffness varies, which impacts on the amplification factor.

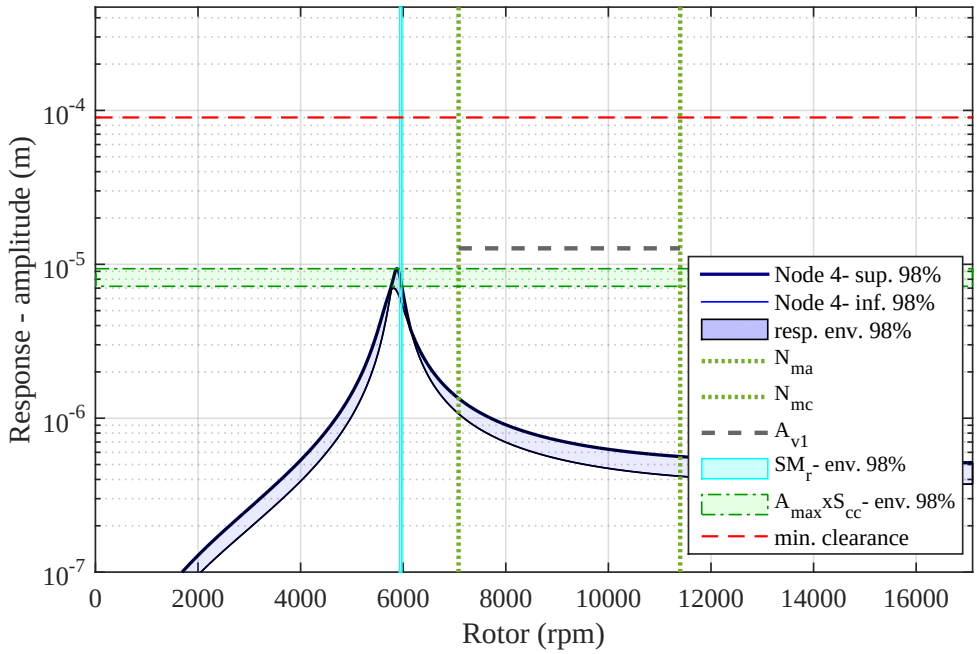

Figure 4.10: Stochastic unbalance response at DE bearing (node 4).

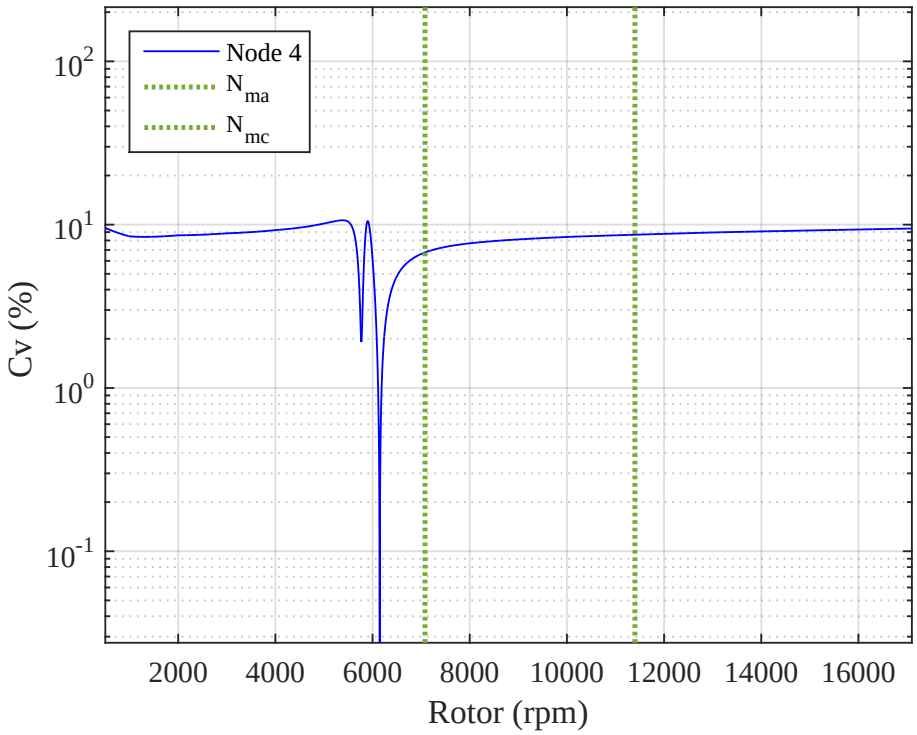

Figure 4.11: Unbalance response coefficient of variation at DE bearing (node 4).

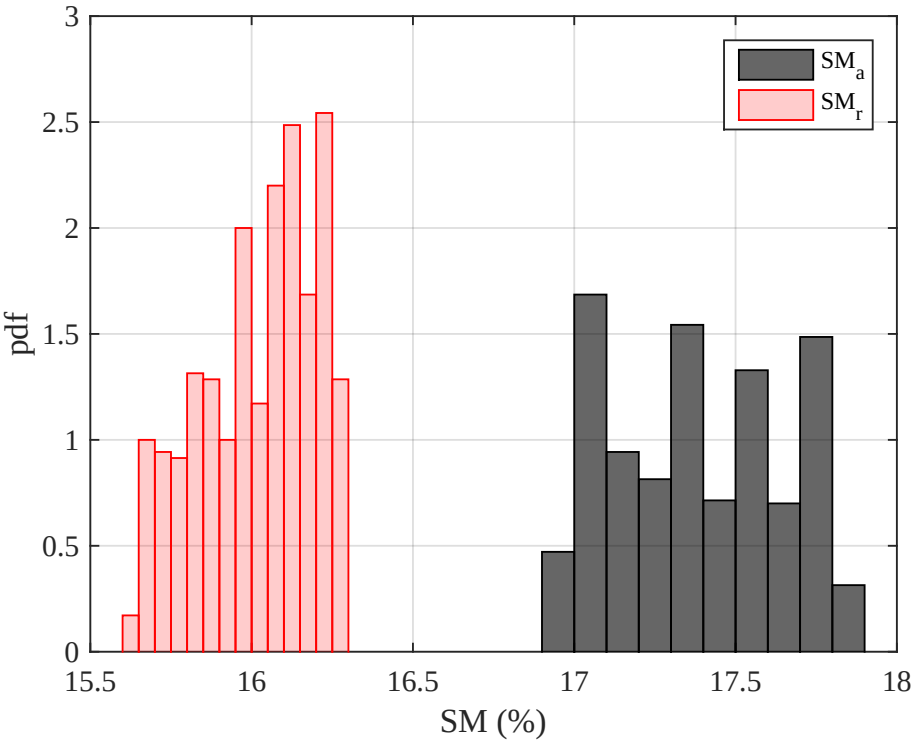

Figure 4.12: Required and actual separation margin PDF's.

Figure 4.13 shows that the amplitude seems to exceed the limit A_{v_1}. However, fig. 4.14 shows a decrease on response variation after the critical speed.

A closer look into fig. 4.15 enlightens the probability that amplitude vibration along the operational speed exceeds the vibration limit criterion. The response distribution density in an undesirable region is significant, which relates to the amount of distribution on the right side of A_{v_1} vertical line. The deviation of the maximum amplitude within operational speed is related to the bearing stiffness variation itself and the critical speed deviation as well.

The coefficient of variation at N_{ma} is 1.62%.

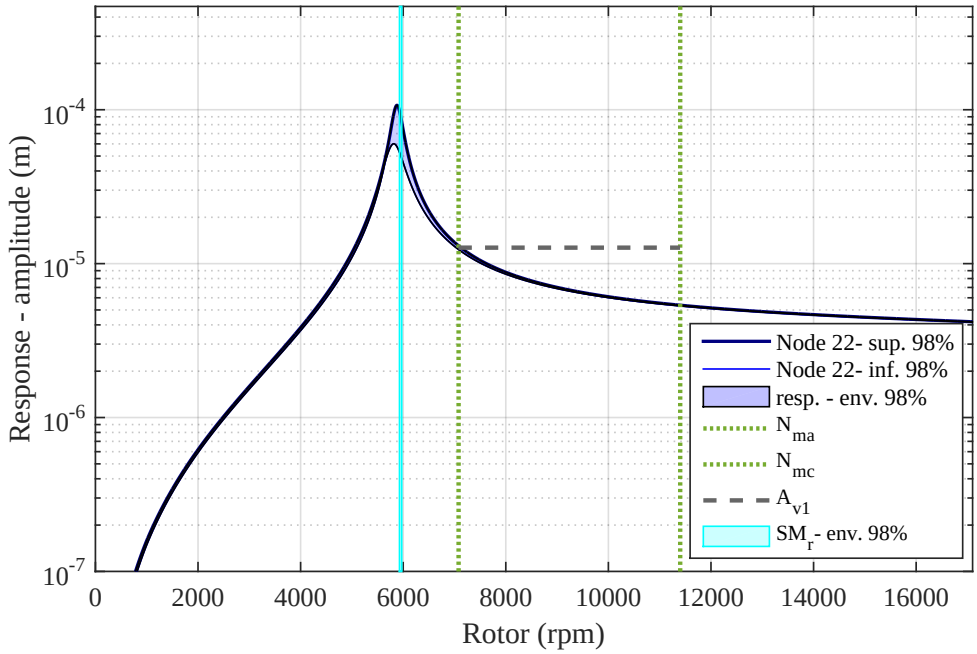

Figure 4.13: Stochastic unbalance response at mid-span (node 22).

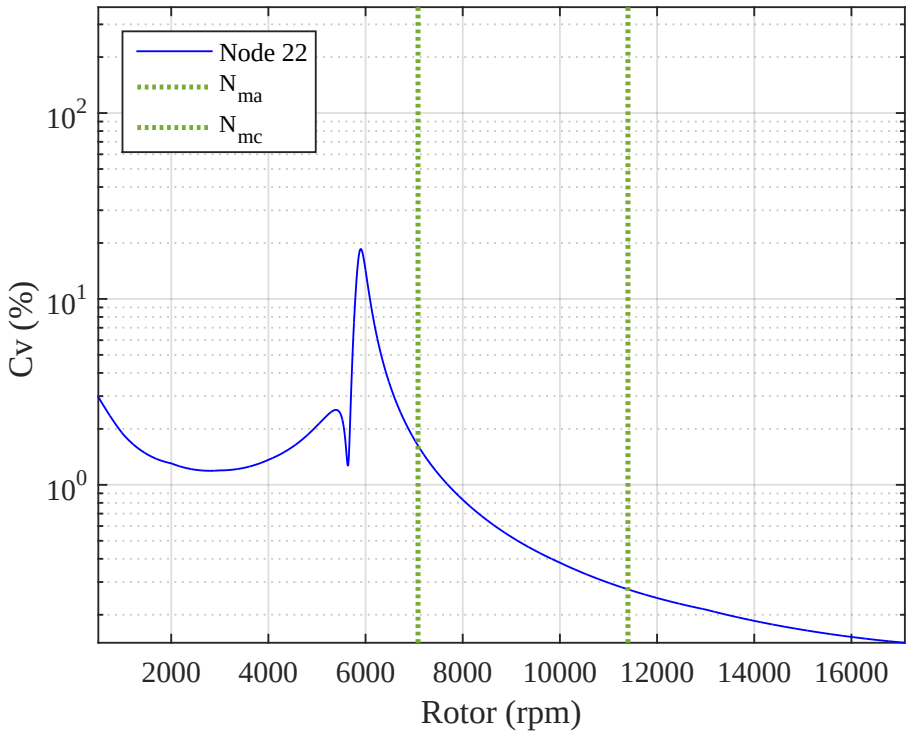

Figure 4.14: Unbalance response coefficient of variation at mid-span (node 22).

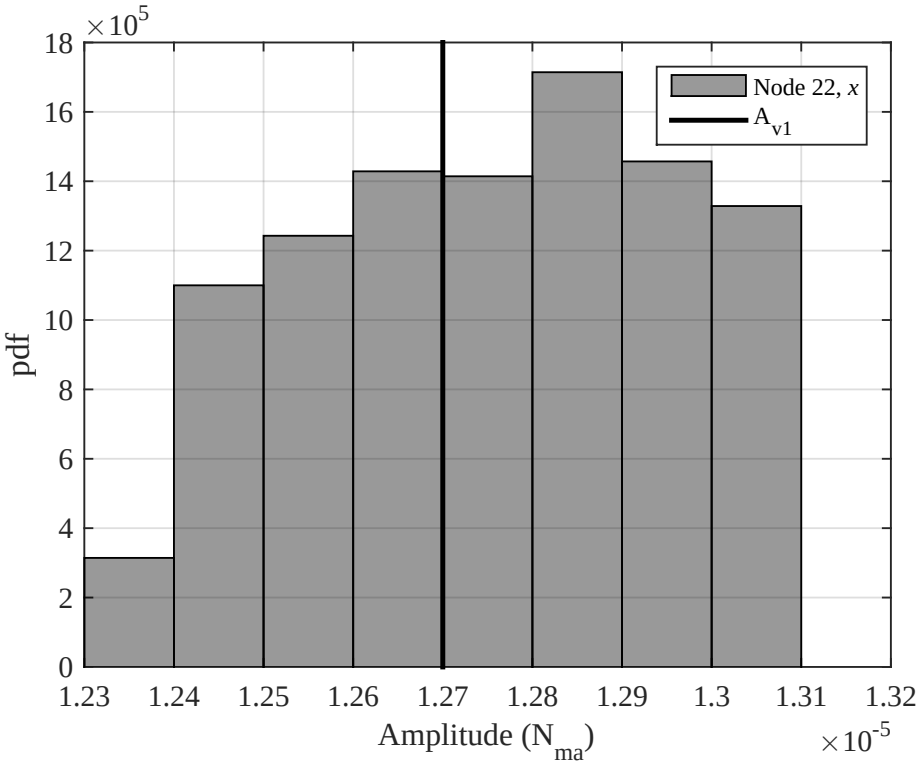

Figure 4.15: Unbalance response PDF at N_{ma} at mid-span (node 22).

Uncertain damping

In this section, the graphics shown are only for an uncertain damping input. The same analyses as the last section will be discussed.

The Campbell's diagram in fig. 4.16 shows an wider envelope area before N_{ma} in comparison to uncertain stiffness case. From operating speed range and beyond, the envelope tends to decrease.

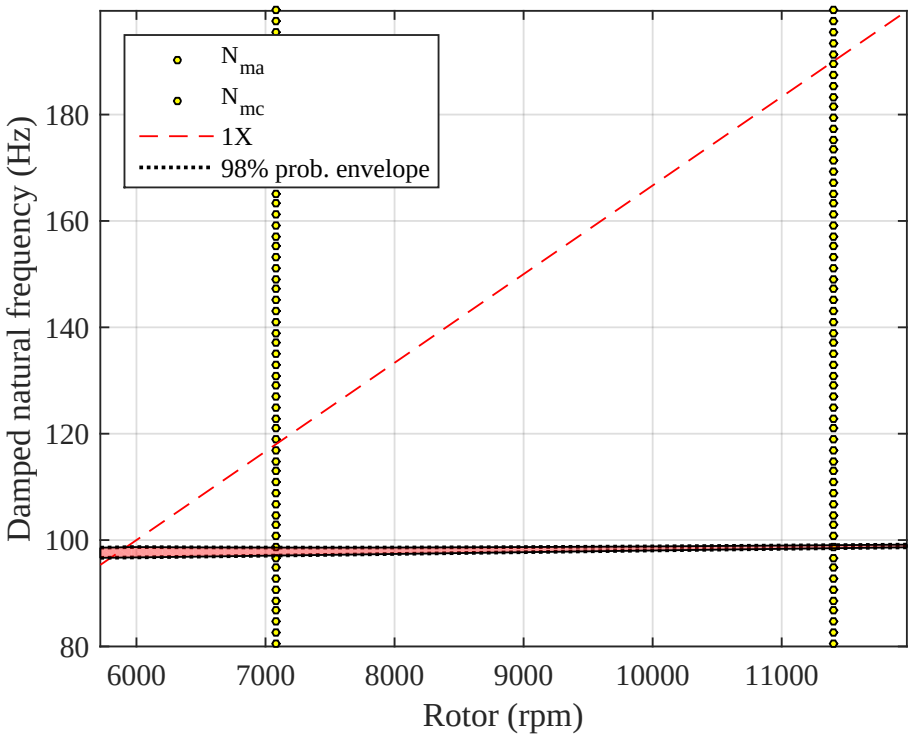

Figure 4.16: Campbell's Diagram for a stochastic damped frequency.

Figure 4.17 shows minimum clearance with a reasonable margin from response amplitude as well as vibration limit A_{v_1} along operational speed range.

Figure 4.18 shows C_v close to 10% from about 2000 rpm rotor speed and decreases nearly to zero deviation about resonance zone. The comparison to uncertain stiffness case shows that response deviation is higher at resonance envelope. However, the envelope amplitude reaches lower values.

The separation margin criterion in fig. 4.19 shows a distribution that seems to be uniform for SM_a. On the other hand, required separation margin presents an asymmetric with shorter deviation distribution. The impact of the stiffness on the efectivess of bearing damping is an explanation to these shorter deviation.

Notice a broader range of critical speed or SM_a for uncertain damping rather than stiffness case which is related to a broader uncertainty interval selected for the damping.

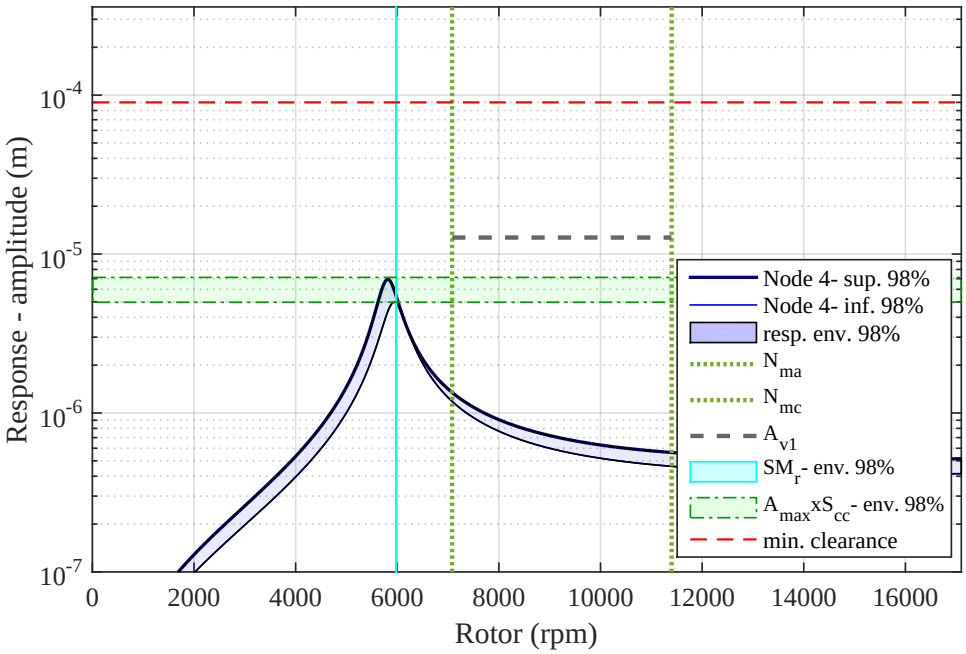

Figure 4.17: Stochastic unbalance response at DE bearing (node 4).

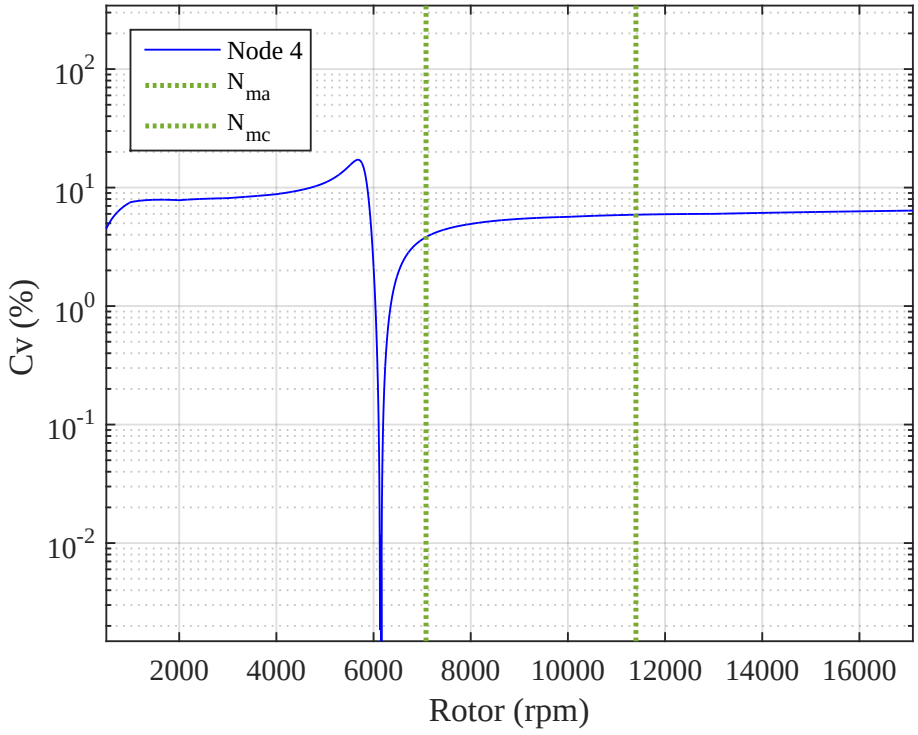

Figure 4.18: Unbalance response coefficient of variation at DE bearing (node 4).

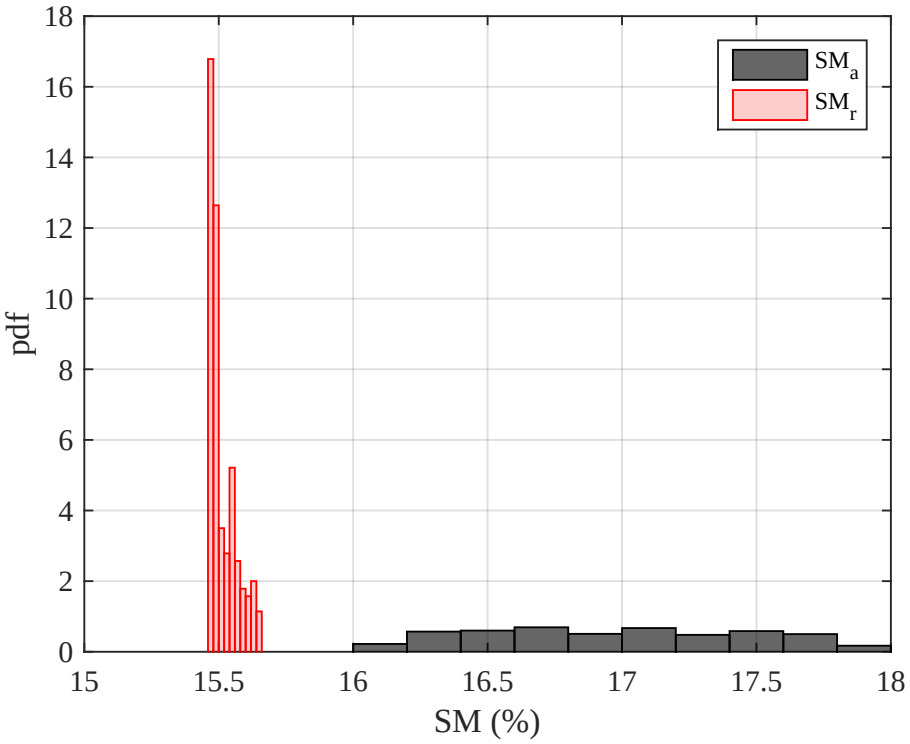

Figure 4.19: Required and actual separation margin PDF's.

Figure 4.20 shows the response amplitude at 22^{th} node which corresponds to the middle of the shaft. Likewise undamped shape mode suggested, when the first mode is excited the response is higher at mid-span and tends to shorten the gap between amplitude and vibration limit A_{v_1} over operational speed. In fact, at minimum allowable speed the probabilistic envelope seems to exceed minimum amplitude criterion even through a decrease on C_v as shown in fig. 4.21.

Figure 4.22 presents PDF for the response at N_{ma} and in comparison to uncertain stiffness case, the right side is wider. Despite the closeness to the modal node, the damping uncertainty is higher and affects critical speed value higher than the stiffness. Therefore, critical speed deviates to shorter margins from operational speed, which increases the response envelope in the minimum allowable speed. Another parameter is C_v which assumes 2.36% at N_{ma}.

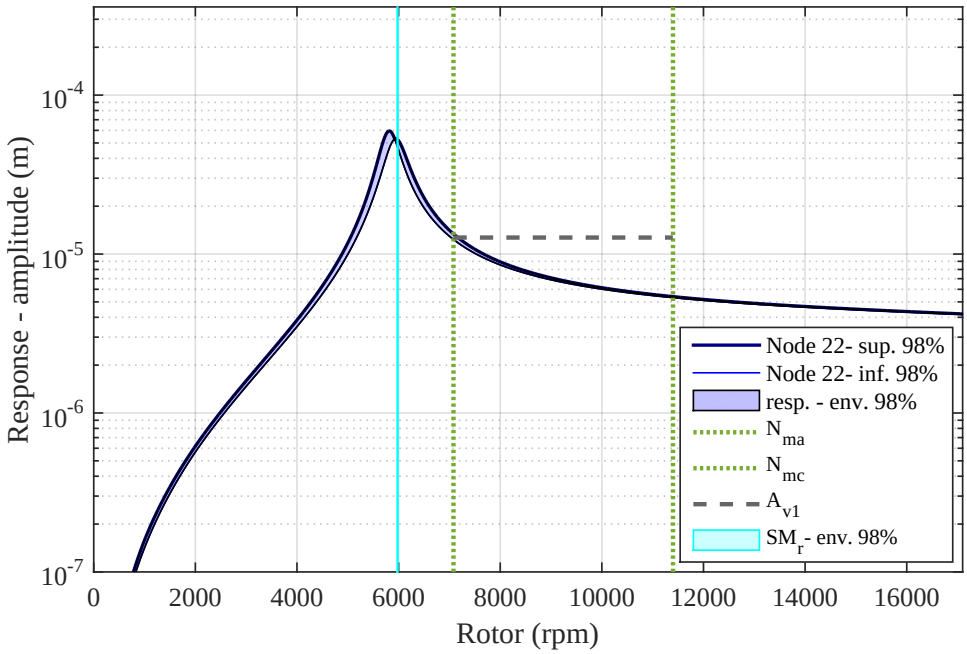

Figure 4.20: Stochastic unbalance response at mid-span (node 22).

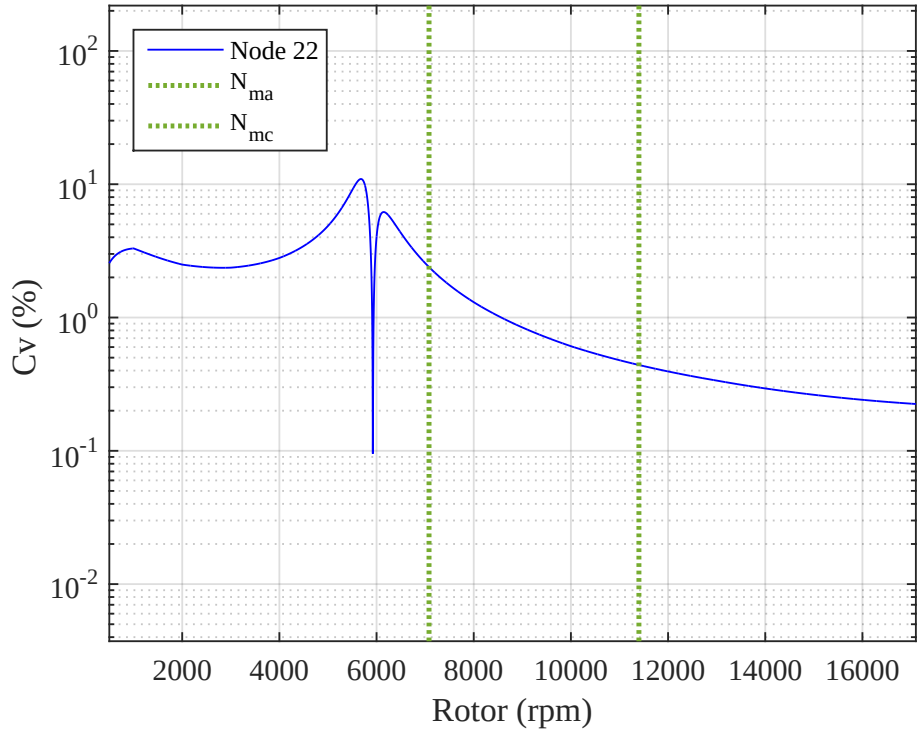

Figure 4.21: Unbalance response coefficient of variation at mid-span (node 22).

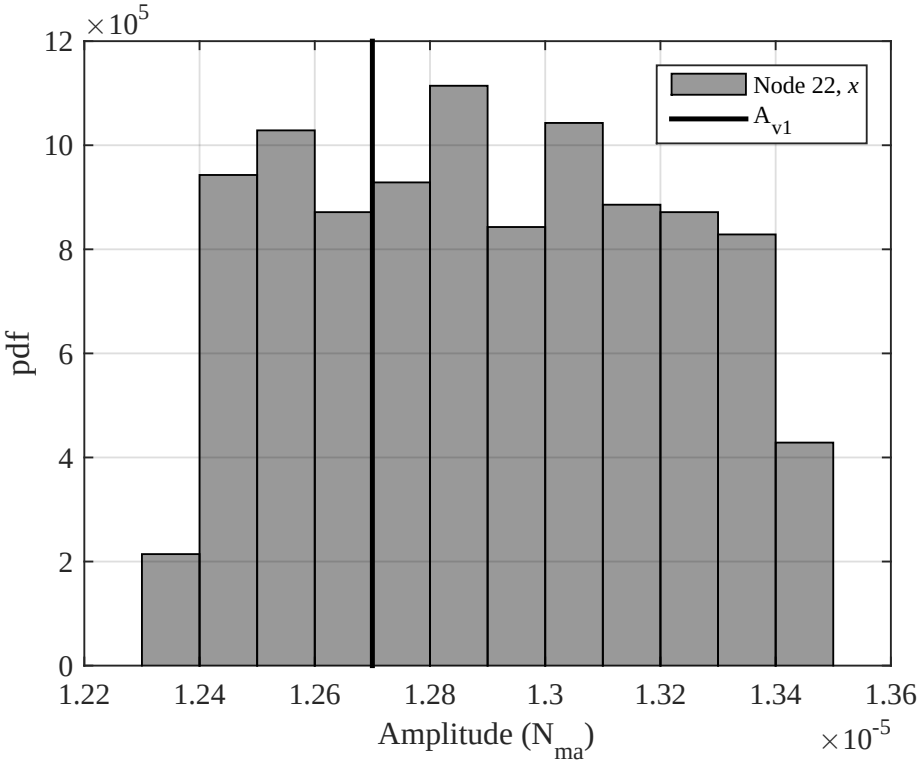

Figure 4.22: Unbalance response PDF at N_{ma} at mid-span (node 22).

Uncertain stiffness and damping

Finally, the analysis starts with both damping and stiffness as uniform distributions. Figure 4.23 shows Campbell's Diagram with similar behavior as the uncertain damping case.

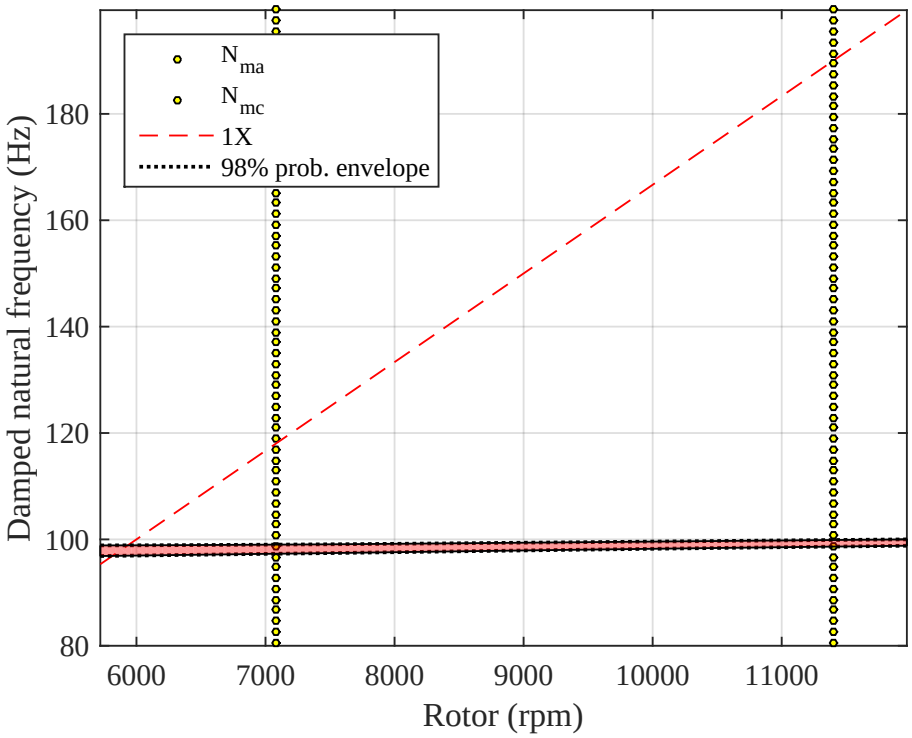

Figure 4.23: Campbell's Diagram for a stochastic damped frequency.

Figure 4.24 as for last section presents minimum clearance at DE bearing with a gap from the maximum amplitude. For maximum amplitude criterion along operational speed the response achieves its higher value at N_{ma}. However, the vibration limit A_{v_1} has a clear gap from the envelope. Figure 4.25 presents a C_v of the response which reaches a peak close to critical speed.

The resonance envelope seems to cross the safe margin to operational speed in fig. 4.24. In fig. 4.26 is clear that actual and required separation margin have an intersection zone which means is probable that the compressor does not meet this API criterion. The major damping influence in the critical speed combined with the bearing stiffness influence on damping effectiveness explains the probability of not meeting separation margin from API 617 [4] standard.

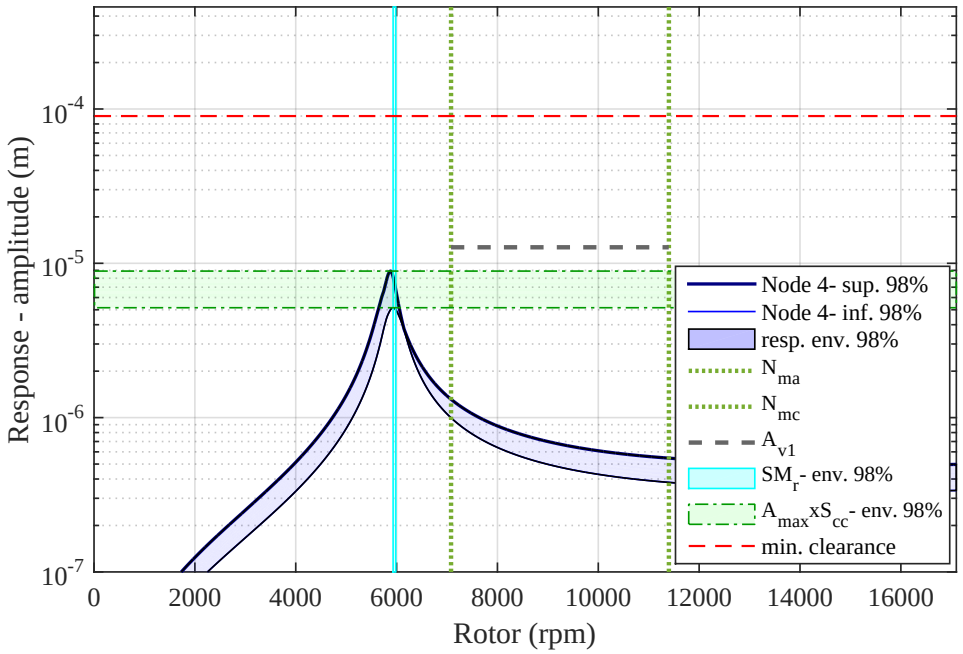

Figure 4.24: Stochastic unbalance response at DE bearing (node 4).

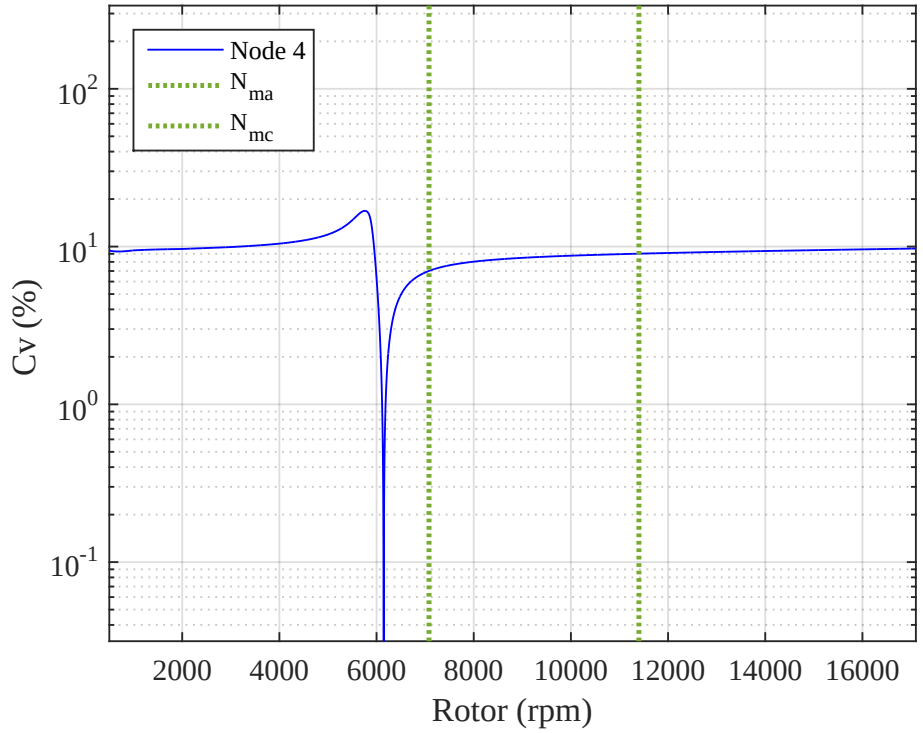

Figure 4.25: Unbalance response coefficient of variation at DE bearing (node 4).

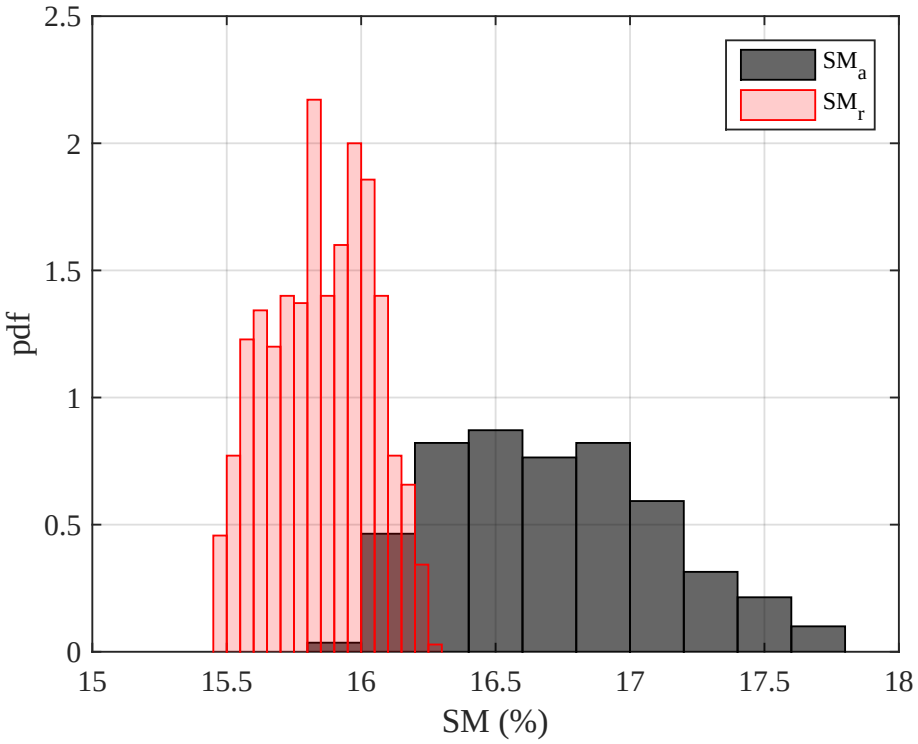

Figure 4.26: Required and actual separation margin PDF's.

Figure 4.27 enlightens that the envelope exceeds the vibration limit A_{v_1} over operational speed. Figure 4.28 shows the response at rotor mid-span from a coefficient of variation perspective. The higher variation is nearly the resonance envelope and decreases to 2.08% at minimum allowable speed, N_{ma}. The PDF in fig. 4.29 shows clearly an asymmetric distribution at minimum allowable speed despite the input being a uniform distribution.

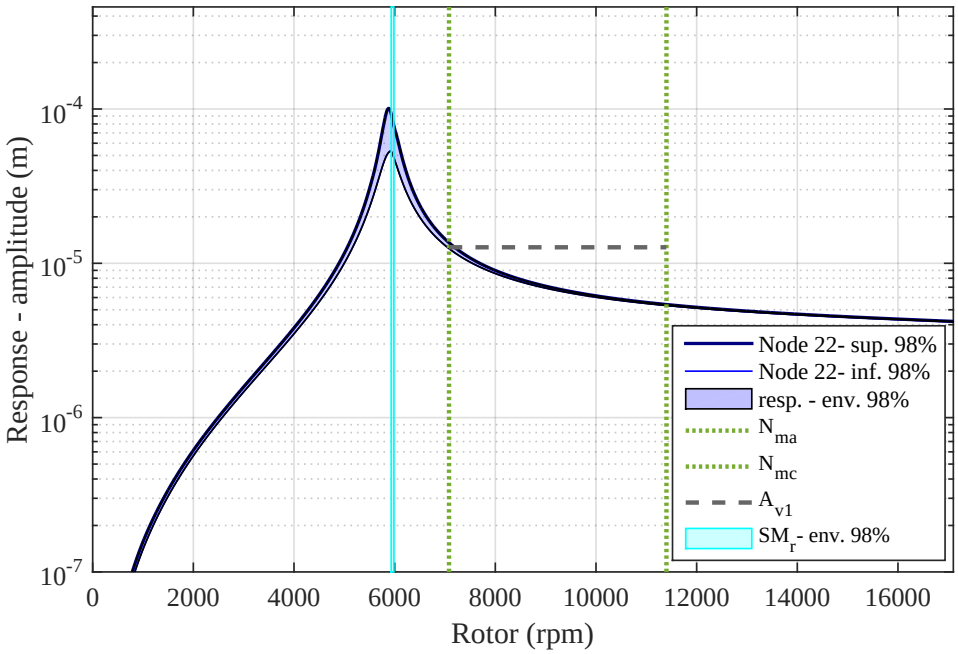

Figure 4.27: Stochastic unbalance response at mid-span (node 22).

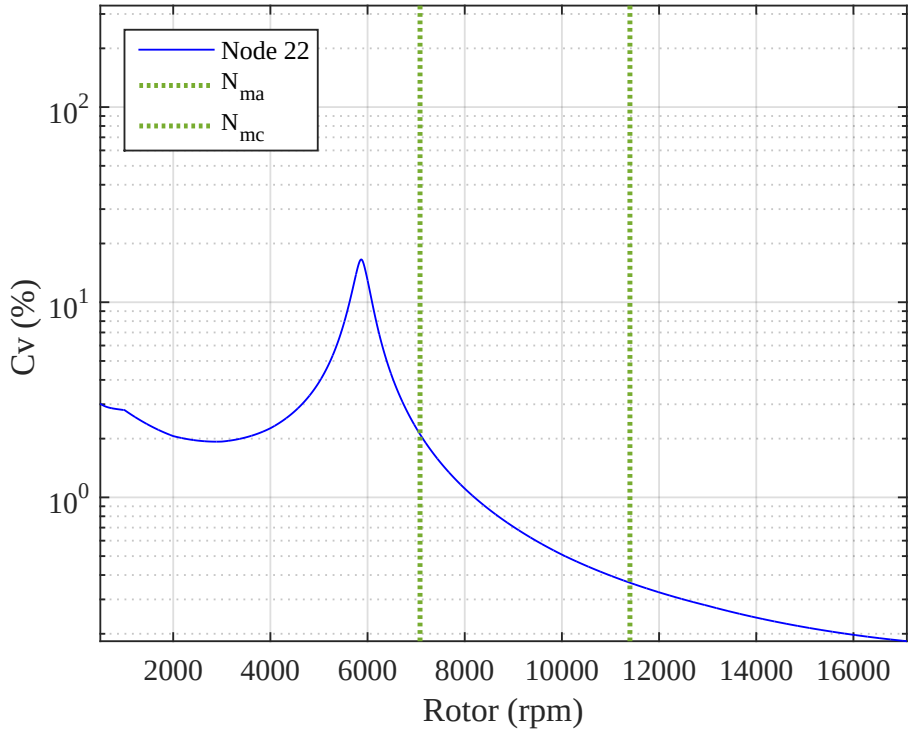

Figure 4.28: Unbalance response coefficient of variation at mid-span (node 22).

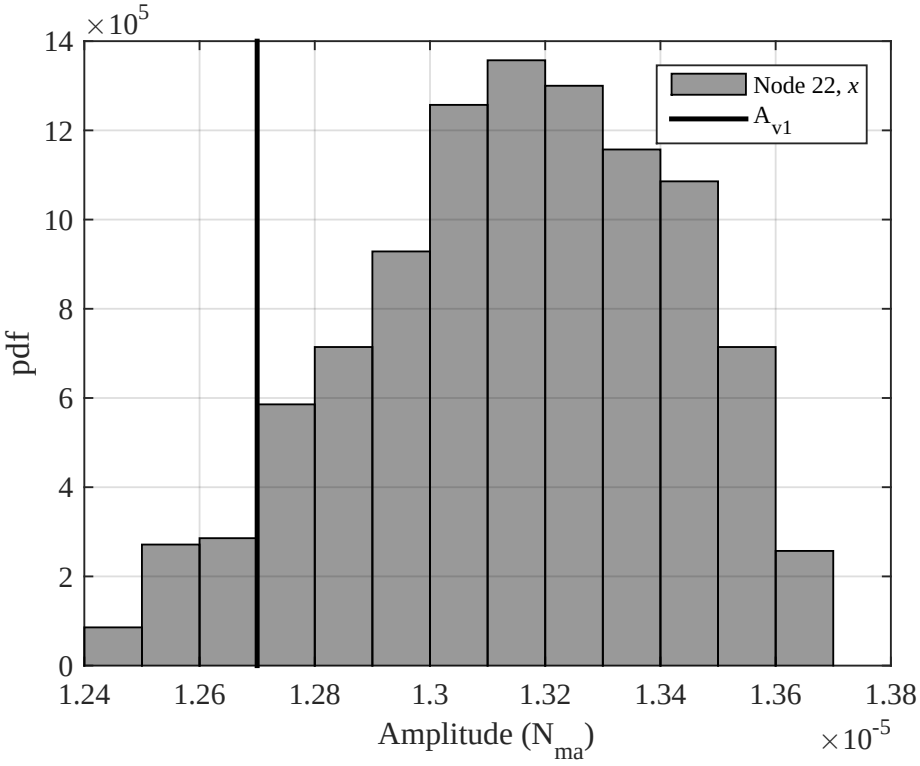

Figure 4.29: Unbalance response PDF at N_{ma} at mid-span (node 22).

Stochastic results analysis

Some conclusions may be detailed from the stochastic analysis developed. Both stiffness and damping impact on the conformity to API 617 [4] standard criteria as shown by damped frequency and unbalance rotor response graphics.

Over operational speed, damping presented more sensitivity to the response output. In comparison, the random stiffness input is less likely to operate with undesirable amplitudes, i.e., above vibration limit A_{v_1}.

From the actual separation margin, damping has also shown higher sensitivity than stiffness due to a broader critical speed "band". For instance, the Coefficient of Variation is 3.06% for damping and 1.51% for stiffness. The damping in the bearing influences the critical speed to shift towards the minimum allowable speed, which raises the vibration levels within operational speed as well.

From the required separation margin view, the random stiffness is more sensitivity due to a higher variation on amplification factor which might be seen in response amplitude nearly critical speed. For instance, the coefficient of variation of required separation margin is 1.12% for stiffness and 0.33% for damping. Besides, the amplification factor coefficient of variation is 16.38% for stiffness and 3.12% for damping. These coefficients of variation support that bearing stiffness influences the damping effectiveness of the system.

Required separation margin presented asymmetric distributions despite either

stiffness and damping have uniform PDF's and the deterministic model is linear. An explanation is that the amplification factor AF which derives the required separation margin is not explicit in the equation of motion.

4.2 Compressor II

The second compressor is similar to the first one whose application is for gas reinjection as well. The Main characteristics of the rotor are summarized in table table 4.3:

Table 4.3: Rotor II characteristics

	Values
Operating speed range (rpm)	7229-11677
Young modulus (GPa)	206.8
Shear modulus (GPa)	82.7
Shaft density (kg/m^3)	7833.4
Rotor total mass (kg)	324
Rotor length (mm)	2148.2
Impeller thickness (mm)	25
Impeller mass (kg)	6.8
Impeller diametral inertia (kg-m^2)	8.7×10^{-2}
Impeller polar inertia (kg-m^2)	4.5×10^{-2}

The main characteristics of the bearings for the TEHD analysis are summarized in table 4.4:

Table 4.4: Bearing II characteristics

	Values
Bearing type	Flooded
Load type	Load on Pivot
Bearing nominal bore diameter (mm)	101.6
Bearing length (mm)	60.3
Numbers of pads	5
Pad offset (%)	0.55
Pad angle (deg)	60
Shaft diameter (mm)	101.6
Preload	0.350
Diametral clearance (mm)	0.140
Oil type	VG46
Oil inlet temperature (deg)	49
Pivot arrangement	Ball-in Socket

The finite element model has 55 nodes as shown in fig. 4.30 which issues the convergence as the first compressor model.

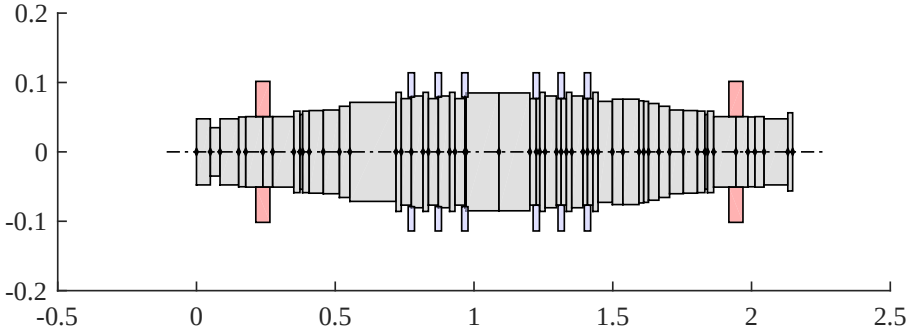

Figure 4.30: Rotor model.

4.2.1 Stochastic model

The uniform probability density functions $f_k \sim \mathcal{U}(1, 1.45)$ and $f_c \sim \mathcal{U}(1, 1.82)$ after 500 Monte Carlo samples are shown in fig. 4.31.

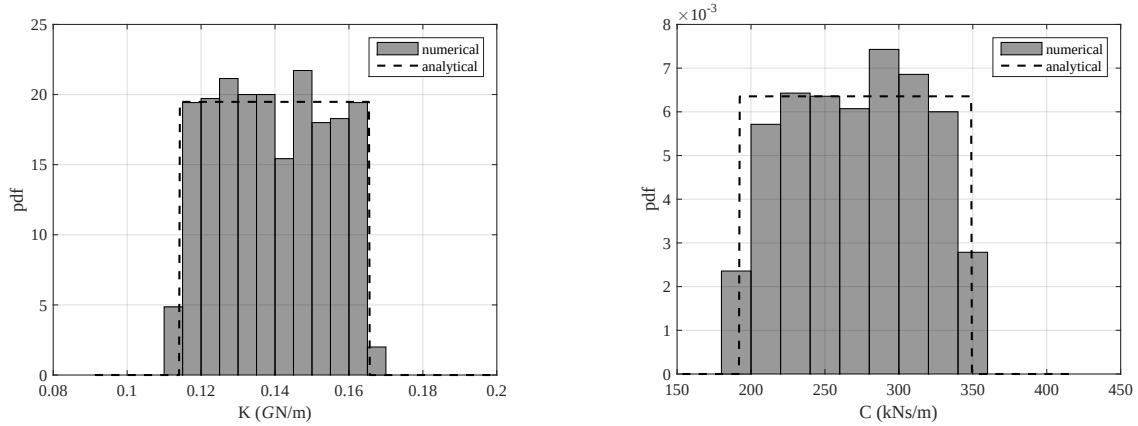

(a) Stiffness probability density function.

(b) Damping probability density function.

Figure 4.31: Probability density functions (500 samples).

Figure 4.32 shows translational bearing coefficients for the Monte Carlos simulations which have similar behavior as the first compressor bearings.

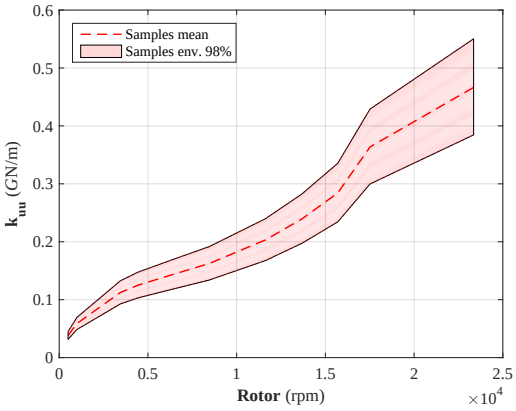

(a) k_{uu} over the speed range.

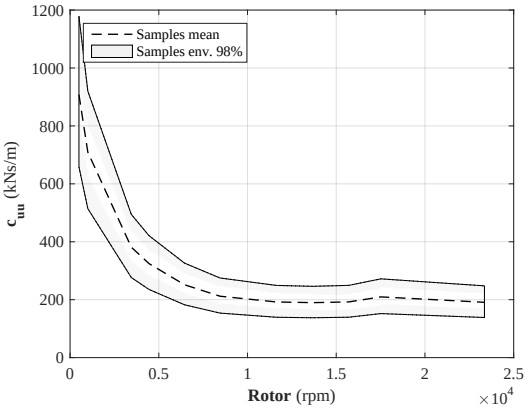

(b) c_{uu} over the speed range

Figure 4.32: Translational terms for 500 samples.

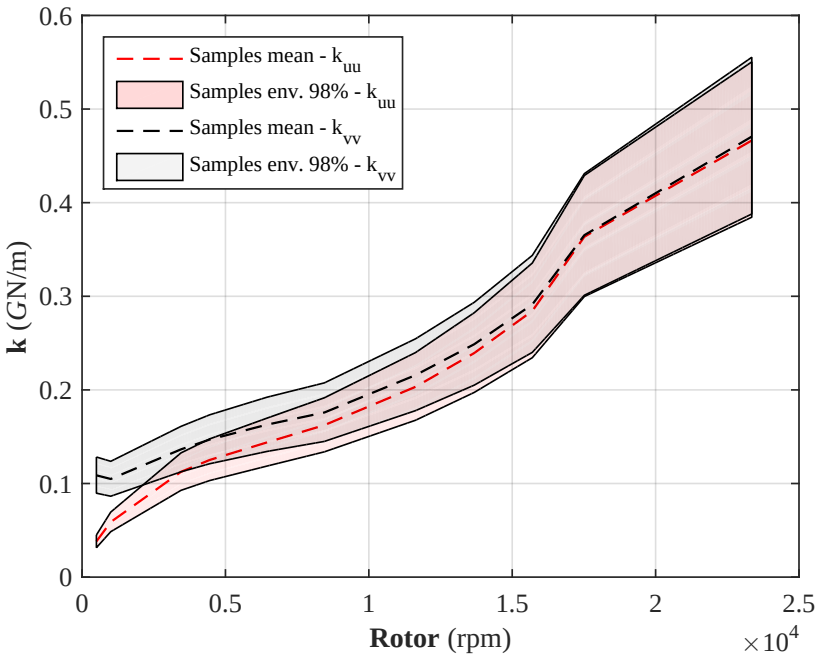

Figure 4.33: Translational terms k_{uu} and k_{vv}.

Undamped modes

The second mode shape in fig. 4.34 shows a softer stiffness than the first compressor as noticed by the larger amplitudes at bearings nodes for 6000 rpm. Since the second mode is within 150% of the maximum operational speed, fig. 4.35 shows these modes for 17000 rpm. The higher speeds are, the higher are translational stiffness coefficients. Therefore, second forward mode approaches a node close to each tilting pad bearings. Notice that for 6000 rpm both mode shapes are flat and at 17000 rpm the modes are round. It occurs due to translational stiffness terms k_{uu} and k_{vv} which are slightly different for lower speeds as shown in fig. 4.33.

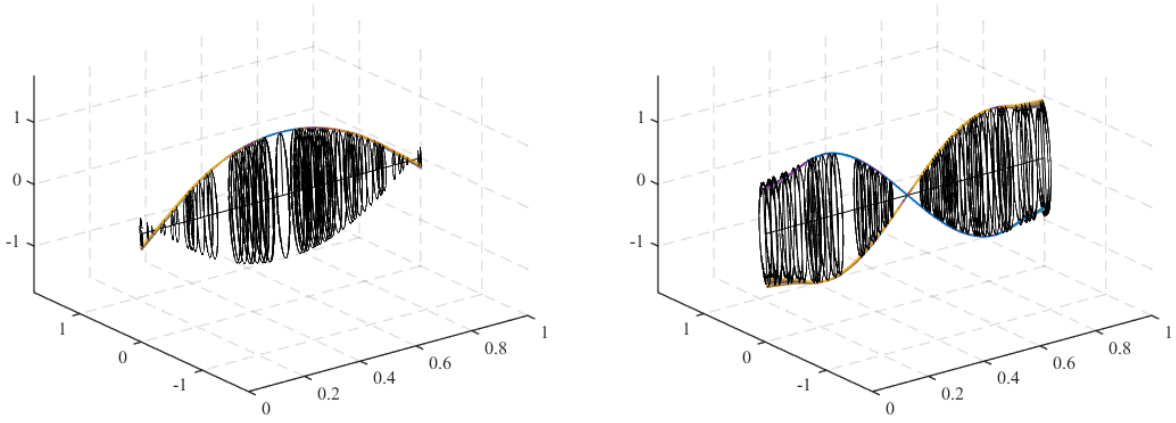

(a) First forward mode. (b) Second forward mode.

Figure 4.34: Shape modes at 6000 rpm

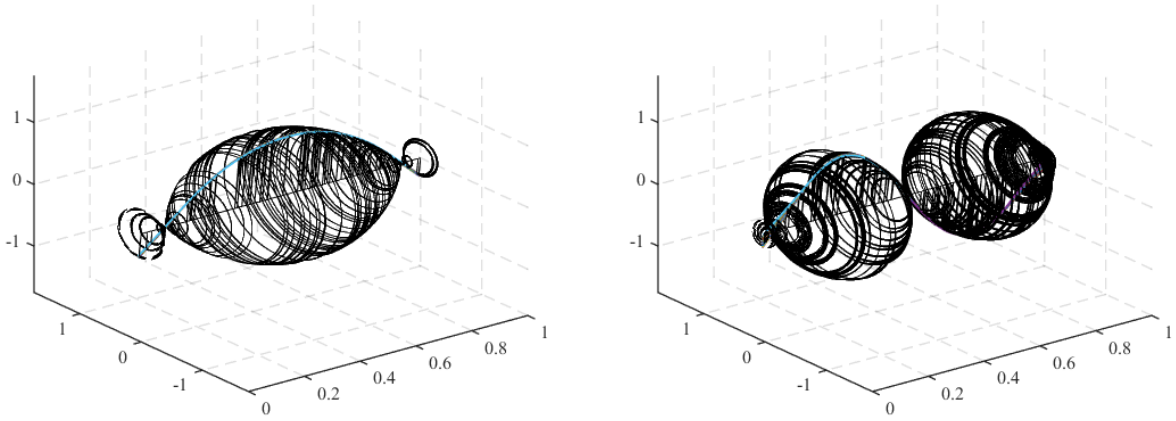

(a) First forward mode. (b) Second forward mode.

Figure 4.35: Shape modes at 17000 rpm

Uncertain stiffness and damping first mode

For the second compressor, the first and second critical speeds are within 150% of the maximum operational speed. Therefore, unbalances are placed to excite the first and second mode are as API 617 [4] standard requires.

The uncertainties only for stiffness or damping coefficients are not analyzed for this compressor since the behavior are similar therewith both variables as stochastic.

The unbalance response at the drive end side bearing is very different from the first compressor. Figure 4.36 shows the critical speed with a wider gap from the required separation margin. One explanation would be that the higher rotor mass and the slender shaft lower the critical speeds and therefore the second mode importance increases as well. Figure 4.37 shows the coefficient of variation which has the

same behavior of the first compressor. Figure 4.38 shows asymmetric distributions whose coefficient of variation is 2.85% for the actual separation margin and 2.41% for the required separation margin. This figure shows a lower required separation margin than the first compressor, which is explained by lower preload. This parameter, when lowered means that the wedge area between the journal and the pad decreases and therefore, the stiffness decreases and the bearing damping becomes more effective.

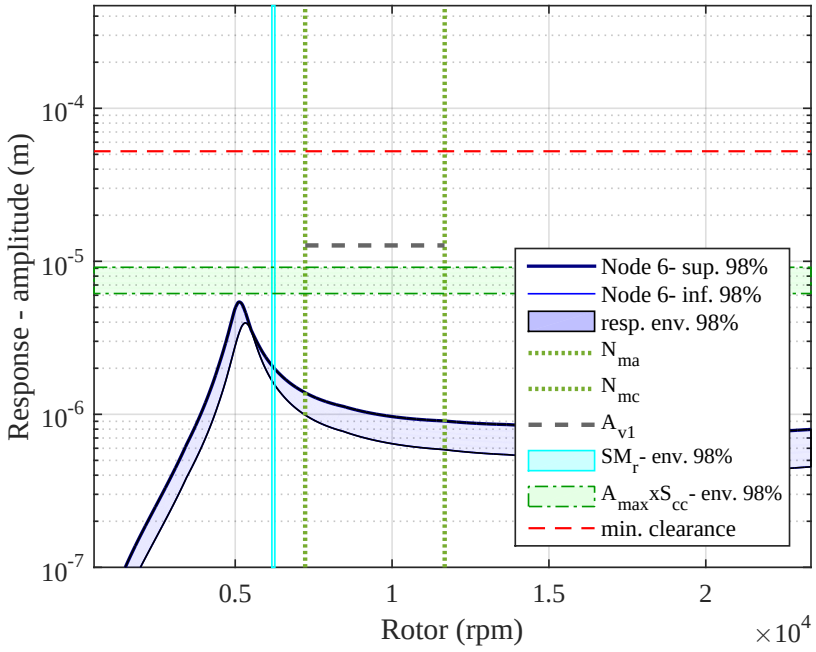

Figure 4.36: Stochastic unbalance response at DE bearing (node 6).

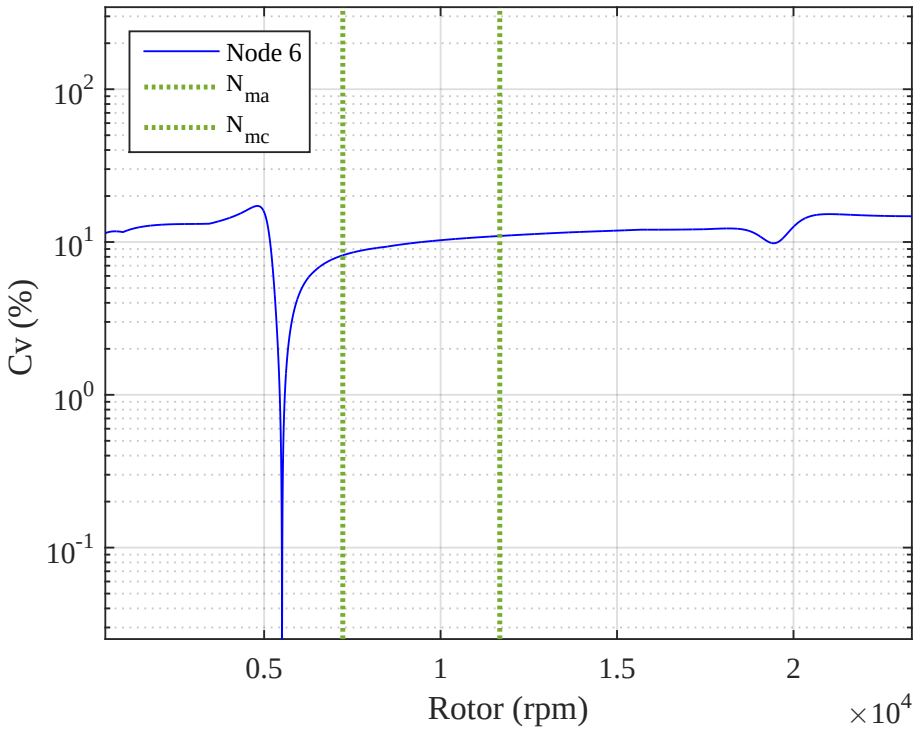

Figure 4.37: Unbalance response coefficient of variation at DE bearing (node 6).

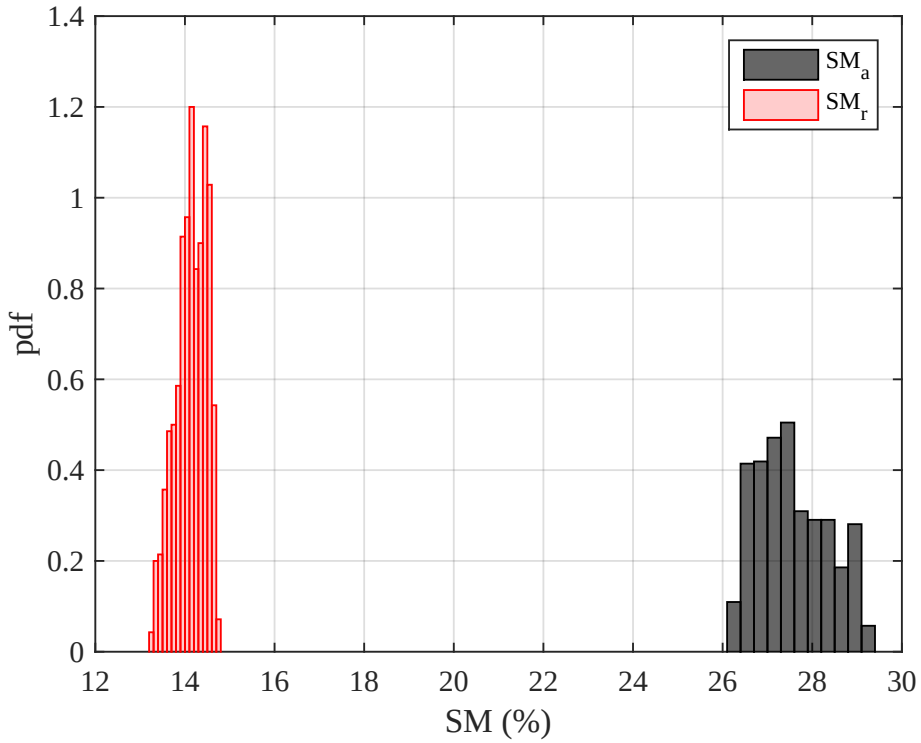

Figure 4.38: Required and actual separation margin PDF's.

Figure 4.39 shows the maximum amplitude envelope within operational speed quite below the vibration limit. In fig. 4.40 the maximum coefficient of variation is

10% which is shorter than the first compressor and fig. 4.41 shows the histogram for the maximum amplitude within operational speed whose coefficient of variation is 2.61%.

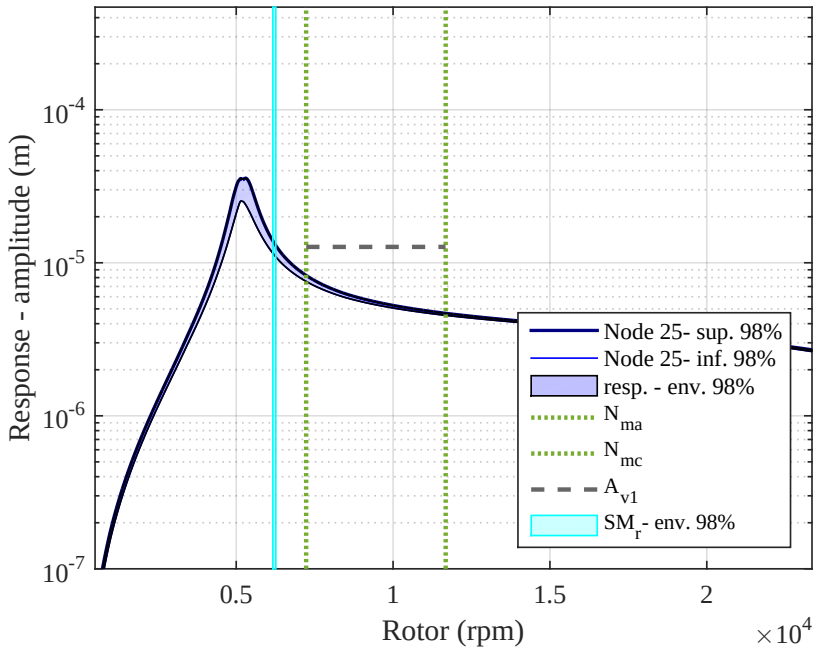

Figure 4.39: Stochastic unbalance response at mid-span (node 25).

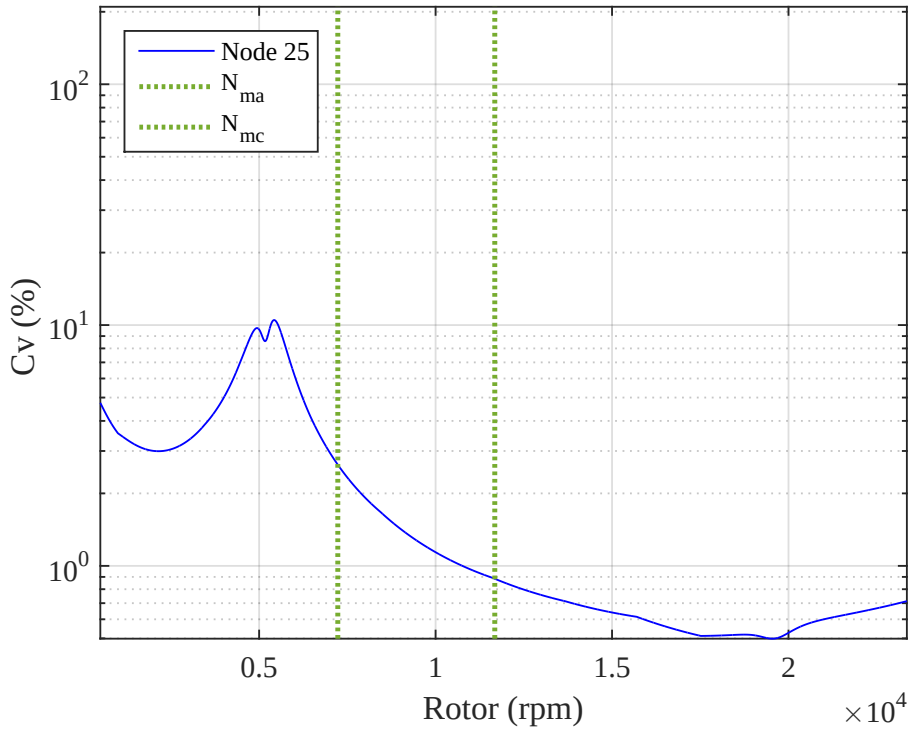

Figure 4.40: Unbalance response coefficient of variation at mid-span (node 25).

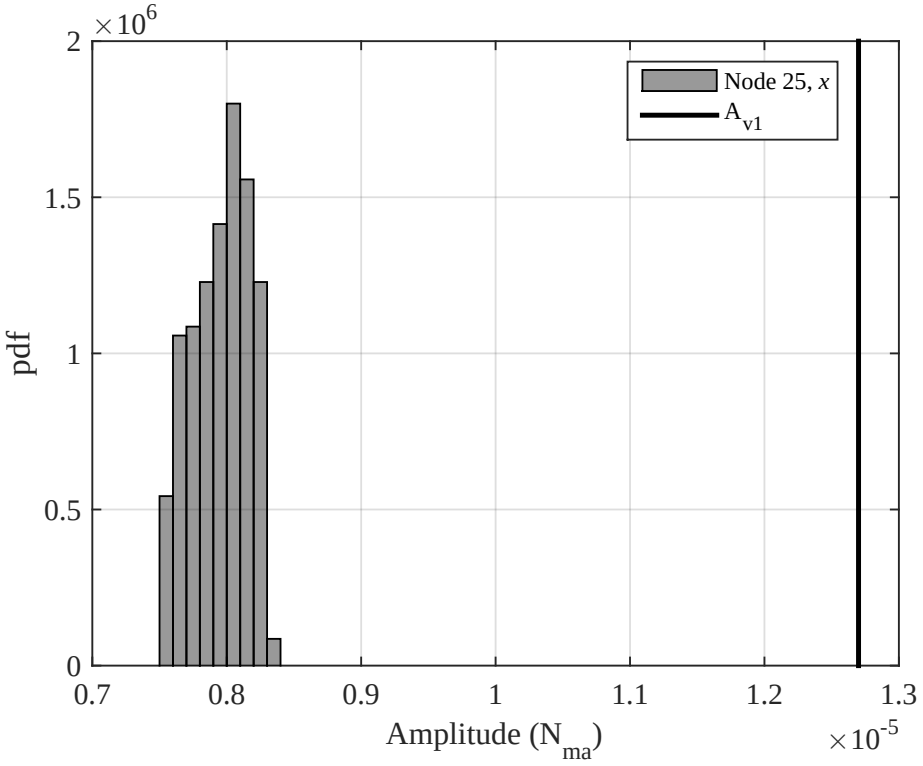

Figure 4.41: Unbalance response PDF at N_{ma} at mid-span (node 25).

Uncertain stiffness and damping second mode

The unbalances are placed out of phase to excite the second mode. The second critical speed is closer to operational speed than the first compressor; therefore the API 617 [4] criteria conformity are checked as well. Figure 4.42 shows the response at drive end side bearing which displays the actual separation margin higher than the required. Figure 4.43 shows the response coefficient of variation above 10%, excepts in the neighboorhood of the critical speeds.

The vibration limit is not an issue to the standard conformity. However, the scale response is closer to the bearing clearance. Figure 4.44 shows the scale response PDF which does not exceed the bearing clearance.

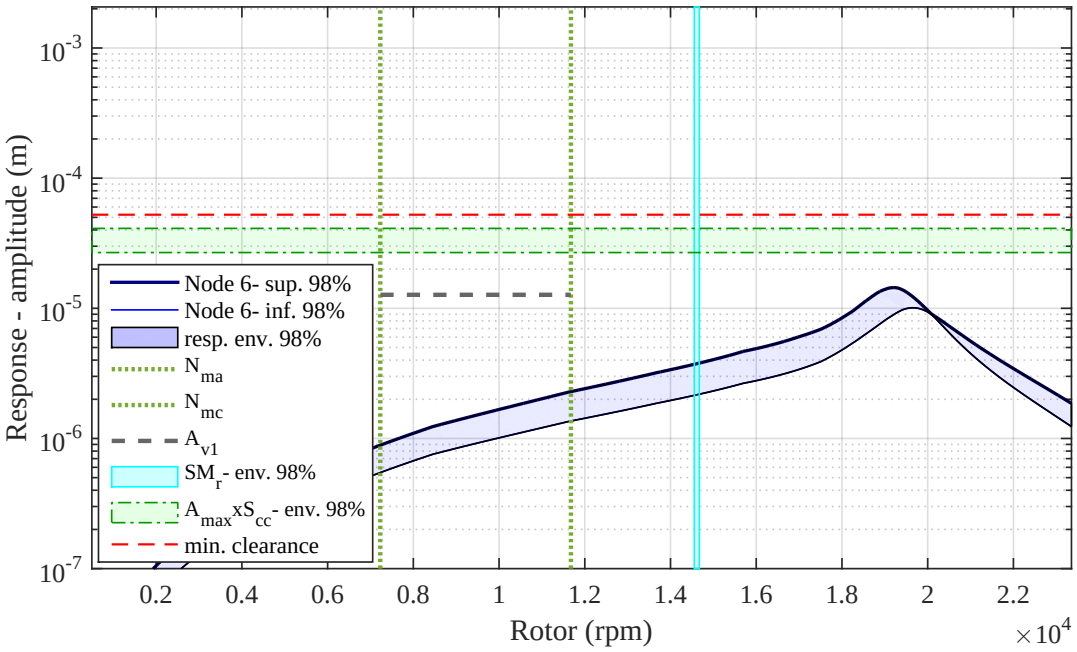

Figure 4.42: Stochastic unbalance response at DE bearing (node 6).

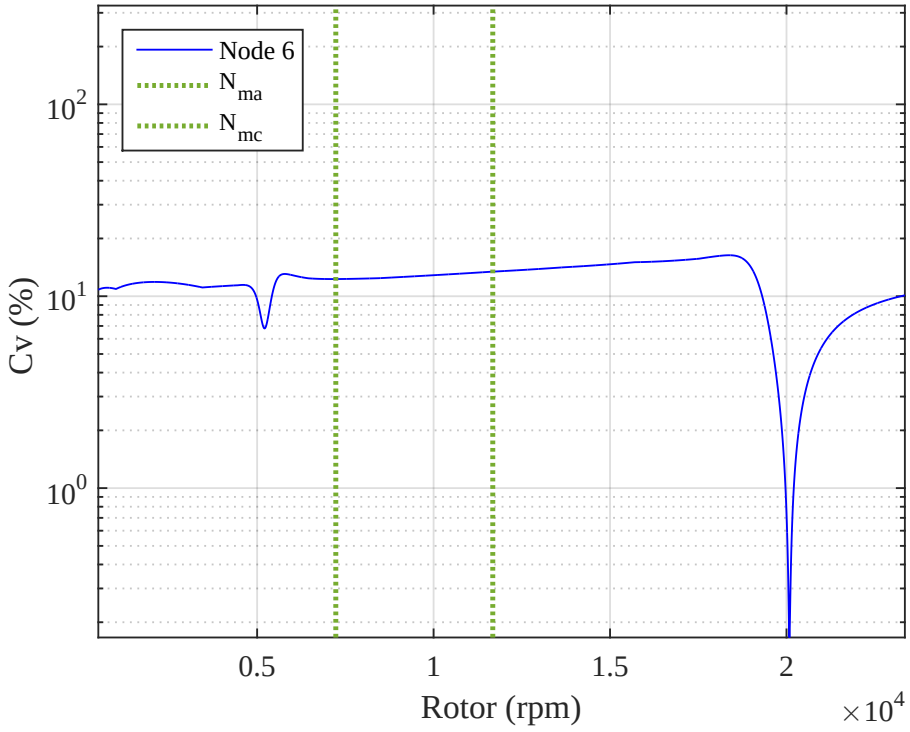

Figure 4.43: Unbalance response coefficient of variation at DE bearing (node 6).

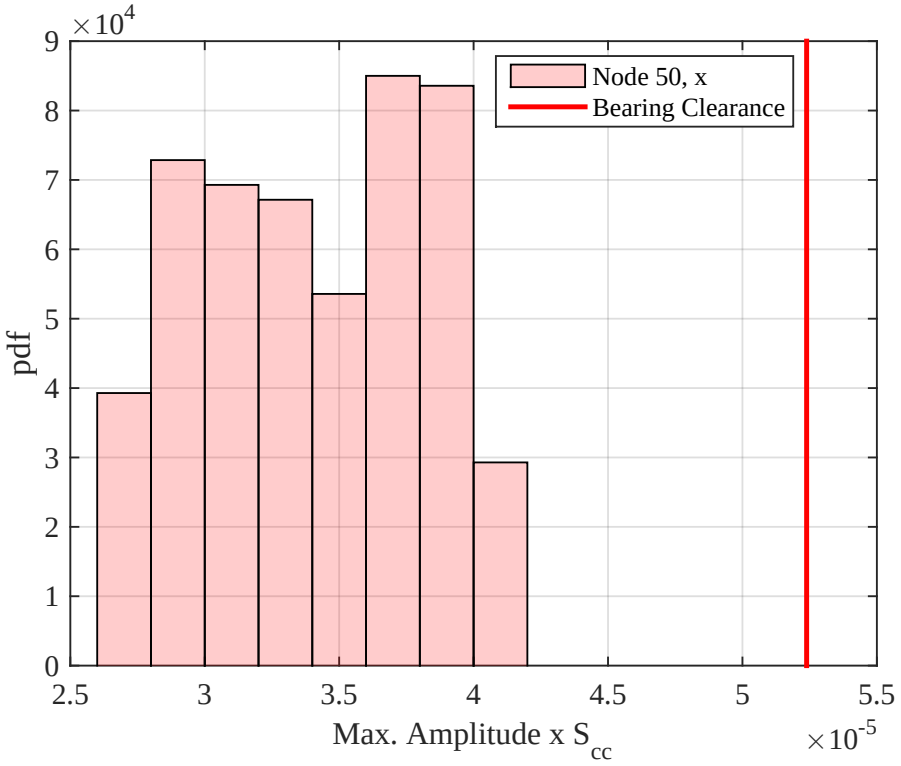

Figure 4.44: Scaled response PDF (node 50).

4.3 Injection compressors results

To summarize main differences between the two injection compressors, the uncertainties on bearings coefficients does not exceed API 617 [4] limits for the second compressor.

The second compressor design leads to critical speeds that provide a safer margin to operational speed which is coherent to a more massive and slender rotor whose effect is to decrease the damped frequencies. The lower preload on the bearings of the second compressor increases the effectiveness of the damping, which cooperates with a safety design. However, during their life cycles the compressors may achieve higher unbalance magnitudes than the ones that run on test bench of manufacturers, and therefore the minimum clearance variation could be checked in advance. The probability of not meeting API 617 [4] criteria for the first compressor concerning vibration limit and separation margin to critical speed could be checked as well. Figure 4.45 shows the difference between the first and the second compressor in a separation margin mean basis. Figure 4.46 shows the gap between the vibration limit A_{v_1} and the maximum response within operational speed for both compressors models as well. Both figures stress how tight are the margins of the first compressor to API 617 [4] criteria.

In order to evaluate rotor probability of not meeting API 617 [4] criteria the

reliability methods (rare event estimation) First-Order Reliability Method and Importance Sampling will be analysed.

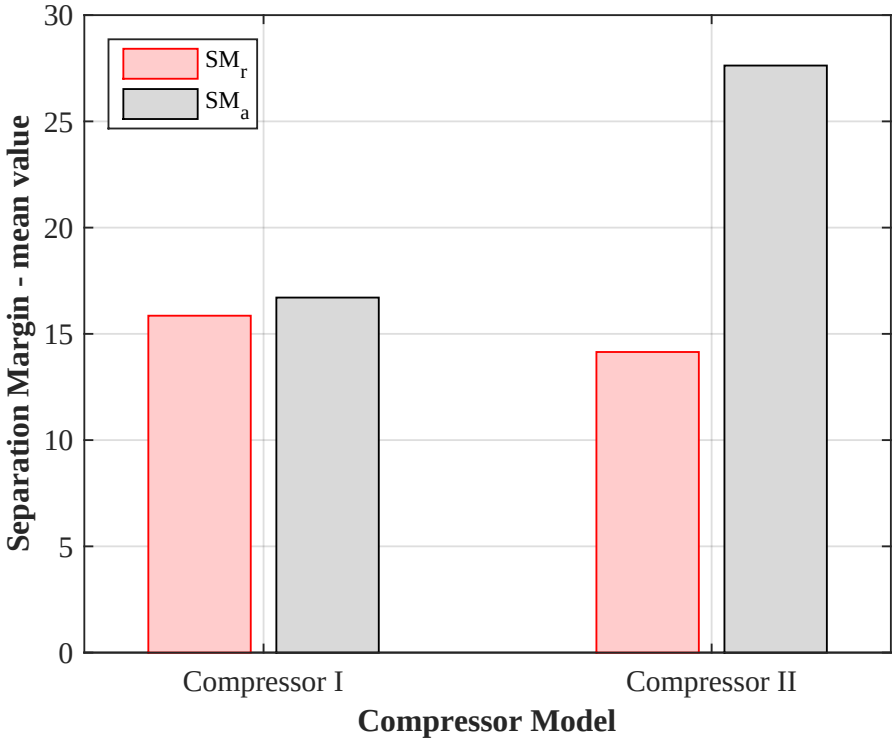

Figure 4.45: Compressors separation margin mean value

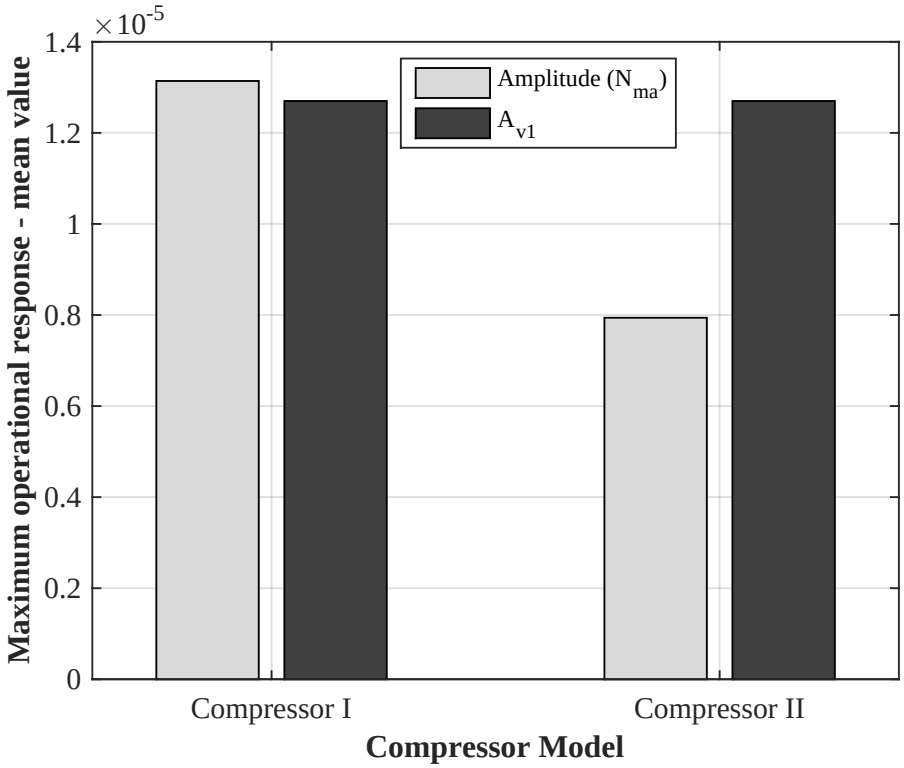

Figure 4.46: Compressors maximum amplitude mean value within operational speed

Chapter 5

Rare event estimation

The Monte Carlos method is one of many approaches to evaluate the probability of failure. A useful tool was developed during the research in reliability analysis to estimate rare event probability (MELCHERS [5]).

The goal of structural reliability is to evaluate whether the structure response will cause a collapse, damage, fail. Each requirement of failure represents a limit-state function. For example, if R represents the resistance of a structure and S the load, the limit-state function is $G = R - S$. The limit function and the failure domain for this bivariate distribution are shown in fig. 5.1. Whenever the limit state function is negative, the structure is in collapse. Following this example and considering R and S probability density distribution, and the failure domain D is possible to define the failure probability as

$$p_f = P(R - S \leq 0) = \int_D \int f_{RS}(r, s) dr ds \tag{5.1}$$

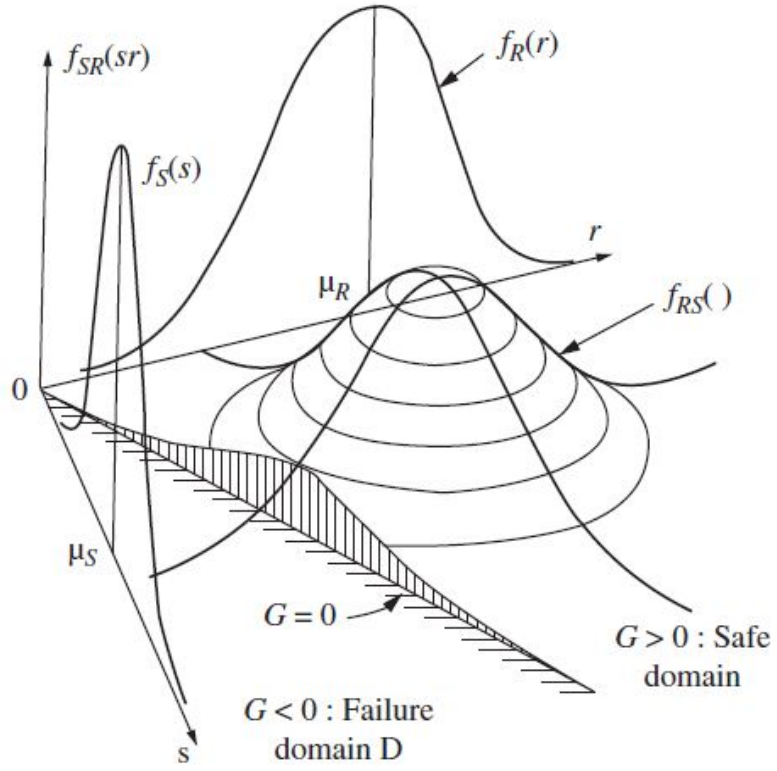

Figure 5.1: Space of the two random variable (r,s) and the joint density function $f_{RS}(r, s)$, the marginal density functions f_R and f_S, and the failure domain D MELCHERS [5].

Let the distributions of R and S be normal random variables with μ_R and μ_S means, and σ_R^2 and σ_S^2 variances. Thus, considering $Z = R - S$ and the property that every normal distribution may be shifted to a zero mean and unit standard deviation, the probability of failure is

$$p_f = P(R - S \leq 0) = P(Z \leq 0) = \Phi\left(\frac{0 - \mu_Z}{\sigma_Z}\right) \tag{5.2}$$

$$= \Phi\left(\frac{-(\mu_R - \mu_S)}{(\sigma_R^2 + \sigma_S^2)^{1/2}}\right) = \Phi(-\beta) \tag{5.3}$$

where Φ is the cumulative normal distribution with zero mean and unit variance and β is defined as the "safety index" which determines the probability of failure as illustrated in fig. 5.2 by the shaded area.

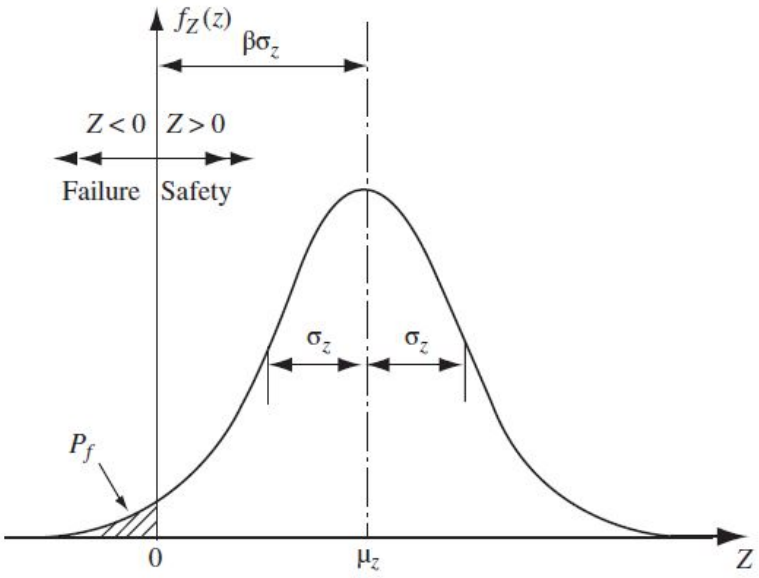

Figure 5.2: Probability density function of safety margin $Z = R - S$ MELCHERS [5].

A usual method to estimate the probability of failure is Monte Carlo whose definition states in eq. (5.4) for multidimensional uncertain variable $\mathbf{X}$ and the limit state function $G(\mathbf{X})$.

$$p_f = P(G(\mathbf{X}) \leq 0) = \int \cdots \int_{G(\mathbf{X})\leq 0} f_{\mathbf{X}}(\mathbf{x}) dx \tag{5.4}$$

5.1 Monte Carlo

The solution of the eq. (5.4) by the Monte Carlo method is given by (MELCHERS [5])

$$p_f = \int \cdots \int I[G(\mathbf{X}) \leq 0] f_{\mathbf{X}}(\mathbf{x}) d\mathbf{x} \tag{5.5}$$

$$\approx J_1 = \frac{1}{N} \sum_{j=1}^{N} I[G(\hat{\mathbf{x}}_j \leq 0)] \tag{5.6}$$

where $I[\ ]$ is the indicator function which equals 1 if the expression inside is true and zeroes otherwise, and N is the number of trials.

The next step is to estimate the number of simulations required for a given confidence level. Since the indicator function is a random variable with two possible outcomes, the central limit theorem establishes that eq. (5.6) approaches a normal distribution as $N \to \infty$ (MELCHERS [5]). The mean and variance of this distribution are defined by

$$\mu_{j_1} = \sum_{i=1}^{N} \frac{1}{N} E[(G \leq 0)] \tag{5.7}$$

$$\sigma_{j_1}^2 = \sum_{i=1}^{N} \frac{1}{N^2} \text{var}[(G \leq 0)] = \frac{\sigma_{I(G\leq 0)}^2}{N} \tag{5.8}$$

To calculate the confidence levels an estimate of the standard deviation of the indicator function is required. The indicator function variance is given by:

$$\text{var}[I(G \leq 0)] = \int \cdots \int I[(G \leq 0)]^2 d\mathbf{x} - \mu_{j_1}^2 \tag{5.9}$$

and therefore the sample variance is given by:

$$S_{I(G\leq 0)}^2 = \frac{1}{N-1} \left(\left\{ \sum_{j=1}^{N} I^2[G(\hat{x}_j) \leq 0] \right\} - N \left\{ \frac{1}{N} \sum_{j=1}^{N} I[G(\hat{x}_j) \leq 0] \right\}^2 \right) \tag{5.10}$$

To evaluate the confidence level for the distribution J_1 the central limit theorem is applied to the failure which occurs when:

$$P(-k\sigma_{j_1} < J_1 - \mu_{j_1} < +k\sigma_{j_1}) = C \tag{5.11}$$

where C is the confidence level. The approximation of standard deviation and mean value by binomial parameters, for instance, $\sigma_{j_1} = \{ N(1-p)p\}^{1/2}$ and $\mu_{j_1} = Np$, and if the error between the actual value of J_1 and the observer is defined by $\varepsilon = (J_1 - Np)/Np$, yields

$$\varepsilon = k[(1-p)/Np]^{1/2} \tag{5.12}$$

For a failure probability of 10^{-3} to achieve an error ε less than 20% with a confidence level of 95% (k=1.96) are necessary $N = 10^5$ samples.

Another way to estimate the number of samples to provide a reasonable estimation of a rare event is by the coefficient of variation C_v defined as (MARELLI *et al.* [7])

$$C_v = \frac{\sigma_{j1}}{\mu_{j1}} = \sqrt{\frac{1-p_f}{Np_f}} \tag{5.13}$$

To achieve a failure probability of 10^{-3} with 10% accuracy, $N = 10^5$ samples are needed. Therefore, rare event estimation is too expensive in computational terms.

5.2 First-order reliability method

This section will introduce the techniques developed to carry out a reliability analysis. To understand the method, the first-order reliability method (FORM) will be discussed in advance.

FORM is a tool often useful to estimate the probability of failure of rare events. Let D represents the failure subset domain, $\mathbf{x} = [x_1, \ldots, x_n]^T$ the random variables, $f(\mathbf{x})$ the joint probability density function of $\mathbf{x}$, therefore the probability of failure is given by:

$$p_f = \int_D f(\mathbf{x}) d\mathbf{x} \tag{5.14}$$

The FORM like other computational reliability methods uses the unique properties of the standard normal space. Hence, this methods involves a transformation of the random variables $\mathbf{x}$ into standard normal variables $\mathbf{u}$ (NIKOLAIDIS *et al.* [6]).

The reasons for this probability transformation are the useful properties of the standard normal space. For instance, the probability density in that space is rotationally symmetric about the origin which coincides with the mean point and decays exponentially with the square of the distance from this point. This property suggests that an approximation of the eq. (5.14) is to recast the integral with another boundary that has a close fit to the nearest point to the origin(KIUREGHIAN and KE [20]). This is the main idea of the first order reliability method.

5.2.1 Transformation to standard normal space

The transformation to standard normal space exists as long as the joint cumulative distribution function of the vector $\mathbf{x}$ of random variables is continuous and strictly increasing in each argument. This transformation is such that $\mathbf{u} = T(\mathbf{x})$ mapping the original random variables to a vector of standard normal variables.

Let the random variables $\mathbf{x}$ be statistically independent, i.e $f(\mathbf{x}) = f_1(x_1)f_2(x_2)...f_n(x_n)$ which each function on the right side defines the marginal probability density function for i^{th} random variable. In this case the needed transformation is diagonal and has the form

$$u_i = \Phi^{-1}[F_i(x_i)] \qquad i = 1, 2, ..., n \tag{5.15}$$

where Φ denotes the standard normal CDF. Figure 5.3 shows the transformation which has the same cumulative distribution function for both $\mathbf{x}$ and $\mathbf{u}$ random variables. The transformation is not unique since the replacement of $F_i(x_i)$ for $1 - F_i(x_i)$ is a solution as well.

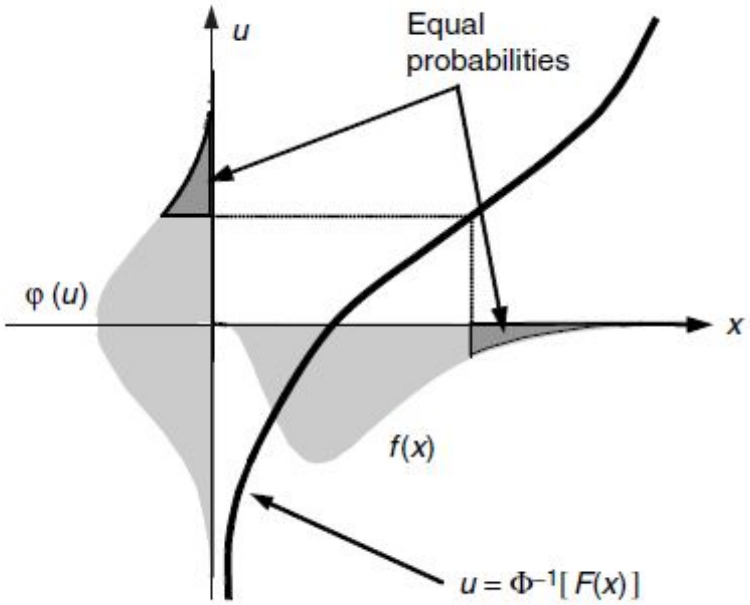

Figure 5.3: Transformation to the standard normal space for a single random variable NIKOLAIDIS *et al.* [6]

The inverse of the presented transformation is

$$x_i = F_i^{-1}[\Phi(u_i)] \qquad i = 1, 2, ..., n \tag{5.16}$$

For non-normal random variables in the original space the transformation is nonlinear, and an algorithm is required which is given by

$$f(\mathbf{u}) = \sum_{i=1}^{n} \frac{f_i(x_i)}{|\mathbf{J}|} \tag{5.17}$$

where the jacobian $\mathbf{J}$ may be deducted with regards to $\Phi^{-1}[F_i(x_i)] = T$ which the derivative to x_i gives

$$\frac{\partial T}{\partial x_i} = \frac{f_i(x_i)}{\phi\{\Phi^{-1}[F(x_i)]\}} = \frac{f_i(x_i)}{\phi(u_i)} \tag{5.18}$$

and hence, the Jacobian elements are defined by

$$J_{ii} = \frac{f_i(x_i)}{\phi(u_i)} \qquad i = 1, 2, ..., n \tag{5.19}$$

where $\phi(u_i) = (2\pi)^{-1/2} \exp(-u_i^2/2)$ is the univariate standard normal PDF.

Statistically dependent random variables

In case the n-vector of random variables $\mathbf{x}$ are non normally distributed and statistically dependent is usually carried out two transformations methods.

1. Nataf transformation

2. Rosenblatt transformation

The first transformation introduced is known as Nataf distribution which means that whenever dependent random variables $\mathbf{x}$ with prescribed CDF's $F_i(x_i)$ and correlation coefficients $\rho_{ij}, i, j = 1, ..., n$ are available a transformation to random variables $\mathbf{u}$ which is a joint Normal distribution is possible (MELCHERS [5]). The transformation is given by

$$u_i = \Phi_i^{-1}[F_{x_i}(x_i)] \qquad i = 1, ..., n \tag{5.20}$$

The random variables $\mathbf{u}$ has the probability density function $\phi_n(\mathbf{u}, \mathbf{P'})$ with zero means and unit standard deviations and correlation matrix $\mathbf{P'} = [\rho'_{ij}]$. Thus, the Nataf approximation is given by

$$f_x(\mathbf{x}) = \phi_n(\mathbf{u}, \mathbf{P'}).|\mathbf{J}| \tag{5.21}$$

where the jacobian is defined by

$$|\mathbf{J}| = \frac{\partial(u_1, \ldots, u_n)}{\partial x_1, ..., x_n} = \frac{f(x_1).f(x_2)\ldots f(x_n)}{\phi(u_1)\phi(u_2)...\phi(u_n)} \tag{5.22}$$

To fulfill the transformation the correlation matrix $\mathbf{P'}$ needs to be found. For convenience is introduced the normalized random variables $z_i = (x_i - \mu_{x_i})/(\sigma_{x_i})$ which provides the definition of the correlation matrix by

$$\rho_{ij} = \frac{\text{cov}[x_i x_j]}{\sigma_{x_i}\sigma_{x_j}} = E[z_i z_j] = \int_{-\infty}^{\infty}\int_{-\infty}^{\infty} z_i z_j \phi_2\big(u_i, u_j; \rho_{ij}^{'}\big) du_i du_j \tag{5.23}$$

where cov[ ] is the covariance of two random variables.

The expression above determines the correlation matrix $\mathbf{P'} = \{\rho'_{ij}\}$ through an iterative process and hence, the transformation to the normal standard space is established.

The second transformation presented is a Rosenblatt transformation. The transformation discussed in ROSENBLATT [21] is applicable to an absolutely continuous n-variate distribution $F(x_1, \ldots, x_n)$ and transformed into the uniform distribution $\mathbf{r}$ on the n-dimensional hypercube.

Since the standardized normal random variables $\mathbf{u}$ is the vector used in reliability methods the vector $\mathbf{r}$ is considered intermediary with regards to the original vector $\mathbf{x}$ (MELCHERS [5]). The Rosenblatt transformation in n-dimensional space is then:

$$\begin{aligned}
\Phi(u_1) &= r_1 = F_1(x_1) \\
\Phi(u_2) &= r_2 = F_2(x_2|x_1) \\
&\vdots \\
\Phi(u_n) &= r_n = F_n(x_n|x_1, \ldots, x_{n-1})
\end{aligned} \tag{5.24}$$

where Φ is the standard Normal cumulative distribution function and $F_i(x_i|x_1, ..., x_{i-1})$ the conditional cumulative distribution function for the random variables as given by

$$F_i(x_i|x_1, ..., x_{i-1}) = \frac{\int_{-\infty}^{\infty} f_{\mathbf{x}_i}(x_1, \ldots, x_{i-1}, t)dt}{f_{\mathbf{x}_{i-1}}(x_1, \ldots, x_{i-1})} \tag{5.25}$$

Notice that $f_{\mathbf{x}_j}$ is the marginal probability density function defined by

$$f_{\mathbf{x}_j}(x_1, \ldots, x_j) = \int_{-\infty}^{+\infty} \cdots \int_{-\infty}^{+\infty} f_{\mathbf{x}}(x_1, \ldots, x_n)dx_{j+1}, \ldots, dx_n \tag{5.26}$$

Back to the Rosenblatt transformation, the vector $\mathbf{u}$ from random variables is finally defined as:

$$\begin{aligned}
u_1 &= \Phi^{-1}[F_1(x_1)] \\
u_2 &= \Phi^{-1}[F_1(x_2|x_1)] \\
&\vdots \\
u_n &= \Phi^{-1}[F_n(x_n|x_1, \ldots, x_{n-1})]
\end{aligned} \tag{5.27}$$

Similarly, the inverse transformation is given by:

$$\begin{aligned}
x_1 &= F_1^{-1}[\Phi(u_1)] \\
x_2 &= F_2^{-1}[\Phi(u_2)|x_1] \\
&\vdots \\
x_n &= F_n^{-1}[\Phi(u_n)|x_1, ..., x_{n-1}]
\end{aligned} \tag{5.28}$$

This routine is generally done numerically.

Another point concerns the limit state function $g(\mathbf{x})$. Since the first order reliability method evolves the transformation of the limit state function to the normal standardized space, the next steps will settle this transformation. Let $G(\mathbf{u})$ be the

limit state function in the standardized normal space, and hence the transformation is defined by

$$g(\mathbf{x}) = G(\mathbf{u})|\mathbf{J}| \tag{5.29}$$

Equation (5.27) and eq. (5.24) give the jacobian elements since, $J_{ij} = \partial u_i/\partial x_j$ and thus:

$$\frac{\partial u_i}{\partial x_j} = \frac{1}{\phi(u_i)} \frac{\partial F_i(x_i|x_1, \ldots, x_{i-1})}{\partial x_j} \tag{5.30}$$

5.2.2 Search for the FORM design point

The first-order reliability method (FORM) intends to solve the integral in eq. (5.14) by an approximation. The approximation is obtained from the linearization of the limit-state function in the standard normal space at a specific point and therefore, this function needs to be continuous and differentiable in the neighborhood of the optimal location.

Let $\mathbf{x}$ be the vector of random variable. Let $g(\mathbf{x})$ be the limit state function in the original space. Let $f(\mathbf{x})$ be the joint PDF of $\mathbf{x}$. Let $G(\mathbf{u}) \equiv g(T^{-1}(\mathbf{u}))$ be the limit-state function in the standard normal space. Then, transforming the variables into the standard normal space the probability of failure is recast as:

$$p_f = \int_{g(\mathbf{x}\leq 0)} f(\mathbf{x}) d\mathbf{x} = \int_{G(\mathbf{u}\leq 0)} \phi_n(\mathbf{u}) d\mathbf{u} \tag{5.31}$$

The optimal point chosen to linearize the limit state function in the standard normal space is the point closer to the origin which concentrates the higher density probability as explained in section section 5.2.1. This point is known as the design point or most probable point (MPP) (MELCHERS [5]). Therefore, the constrained optimization problem is defined by

$$\mathbf{u}^* = \min\{\|\mathbf{u}\| \big| G(\mathbf{u}) = 0\} \tag{5.32}$$

The norm of $\mathbf{u}^*$ was defined before as the safety index β or β_{HL} and thus the probability of failure yields

$$p_f = \Phi(-\beta_{HL}) \tag{5.33}$$

The FORM algorithm, in summary, approximates the limit-state function in the standard normal space as the hyperplane tangent to the limit-state function at the design point (HASOFER and LIND [22]) as shown in fig. 5.4.

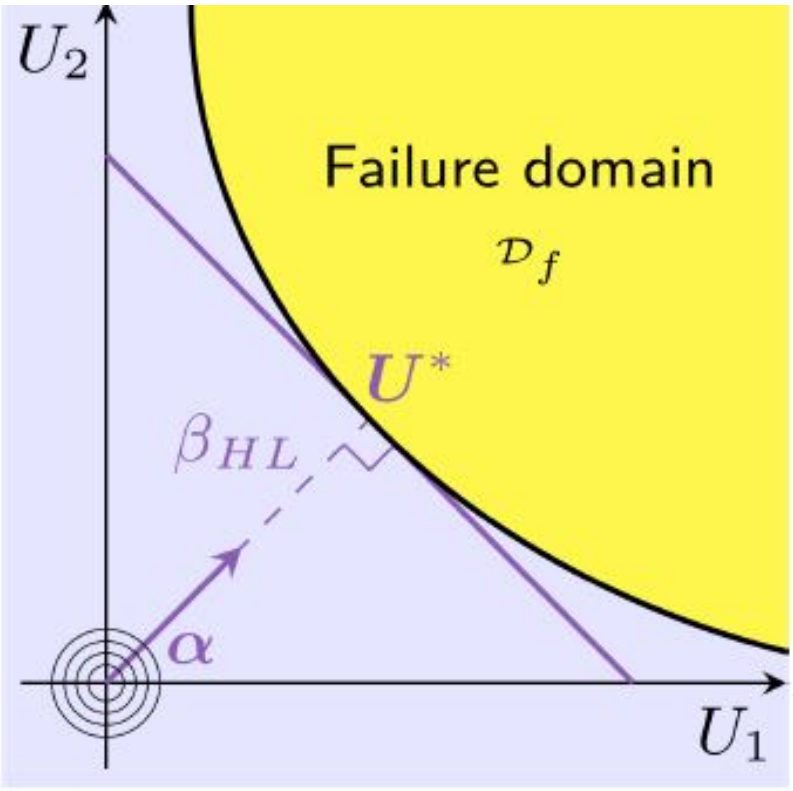

Figure 5.4: FORM linearization hyperplane for estimation of the probability of failure MARELLI *et al.* [7]

For the non-linear case, the optimization problem uses the Lagrangian multipliers as:

$$\mathcal{L}(\mathbf{u}, \lambda) = \frac{1}{2}\|\mathbf{u}\|^2 + \lambda G(\mathbf{u}) \tag{5.34}$$

where λ is the Lagrange multiplier, and the related conditions are:

$$\nabla_{\mathbf{u}}\mathcal{L}(\mathbf{u}^*, \lambda^*) = 0 \tag{5.35}$$

$$\frac{\partial \mathcal{L}}{\partial \lambda}(\mathbf{u}^*, \lambda^*) = 0 \tag{5.36}$$

The equations above may be recast as:

$$G(\mathbf{u}^*) = 0 \tag{5.37}$$

$$\mathbf{u}^* + \lambda^* \nabla G(\mathbf{u}^*) = 0 \tag{5.38}$$

This pair of equations address that the design point belongs to the limit-state surface and the vector $\mathbf{u}^*$ is collinear to $\nabla G(\mathbf{u}^*)$.

Hasofer-Lind - Rackwitz-Fiessler algorithm (HL-RF)

The search for the design point which is the solution of eq. (5.37) and eq. (5.38) may be an iterative process presented by RACKWITZ and FIESSLER [23]. The first step is to input a value for $\mathbf{u}$ which commonly is the origin. At each iteration, the limit-state function is approximated as:

$$G(\mathbf{u}) \approx G(\mathbf{u}_k) + \nabla G(\mathbf{u}_k)\dot{(}\mathbf{u} - \mathbf{u}_k) \tag{5.39}$$

After some algebra and the introduction of the unit vector α eq. (5.37) and eq. (5.38) are reduced to:

$$\mathbf{u}_{k+1} = \left[\alpha_k.\mathbf{u}_k + \frac{G(\mathbf{u}_k)}{\|\nabla G(\mathbf{u}_k)\|}\right]\alpha_k \tag{5.40}$$

$$\alpha_k = -\frac{\nabla G\mathbf{u}_k}{\|\nabla G(\mathbf{u}_k)\|} \tag{5.41}$$

For each k-th iteration the reliability index is given by:

$$\beta_k = \alpha_k.\mathbf{u}_k + \frac{G(\mathbf{u}_k)}{\|\nabla G(\mathbf{u}_k)\|} \tag{5.42}$$

The safety index β equals $\alpha^*.\mathbf{u}^*$ when the algorithm converges, i.e, $G(\mathbf{u}^*)$ equals zero. The convergence criterion of the algorithm is commonly based on the safety index β or the stability of $\mathbf{u}$ or the difference of the limit-state surface between consecutive iterations.

Improved HL-RF algorithm (iHL-RF)

The algorithm developed by HASOFER and LIND [22] and RACKWITZ and FIESSLER [23] and LIU and DER KIUREGHIAN [24] despite being widely used has no proof of its convergence for any given problem. However, ZHANG and DER KIUREGHIAN [25] developed an improved version of this algorithm which is globally convergent for a differentiable limit state function $G(\mathbf{u})$ in the standard normal space.

The constrained optimization problem is defined as

$$\mathbf{u}^* = \min\{\|\mathbf{u}\| \big| G(\mathbf{u}) = 0\} \tag{5.43}$$

where the norm of $\mathbf{u}^*$ is the safety index β. The algorithm generates a sequence of points such as

$$\mathbf{u}_{k+1} = \mathbf{u}_k + \lambda_k \mathbf{d}_k \tag{5.44}$$

where λ_k denotes the step size, and d_i is the search direction vector. The global convergence of the algorithm is assured if a merit function attains its minimum at the solution point of the problem and $\mathbf{d}_k$ is a descent vector of the merit function at every point of the sequence in eq. (5.44). The Armijo rules in eq. (5.45) presents the merit function m and the best step length λ_k for each iteration.

$$\lambda_k = \max_s \{b^s \big| m(\mathbf{u}_k + b^s \mathbf{d}_k) - m(\mathbf{u}_k) \leq -ab^s \langle \nabla m(\mathbf{u}_k), \mathbf{d}_k \rangle\} \tag{5.45}$$

where $(a, b) \in (0, 1)$ are pre-selected parameters and s is an integer.

The solution of the problem eq. (5.43) is given by eq. (5.37) and eq. (5.38), and the HL-RF search direction comes from the solution of these equations for the linearized constraint

$$L_{\mathbf{u}_k}(\mathbf{u}) = G(\mathbf{u}_k) + \langle \nabla G(\mathbf{u}_k), \mathbf{u} - \mathbf{u}_k \rangle \tag{5.46}$$

where $L_{\mathbf{u}_k}(\mathbf{u})$ is the linearized limit state function at k-th step. Thus, the search direction is defined by

$$\mathbf{d}_k = \frac{\langle \mathbf{u}_k, \nabla G_{\mathbf{u}_k} \rangle - G(\mathbf{u}_k)}{\|\nabla G_{\mathbf{u}_k}\|^2} \nabla G_{\mathbf{u}_k} - \mathbf{u}_k \tag{5.47}$$

The simpler merit function which has its minimum at the solution of eq. (5.43) as wells as the same search descent direction $\mathbf{d}$ is given by

$$m(\mathbf{u}) = \frac{1}{2}\|\mathbf{u}\| + c\big|G(\mathbf{u})\big| \tag{5.48}$$

where $c > \frac{\|\mathbf{u}\|}{\|\nabla G(\mathbf{u})\|}$ is a real penalty parameter.

5.3 Importance Sampling

The importance sampling (IS) is another method to evaluate the integral

$$p_f = \int \cdots \int I[G(\mathbf{x}) \leq 0] f_{\mathbf{x}}(\mathbf{x}) dx \tag{5.49}$$

by the introduction of the importance-sampling probability function $h_{\mathbf{v}}(\mathbf{v})$ to a random vector $\mathbf{v}$ and hence, the integral eq. (5.49) is recast as ([5])

$$p_f = \int \cdots \int I[G(\mathbf{x}) \leq 0] \frac{f_x(\mathbf{x})}{h_{\mathbf{v}}(\mathbf{x})} h_{\mathbf{v}}(\mathbf{x}) dx \tag{5.50}$$

$$= E\left\{ I\big[G(\mathbf{v}) \leq 0\big] \frac{f_{\mathbf{v}}(\mathbf{v})}{h_{\mathbf{v}}(\mathbf{v})} \right\} \tag{5.51}$$

where $E\{\ \}$ denotes the expected value and $\mathbf{v}$ a random vector with probability function $h_{\mathbf{v}}(\mathbf{v})$. The probability of failure may be also estimated by

$$p_f \approx \frac{1}{N}\sum_{j=1}^{N}\left\{ I[G(\mathbf{v}_j) \leq 0]\frac{f_{\mathbf{x}}(\mathbf{v}_j)}{h_{\mathbf{v}}(\mathbf{v}_j)} \right\} \tag{5.52}$$

The sampling distribution $h_{\mathbf{v}}(\ )$ may be chosen to reduce the variance of the probability of failure given by

$$\begin{aligned} \mathrm{var}\left\{ I\big[G(\mathbf{x}) \leq 0\big]\frac{f_{\mathbf{x}}(\mathbf{x})}{h_{\mathbf{v}}(\mathbf{x})} \right\} = \int\cdots\int \left\{ I\big[G(\mathbf{x}) \leq 0\big]\frac{f_{\mathbf{x}}(\mathbf{x})}{h_{\mathbf{v}}(\mathbf{x})} \right\}^2 h_{\mathbf{v}}(\mathbf{x})d\mathbf{x} \\ -E\left\{ I\big[G(\mathbf{x}) \leq 0\big]\frac{f_{\mathbf{x}}(\mathbf{x})}{h_{\mathbf{v}}(\mathbf{x})} \right\}^2 \end{aligned} \tag{5.53}$$

If the sampling distributing function is selected as

$$h_{\mathbf{v}}(\mathbf{v}) = \frac{\big|I[\quad]f_{\mathbf{x}}(\mathbf{v})\big|}{\int\cdots\int\big|I[\quad]f_{\mathbf{x}}(\mathbf{v})\big|d\mathbf{v}} \tag{5.54}$$

the variance in eq. (5.54) equals zero and therefore describes the optimal distribution. However, this distribution is not helpful since the probability of failure is needed.

In general, reliability problems are interested in the hyperzone $G(\mathbf{x}) \leq 0$ and, mainly, the region of greatest probability density within that zone. In the original space, this is the region to the right of the design point x^* and therefore the first order reliability method which applies an algorithm to search for the design point is helpful. Once the design point is identified an approach for choosing the importance sampling distribution $h_{\mathbf{v}}(\ )$ is a normal standard distribution with its mean on the design point as shown by fig. 5.5.

This sampling distribution has approximately equal probability in falling in either the safe or the unsafe region, i.e., for a given level of confidence far fewer sample points are required to converge the likelihood of failure in comparison with the crude Monte Carlo method. For instance, consider that 100 points in the failure region are needed. The assumption that the "success" rate for the sampling distribution is around 50% requires 200 samples. On the other hand, by the Crude Monte Carlo method for a rare event probability of 10^{-4} which is rather typical for these applications, requires an amount of 100 points $\times$ 10^4, i.e, 10^6 samples. Therefore, importance sampling has much better efficiency than the crude Monte Carlo method and is not an approximation as FORM .

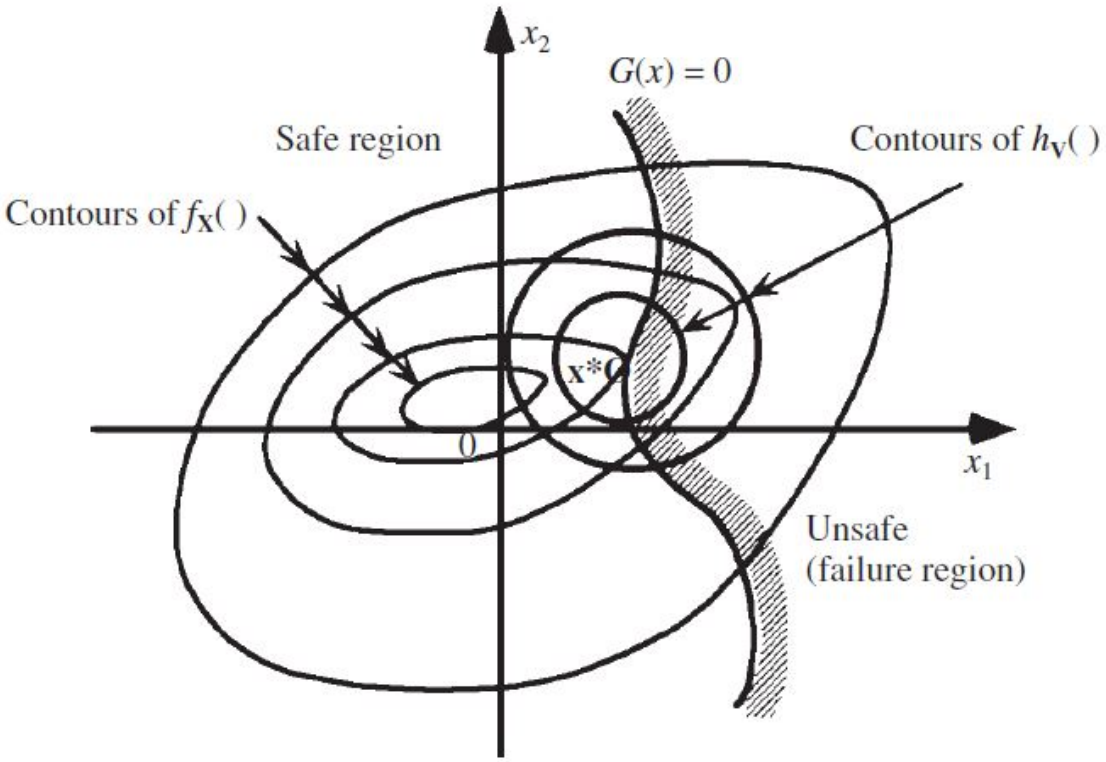

Figure 5.5: Importance sampling function $h_{\mathbf{v}}(\ )$ in the original space MELCHERS [5]

5.4 Reliability methods drawbacks and advantages

The first-order reliability method has the advantage to estimate the probabability of failure in the standardized normal space which only requires the design point to be found. However, when the limit-state function is not linear there is no guarantee the search for the design point will converge or if the limit-state function has multiple mininum local the probability of failure will not represent an accurate estimative. In such cases the Importance Sampling represents a better solution because the design point does not need to be accurate to converge for the probability of failure. However it does need to compute a few more samples than FORM .

5.5 Implicit functions

Sometimes the limit state function might not be known explicitly by the vector $\mathbf{x}$ which represents the random variables in the original space. For instance, the limit state may be represented at discrete points through a finite element analysis. Since the limit state function may not be written with respect to the random variables, the general procedure to search for the design point in a FORM analysis is not

applicable (MELCHERS [5]).

This section presents the direct coupling, response surface method, and the polynomials chaos expansion to deal with implicit limit-state functions. The last has been chosen due to the efficiency, flexibility and availability on UQLab software.

5.5.1 Direct coupling method

KIUREGHIAN and KE [20] reviews that the algorithm which searches the design point in the standard normal space u^* uses the gradient vector of the limit-state function,

$$\nabla_{\mathbf{u}} G(\mathbf{u}) = \left[\frac{\partial G(\mathbf{u})}{\partial u_1} \dots \frac{\partial G(\mathbf{u})}{\partial u_2} \right] \tag{5.55}$$

and therefore an intermediate vector of random variables $\mathbf{s}$ which is explicit in the limit-state function, and the input vector $\mathbf{x}$ gives the chain rule of differentiation

$$\nabla_{\mathbf{u}} G(\mathbf{u}) = \nabla_{\mathbf{s}} g(\mathbf{s}) J_{\mathbf{s},\mathbf{x}} J_{\mathbf{x},\mathbf{u}} \tag{5.56}$$

where $\nabla_{\mathbf{s}} g(\mathbf{s})$ is the gradient of the limit-state function with respect to $\mathbf{s}$, $J_{\mathbf{s},\mathbf{x}}$ is the Jacobian of the transformation from $\mathbf{s}$ to $\mathbf{x}$ and $J_{\mathbf{x},\mathbf{u}}$ is the Jacobian of the transformation from $\mathbf{x}$ to $\mathbf{u}$. The difficulty in the algorithm lies in computing the Jacobians like $J_{\mathbf{s},\mathbf{x}}$, the partial derivatives of the output variables with respect to the input variables. This is known as the direct differentiation method which applies to non-linear and time-variant problems as well (SUDRET and KIUREGHIAN [26]).

SUDRET and KIUREGHIAN [27] wrote a report which substitutes the term $J_{\mathbf{s},\mathbf{x}}$ for $\nabla_{\mathbf{x}} S(\mathbf{x})$. For structural reliability with finite element analysis, the last term denotes the mechanical transformation whose evaluation is the main point to carry out a reliability analysis.

To determine the design point either a straightforward application of a finite difference scheme or the perturbation method are possible as well. However, the first method for a vector of n random variables requires $n+1$ complete finite element analysis for each gradient, and the accuracy depends on the size of finite variation of the parameters which is difficult to handle in advance. Therefore, the perturbation method is a more efficient approach and is known as well as the direct differentiation method. SUDRET and KIUREGHIAN [27] investigates this method for a static elastic case, geometrically non-linear structures, dynamic response sensitivity of elastoplastic structures and plane stress plasticity and damage.

The direct coupling has the main drawback which is the necessity of an analytical development of the gradients in the chain rule of differentiation for each addressed problem.

5.5.2 Response surface method

Another approach is to construct a surrogate limit state function which includes response surfaces, artificial neural networks, vector support machine techniques and gaussian processing modeling, also known as the Kriging technique (MELCHERS [5]).

A limit-state surface may be constructed artificially by a polynomial or other suitable function fitted to the results from numerical analyses. This surface is known as a response surface. An appropriate response surface should represent the response in a structural reliability analysis with most accuracy in the area around most probable point (MPP) .

Let the limit-state function be represented by $G(\mathbf{x})$ and let it be an implicit function of the vector of random variables $\mathbf{x}$. Let $\hat{\mathbf{x}}$ represent a discrete set of points in $\mathbf{x}$ space and let $G(\mathbf{x})$ be evaluated in these points. Thus, the response surface method is to fit a function $\bar{G}(\mathbf{x})$ with the discrete set of values $G(\bar{\mathbf{x}})$. The typical approach to the response surface is to let $\bar{G}(\mathbf{x})$ be a n-th order polynomial and its coefficients determined to minimize the error of the approximation.

A polynomial regression model applicable for the surrogate limit-state function may be (MELCHERS [5])

$$\bar{G}(\mathbf{x}) = \mathbf{A} + \mathbf{x}^T\mathbf{B} + \mathbf{x}^T\mathbf{C}\mathbf{x} \tag{5.57}$$

with undetermined (regression) coefficients defined by $\mathbf{A}$, $\mathbf{B}^T = [B_1, B_2, \ldots, B_n]$ and

$$\mathbf{C} = \begin{bmatrix} C_{11} & \ldots & C_{1n} \\ \vdots & & \vdots \\ sym & \ldots & C_{nn} \end{bmatrix} \tag{5.58}$$

The least-square-fit method finds the response surface coefficients. Let the vector D represent the set of regression coefficients $\mathbf{A}$, $\mathbf{B}$ and $\mathbf{C}$. Let $\bar{G}(\mathbf{D}, \mathbf{x})$ represent the eq. (5.57). Let ε_i represent the error between the implicit limit state function $G(\bar{x}_i)$ and the approximation response surface $\bar{G}(\mathbf{D}, \mathbf{x})$ for each point $\bar{\mathbf{x}}_i$. Thus, $\mathbf{D}$ is selected to minimize the sum of squares of the errors:

$$S = \min_{\mathbf{D}} \left[\sum_{i=1}^{n} \varepsilon_i \right]^{1/2} = \min_{\mathbf{D}} \left[\sum_{i=1}^{n} \left(\bar{G}\big(\mathbf{D}, \bar{x}_i\big) - G\big(\bar{x}_i\big) \right)^2 \right]^{1/2} \tag{5.59}$$

The above procedure is also known as polynomial regression and is one of the many to fit a response surface instead of the original implicit limit-state function.

The response surface method may also be addressed by a polynomial function in a quadratic form (SUDRET and KIUREGHIAN [27]) such as:

$$G(\mathbf{x}) \approx \bar{G}(\mathbf{x}) = a_0 + \sum_{i=1}^{N} a_i x_i + \sum_{i=1}^{N} a_{ii} x_i^2 + \sum_{i=1}^{N} \sum_{j=1, j\neq i}^{N} a_{ij} x_i x_j \tag{5.60}$$

where the set of coefficients $\mathbf{a} = \{a_0, a_i, a_{ii}, a_{ij}\}^3$ needs to be determined.

The unknown coefficients are estimated by the least-square method. Thus, the error between the fitted limit-state function and the implicit limit-state function for each selected point is

$$\varepsilon(\mathbf{a}) = \sum_{i=1}^{N} \Big(G(\bar{x}_i) - \bar{G}(\bar{x}_i) \Big)^2 \tag{5.61}$$

Equation (5.60) can be recast as

$$\bar{G}(\mathbf{x}) = \{1, x_i, x_i^2, x_i x_j\}^T \cdot \{a_0, a_i, a_{ii}, a_{ij}\} \equiv \mathbf{V}^T(\bar{\mathbf{x}}) \cdot \mathbf{a} \tag{5.62}$$

where $\bar{\mathbf{x}}$ is the set of fitting points.

Hence, the least-square problem becomes:

$$\mathbf{a} = \min \left[\sum_{i=1}^{n} \Big(G(\bar{x}_i) - \mathbf{v}^T(\bar{x}_i) \cdot \mathbf{a} \Big)^2 \right] \tag{5.63}$$

The solution of eq. (5.63) turns out to be:

$$\mathbf{a} = \big(\mathbf{V}^T \cdot \mathbf{V} \big)^{-1} \cdot \mathbf{V}^T \cdot G(\bar{\mathbf{x}}) \tag{5.64}$$

where $\mathbf{V}$ is the matrix whose rows are the vectors $\mathbf{v}^T(\bar{x}_i)$. Note that the fitting points have to be appropriately selected to get an invertible matrix $\mathbf{V}^T \cdot \mathbf{V}$.

5.5.3 Polynomial chaos expansion

Polynomials chaos expansion (PCE) is a powerful technique to provide a functional approximation of computational models through its spectral representation on a basis of polynomial expansion (MARELLI and SUDRET [28]).

Let a random vector $\mathbf{x}$ with M independent variables. Let $f_{\mathbf{x}}(\mathbf{x})$ be the joint probability density function of $\mathbf{x}$. Let a finite variance computational models as a map $\mathbf{y} = \mathscr{M}(\mathbf{x})$. Then, the polynomial chaos expansion of $\mathscr{M}(\mathbf{x})$ is defined as:

$$\mathbf{y} = \mathscr{M}(\mathbf{x}) = \sum_{\alpha} y_\alpha \Psi_\alpha(\mathbf{x}) \tag{5.65}$$

where Ψ_α are multivariate polynomials orthonormal with respect to $f_{\mathbf{x}}(\mathbf{x})$, $\alpha \in \mathbb{N}^M$ is a multi-index which identifies the components of the polynomials Ψ_α and y_α the corresponding coefficients. The sum in eq. (5.65) needs to be truncated for

realistic applications and hence, the multi-index α is restricted to a subset $\mathscr{A} \subset \mathbb{N}^M$ of selected multi-indices of multivariate polynomials.

The polynomial basis is built from a set of univariate orthonormal polynomials $\phi_k^{(i)}(x_i)$ which satisfy:

$$\left\langle \phi_j^{(i)}(x_i), \phi_k^{(i)}(x_i) \right\rangle \stackrel{\text{def}}{=} \int_{D_{x_i}} \phi_j^{(i)}(x_i)\phi_k^{(i)}(x_i) f_{\mathbf{x_i}}(x_i) dx_i = \delta_{jk} \tag{5.66}$$

where i denotes the input variable, j and k the corresponding polynomial degree and δ_{jk} the Kronecker symbol.

Thus, the multivariate polynomials $\Psi_\alpha(\mathbf{x})$ are formed by the tensor products of their univariate counterparts:

$$\Psi_\alpha(\mathbf{x}) \stackrel{\text{def}}{=} \prod_{i=1}^{M} \phi_{\alpha_i}^{(i)}(x_i) \tag{5.67}$$

Therefore the multivariate polynomials are orthonormal as well.

A truncation scheme to the univariate polynomials may be defined as all polynomials in the M input variables of total degree less than or equal to p:

$$\mathscr{A}^{M,p} = \{\alpha \in \mathbb{N}^M \quad : |\alpha| \leq p\} \qquad \text{card } \mathscr{A}^{M,p} \equiv P = \binom{M+p}{p} \tag{5.68}$$

The calculation of the coefficients y_α of the polynomial chaos expansion for a given basis are implemented by a non-intrusive method which considers a proper sampling of the random input variables.

The least-square minimization is an approach one may estimate the coefficients. The eq. (5.65) can be recast as:

$$\mathbf{y} = \mathscr{M}(\mathbf{x}) = \sum_{j=0}^{P-1} y_j \Psi_j(\mathbf{x}) + \varepsilon_P \equiv \mathbf{y}^T \Psi(\mathbf{x}) + \varepsilon_P \tag{5.69}$$

where P was defined as the cardinality of the set $A^{M,p}$, ε_p is the truncation error, y is a vector containing the coefficients and $\Psi(\mathbf{x})$ is the matrix containing the values of all the orthonormal polynomials in $\mathbf{x}$.

Thus, the least-square problem is set up as:

$$\hat{\mathbf{y}} = \min \left[\left(\mathbf{y}^T \Psi(\mathbf{x}) - \mathscr{M}(\mathbf{x}) \right)^2 \right] \tag{5.70}$$

The solution to the problem above is similar to eq. (5.63).

To estimate the error due to the truncation in polynomial chaos expansion one may determine by the leave-one-out cross-validation error ε_{LOO} . This method con-

sists in building N metamodels $\mathscr{M}^{PC\setminus i}$, each one created on a reduced experimental design $\bar{\mathbf{x}}\setminus\bar{x}_i = \{\bar{x}_j, j = 1,\ldots,N, j \neq i\}$ and comparing its prediction on the excluded point $\bar{x}_i$ with the real value y_i. The leave-one-out cross-validation error is then:

$$\varepsilon_{LOO} = \frac{\sum_{i=1}^{N}\left(\mathscr{M}(\bar{x}_i) - \mathscr{M}^{PC\setminus i}(\bar{x}_i)\right)}{\sum_{i=1}^{N}\left(\mathscr{M}(\bar{x}_i) - \mu_{\mathbf{y}}\right)} \tag{5.71}$$

where $\mu_{\mathbf{y}}$ is the mean value of the vector of the real values $\mathbf{y}$ and $\mathscr{M}^{PC}$ is the truncated polynomial chaos expansion.

Chapter 6

Rare event estimation results

Rare event estimation also known as reliability analysis plays an essential role in this chapter on evaluating the probability of failure of the stochastic rotordynamic model.

UQLab software will carry out the reliability analyses. UQLab is a general purpose Uncertainty Quantification framework developed at ETH Zurich (Switzerland). It is an open-source scientific with modules which are smoothly connected through UQLab to carry out uncertainty propagation. For instance, Monte Carlo sampling, sensitivity analysis, reliability analysis, build surrogate models.

The routine to execute the reliability analysis is to run the UQLab module of polynomial chaos expansion and build a surrogate model from the stochastic rotordynamic model with two uncertain parameters related to stiffness and damping coefficients. Then, from the surrogate model, the design point is searched through the first order reliability method included in UQlab package. Finally, the importance sampling is applied to a function around the design point, and the probability of failure is estimated. This routine instead of a Monte Carlos Simulation yields a more efficient approach to rare event simulations.

The analysis takes the vector $\mathbf{x}$ of random variables x_1 and x_2, where x_1 is the variable related to the bearing stiffness and x_2 to the damping. The input variable physically means how many times the random number multiplies the deterministic value in a uniform distribution. For example, $x_1 = 1.5$ represents a stiffness 50% higher than the deterministic value.

The rotordynamic stochastic model is divided into two limit-state functions which yield:

$$G_1(\mathbf{x}) = A_{\max}(\mathbf{x}) - A_{v_1} \tag{6.1}$$

$$G_2(\mathbf{x}) = SM_a(\mathbf{x}) - SM_r(\mathbf{x}) \tag{6.2}$$

where $A_{\max}$ means the maximum amplitude which occurs at minimum allowable speed N_{ma} , A_{v_1} the vibration limit within operational speed, SM_a the actual separation margin between operational speed and critical speed and SM_r the separation margin required between operational speed and critical speed. These variables are withdrawn from an unbalance response analysis. Due to the lack of failure probability on the second compressor, this chapter analysis is only for the first compressor.

6.1 Uncertain Stiffness

The analyzes follow the sequence presented in chapter 4. Therefore, the random variable is only applicable to the stiffness for the first case where the random variable is $f_{\mathbf{x}}(x_1) \sim \mathcal{U}(1, 1.45)$.

The polynomials chaos expansion (PCE) is used to find a surrogate model for the limit-state function $G_1(\mathbf{x})$. The results are shown in fig. 6.1.

The polynomial degree is chosen between 3 and 15 as a degree-adaptive calculation of the PCE coefficients which finds the degree with the lowest Leave-One-Out cross-validation error.

The model represents a 15 polynomial degree with a basis of 16 vectors after 500 model evaluations and presented a leave-one-out cross-validation error (ε_{LOO}) around 2.9×10^{-21}. The coefficients norms $|y_\alpha|$ are higher as lower are the degrees such that its mean value is close to the first degree.

Once the surrogate model is built the FORM analysis is the next step. Figure 6.2 shows the convergence of the method for the safety index β_{HL} which reached 0.1747 after 100 iterations and 800 model evaluations. The approximated probability of failure is then, 56.94%. Figure 6.3 shows the design point $(-0.1745\ 0)$ with a green triangle marker in the standardized normal space which corresponds to $(1.1938, 1)$ in the original space.

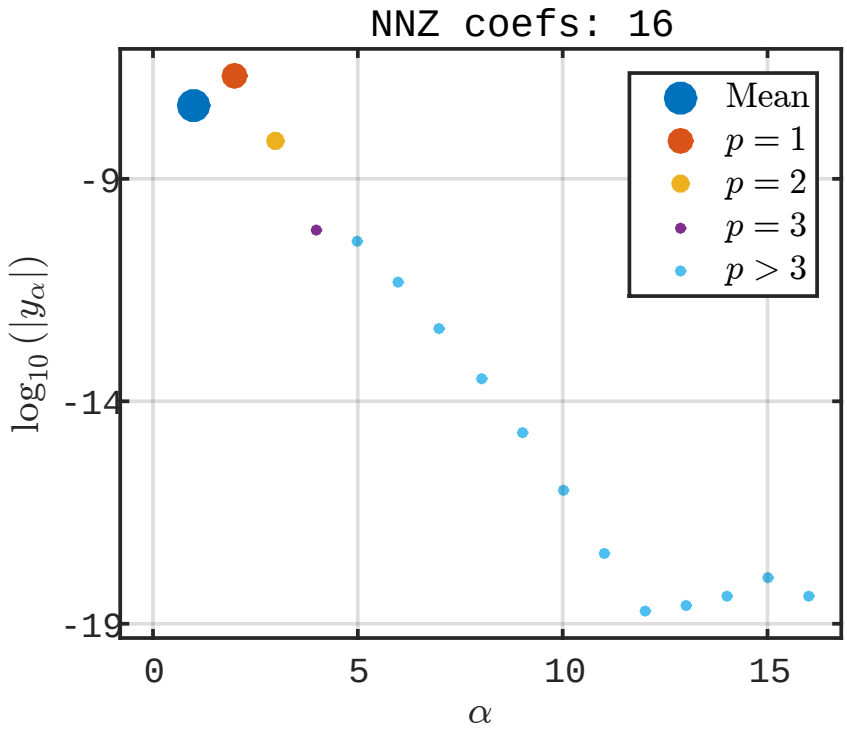

Figure 6.1: Graphical representation of the logarithmic spectrum of the PCE coefficients.

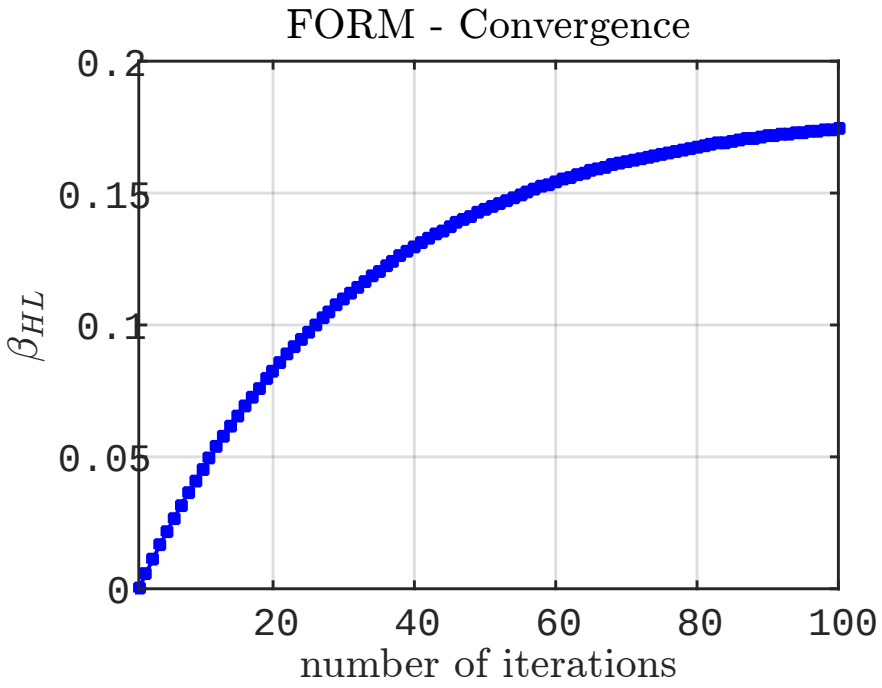

Figure 6.2: FORM analysis convergence.

Note that the samples vary only along the abscissa values since the damping which corresponds to the ordinate is a deterministic value for this analysis.

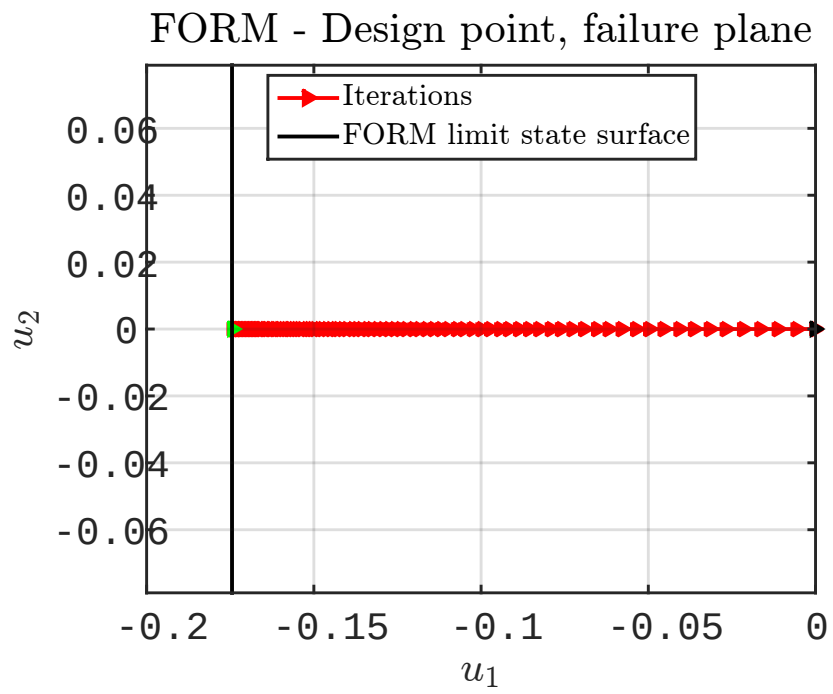

Figure 6.3: Form design point and failure plane

The importance sampling (IS) is carried out after the FORM since the design point is one of its inputs. The convergence is presented in fig. 6.4 along with the confidence level which is set as 0.05 and therefore by *eq.* (5.11) gives an interval of failure probability around (53.8 60.9)% with a coefficient of variation (C_v) of 0.0316. The probability of failure by importance sampling is 57.3%. Notice in this case that FORM gives a lower probability of failure than importance Sampling and instead within the confidence bounds of the second method. The whole procedure lasted around 4 hours and 30 minutes.

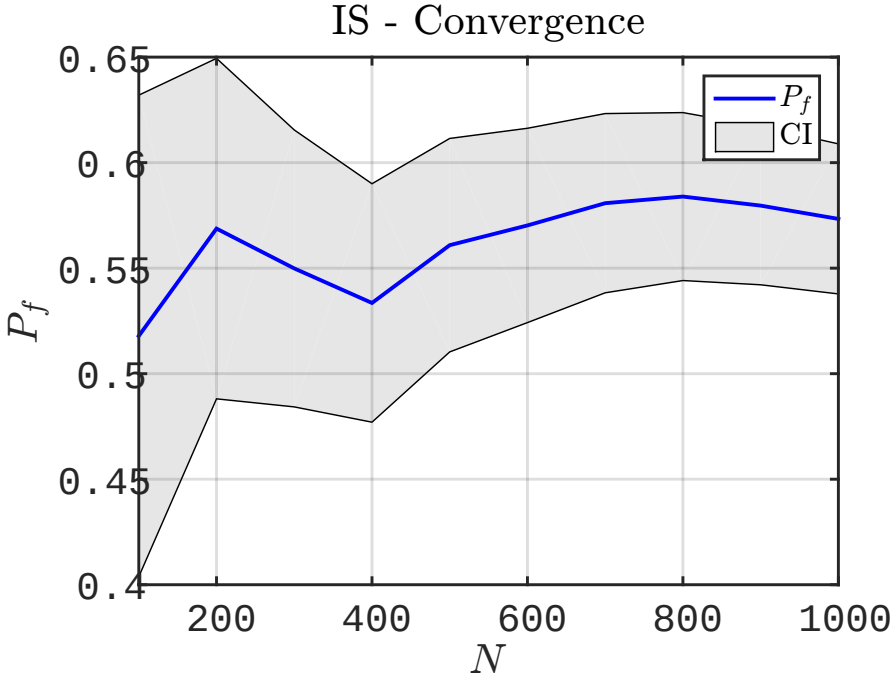

Figure 6.4: Importance sampling convergence.

Figure 6.5 shows the sampling distribution in the standardized space with the green and red points which mark the safe and failure zone, respectively. The safety index is estimated to be 0.1849.

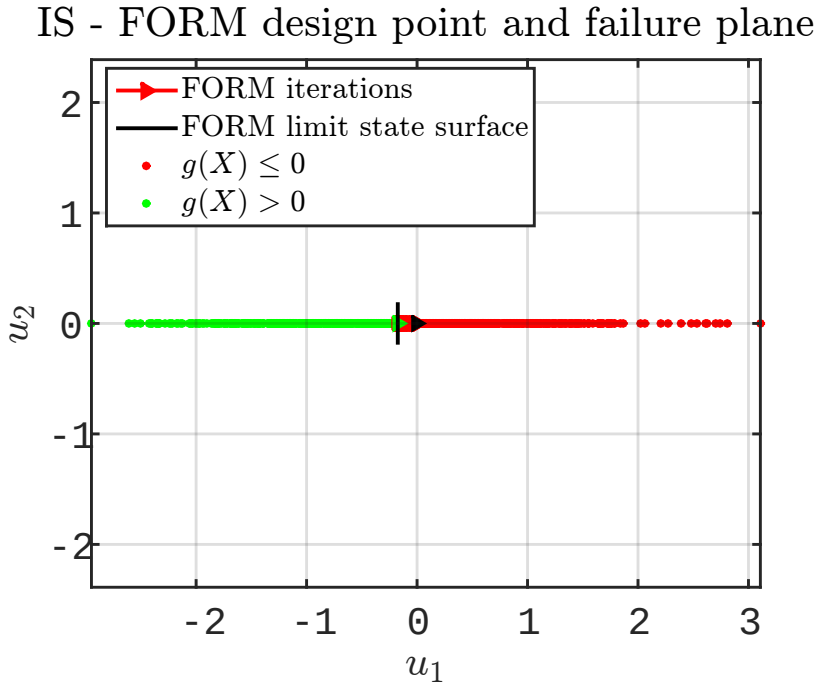

Figure 6.5: IS samples and FORM failure plane.

6.2 Uncertain damping

The last section was an uncertain stiffness variable whereas this section will be carried out only for uncertain damping where distribution is given by $f_{\mathbf{x}}(x_2) \sim \mathcal{U}(1, 1.82)$. The PCE carried out lead to a total of 16 vectors to the basis and a 15 polynomial degree with an error ε_{LOO} of 1.19×10^{-21}. Figure 6.6 shows that the basis with higher coefficients are the ones with lower degrees.

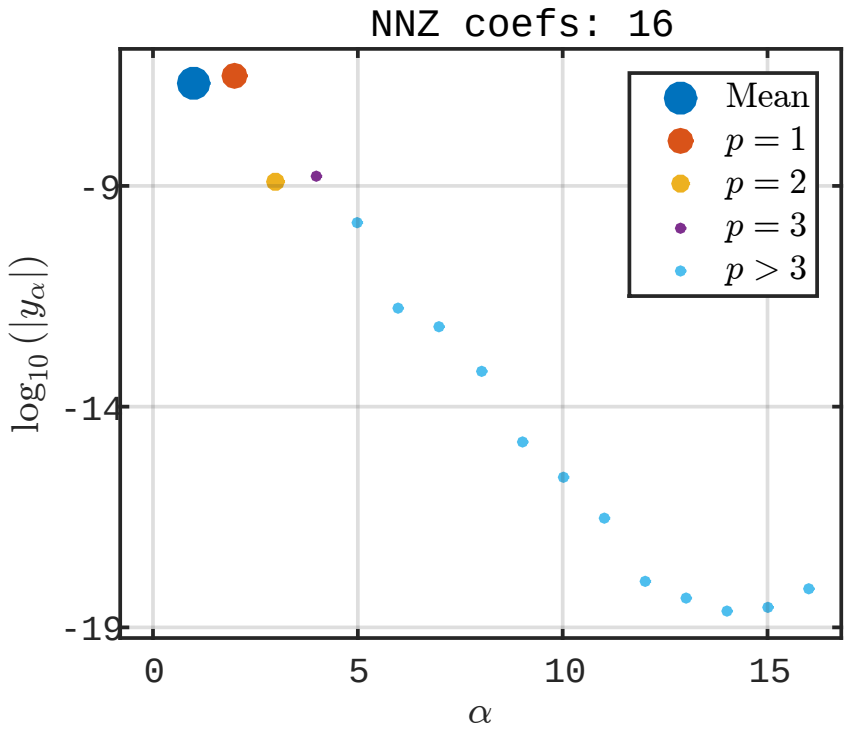

Figure 6.6: Graphical representation of the logarithmic spectrum of the PCE coefficients.

Figure 6.7 shows the convergence to FORM analysis with regards to the safety index β_{HL}. After 100 iterations and 800 model evaluations, the safety index converged to 0.4801.

Figure 6.8 shows the design point in the standardized normal space as (0 $-$ 0.4794) which corresponds to (1 1.2590) in the original space. Notice that the limit-state surface is horizontal according to a deterministic stiffness value, i.e., u_1. Hence, the probability of failure by FORM is 68.44%.

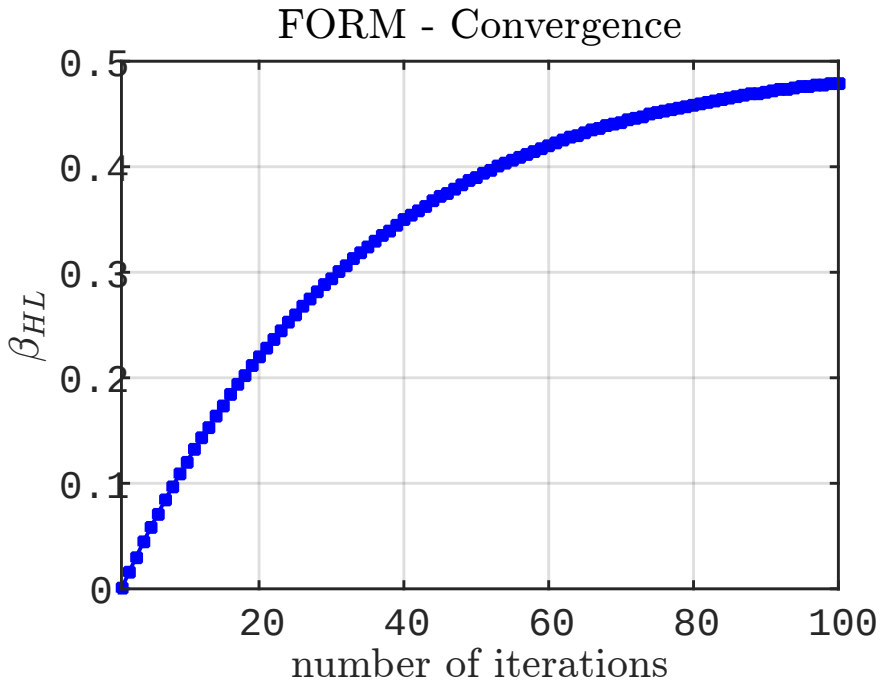

Figure 6.7: FORM analysis convergence.

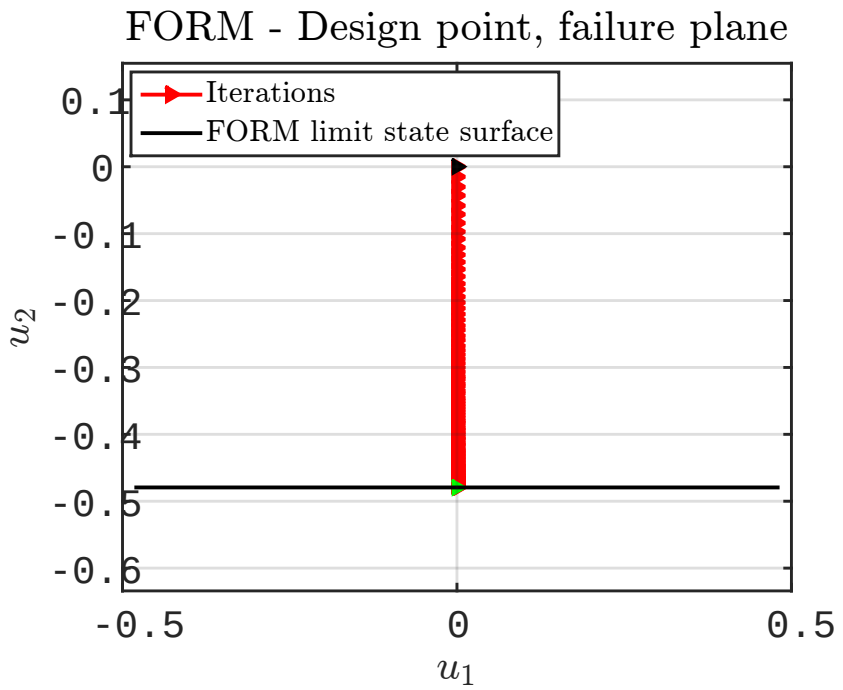

Figure 6.8: FORM design point and failure plane.

The last step begins by running IS from the design point given by FORM. Figure 6.9 shows the probability of failure calculated at each sample within a confidence level of 0.05. Thus, after 800 model evaluations the probability of failure converged to 64.37% within upper and lower bounds of 59.80% and 68.95% and $C_v = 0.0363$.

The graphic in fig. 6.10 shows the sampling distribution around the design point in the vertical line. The limit-state function which separates the failure and the safety zone is placed between the red and green samples in a horizontal disposition.

The safety index for importance sampling is 0.3685. Notice that failure probability for FORM is within the confidence bounds of importance sampling analysis. The undamping random analysis has taken about 4 hours and 30 minutes.

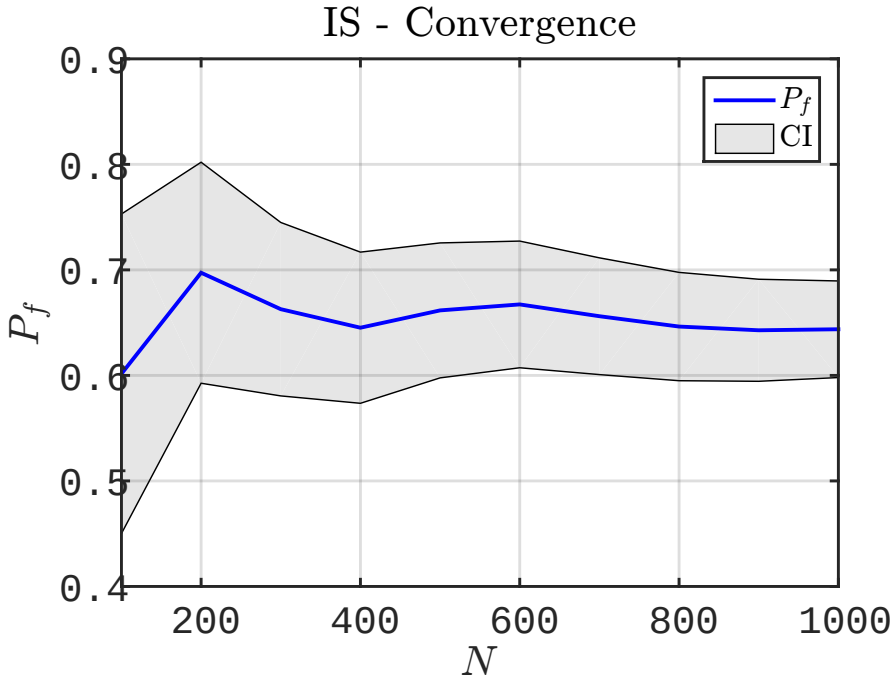

Figure 6.9: Importance sampling convergence.

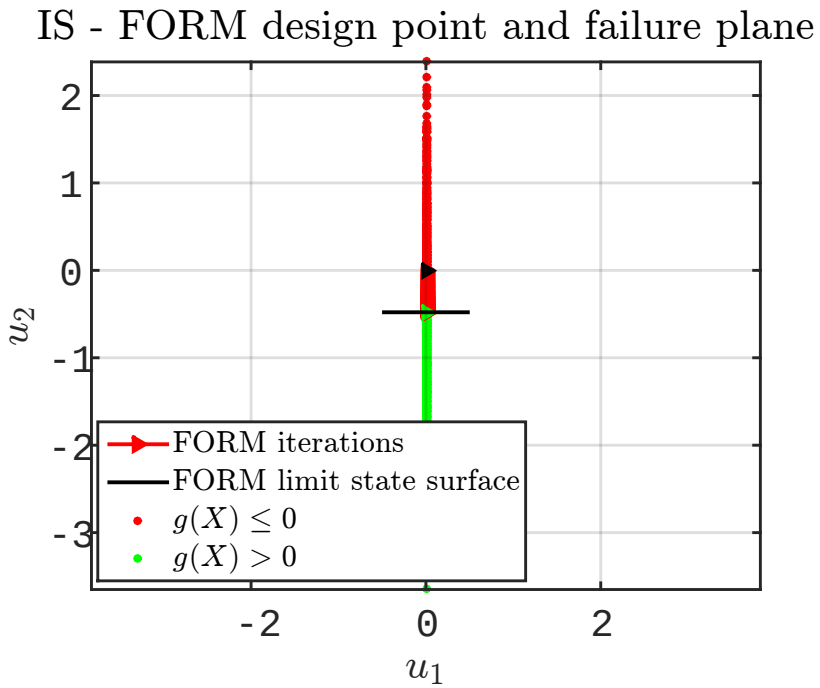

Figure 6.10: IS samples and FORM failure plane.

6.3 Uncertain stiffness and damping

Finally the analysis is brought to the case whose stiffness and damping are both random variables such that $\mathbf{x} = \{x_1, x_2\}^T$ is a joint distribution with $f_{\mathbf{x}}(x_1) \sim \mathcal{U}(1, 1.45)$ and $f_{\mathbf{x}}(x_2) \sim \mathcal{U}(1, 1.82)$.

This analysis will be split into two cases:

1. Vibration limit failure
2. Separation margin failure

The vibration limit failure is related to $G_1(\mathbf{x})$ which is the limit state whenever the amplitude vibration equals the operational speed range limit according to API 617 [4] standard.

The separation margin failure is related to $G_2(\mathbf{x})$ which occurs when the separation margin from critical to operational speed equals the required separation margin.

6.3.1 Vibration limit failure

The surrogate model for the limit-state function $G_1(\mathbf{x})$ is a Polynomial chaos expansion with a basis size of 136 vectors and a polynomial degree of 15 carried out by 500 samples. The error ε_{LOO} is around 3.1×10^{-19}. Figure 6.11 shows the graphical representation of the logarithmic spectrum of the PCE coefficients with higher order polynomials closer to zero.

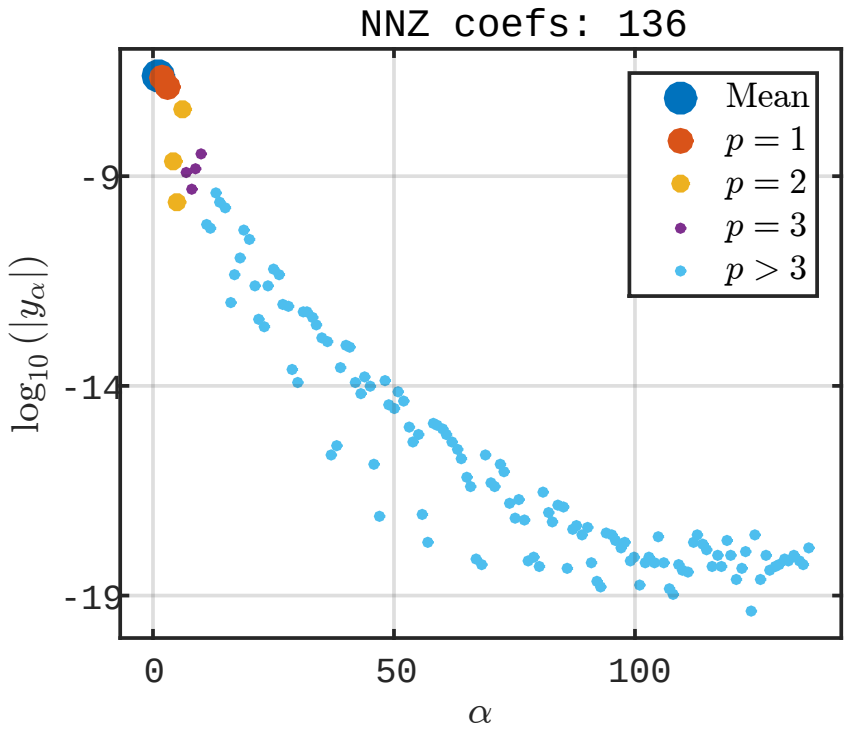

Figure 6.11: Graphical representation of the logarithmic spectrum of the PCE coefficients.

The FORM analysis from the surrogate model converged after 51 iterations and 425 models evaluation. The reliability index β_{HL} is estimated as 0.6728 as shown by fig. 6.12, i.e., the probability of failure is then 74.95%.

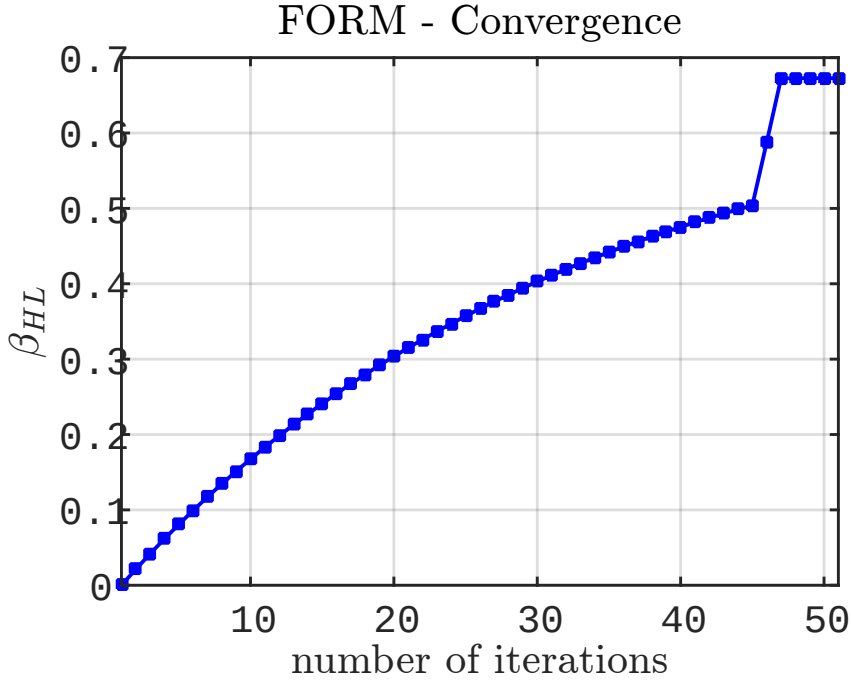

Figure 6.12: FORM analysis convergence.

Figure 6.13 shows the failure plane in the standardized space iteratively solved by

FORM with the design point which corresponds to $(-0.3909 \ -0.5475)$. The vector $\mathbf{x}$ in the original random space for the design point is defined as (1.15661.2394).

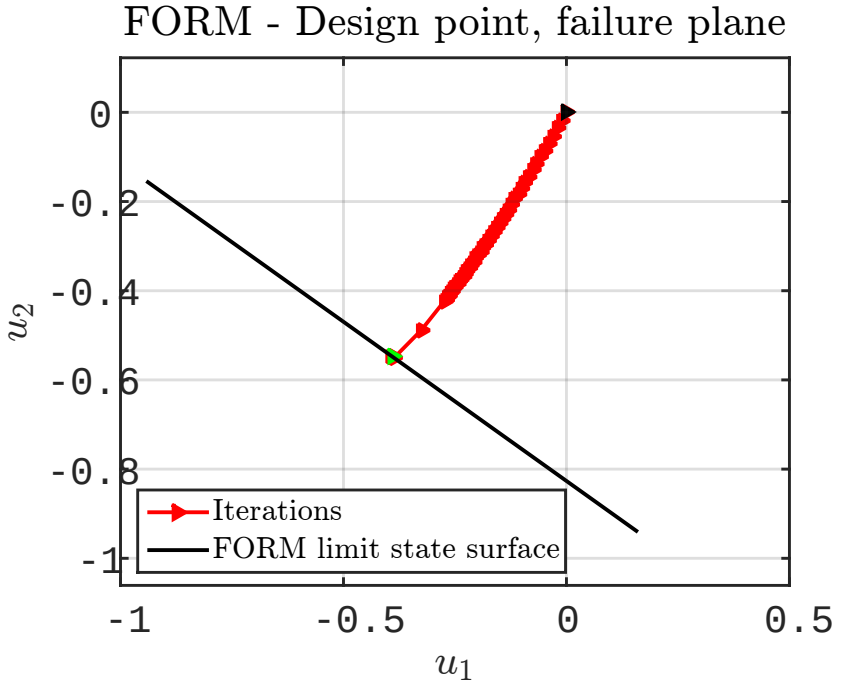

Figure 6.13: FORM design point and failure plane.

The IS convergence is shown in fig. 6.14 for 1425 models evaluations which reaches the probability of failure of 83.63%. The confidence bounds are within 78.02%, and 89.24% limits and C_v of 0.0342. Note that FORM results are out of the bounds of the confidence level which is possible outcome since this method is an approximation and importance sampling converges to the real value.

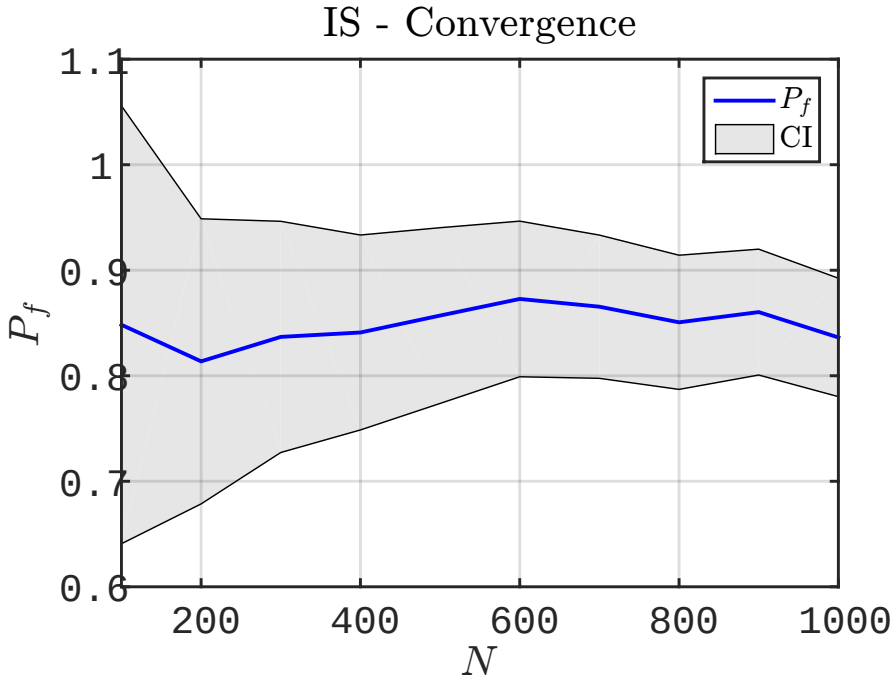

Figure 6.14: Importance sampling convergence.

Figure 6.15 shows the samples around the design point in the standard normal space. The safety index is estimated as 0.9794. This analysis has taken about 3 hours.

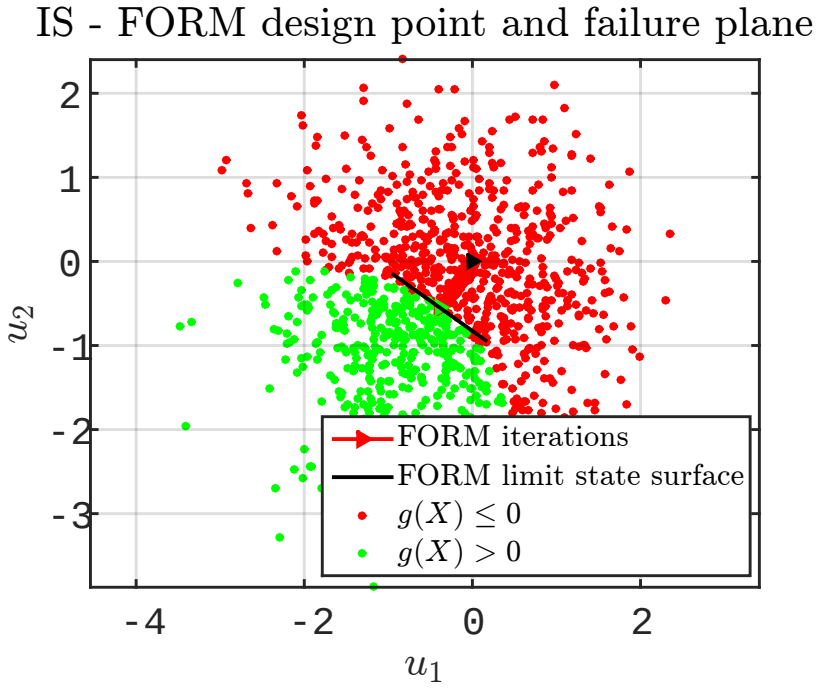

Figure 6.15: IS samples and FORM failure plane.

6.3.2 Separation margin failure

This last analysis begins with the search for the surrogate model to $G_2(\mathbf{x})$ function. Figure 6.16 shows the logarithm spectrum for the PCE coefficients after 500 samples with an error of $\varepsilon_{LOO} = 2.6 \times 10^{-3}$. The basis of the model has ten multivariate vectors with a third-degree polynomial.

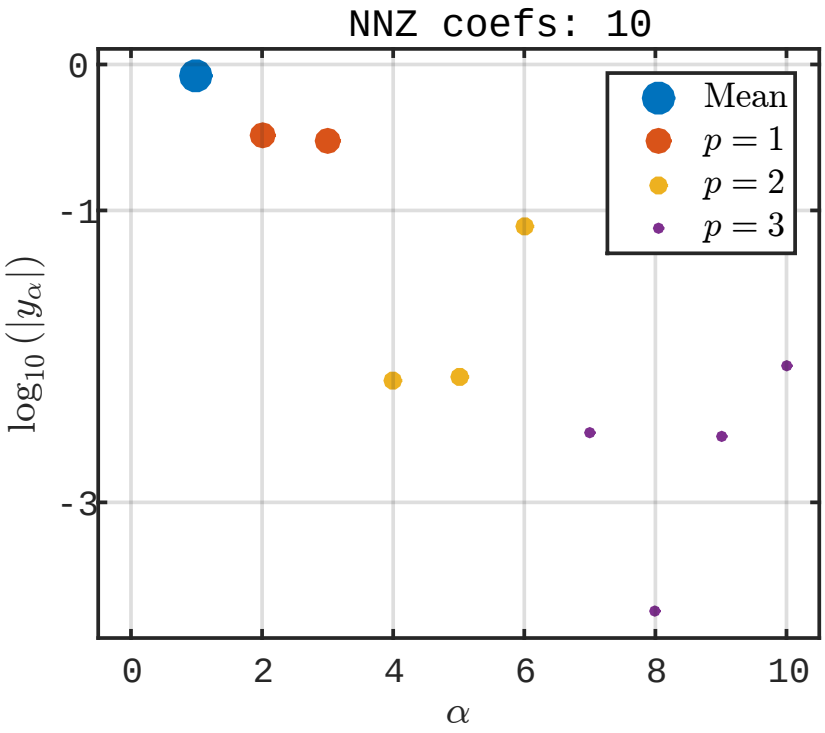

Figure 6.16: Graphical representation of the logarithmic spectrum of the PCE coefficients.

Figure 6.17 shows that FORM converges to $\beta_{HL} = 2.6463$ after 20 iterations and 108 model evaluations. FORM iterations in the standard normal space is shown in fig. 6.18 with the first order limit-state function which represents the failure plane. The design point in this space is defined by (1.84 1.91) coordinate which means (1.44 1.80) coordinate in the original space. The probability of failure is estimated as 0.41%.

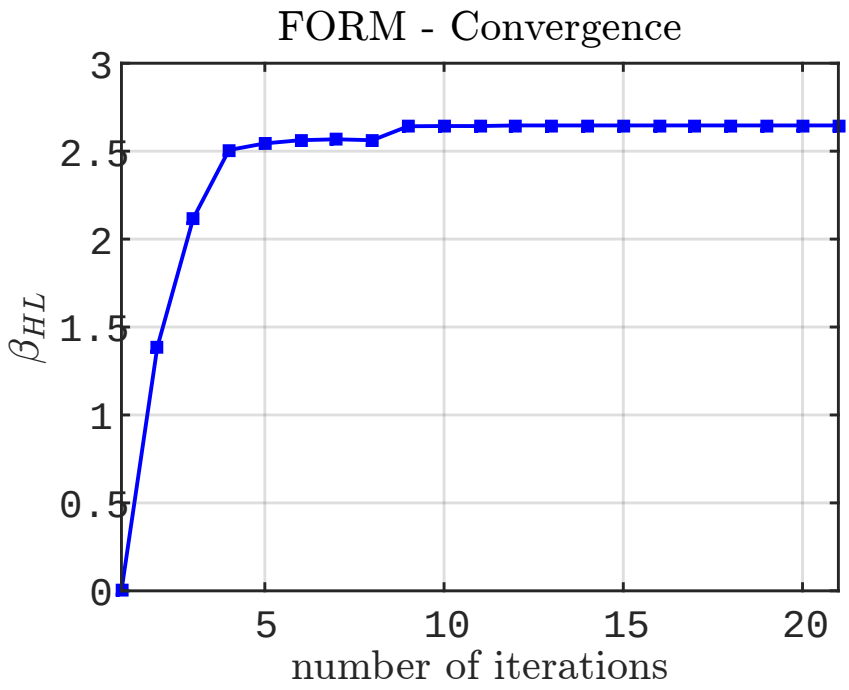

Figure 6.17: FORM analysis convergence.

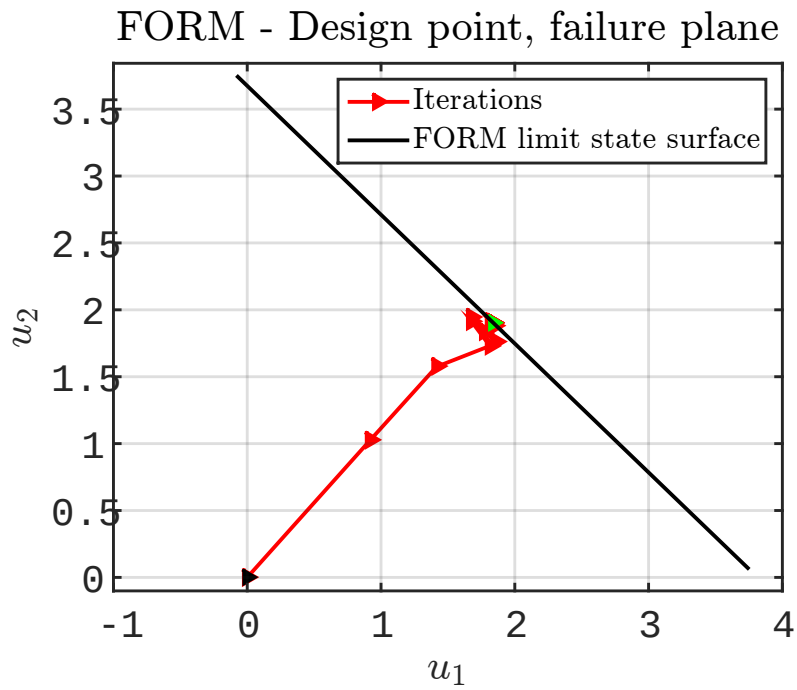

Figure 6.18: FORM design point and failure plane.

Finally, IS is carried out as shown by the convergence graphic in fig. 6.19. After 1108 model evaluations the probability of failure converged to 0.26% with confidence bounds within (0.22 0.30)% (confidence level of 0.05) and a C_v of 0.0838.

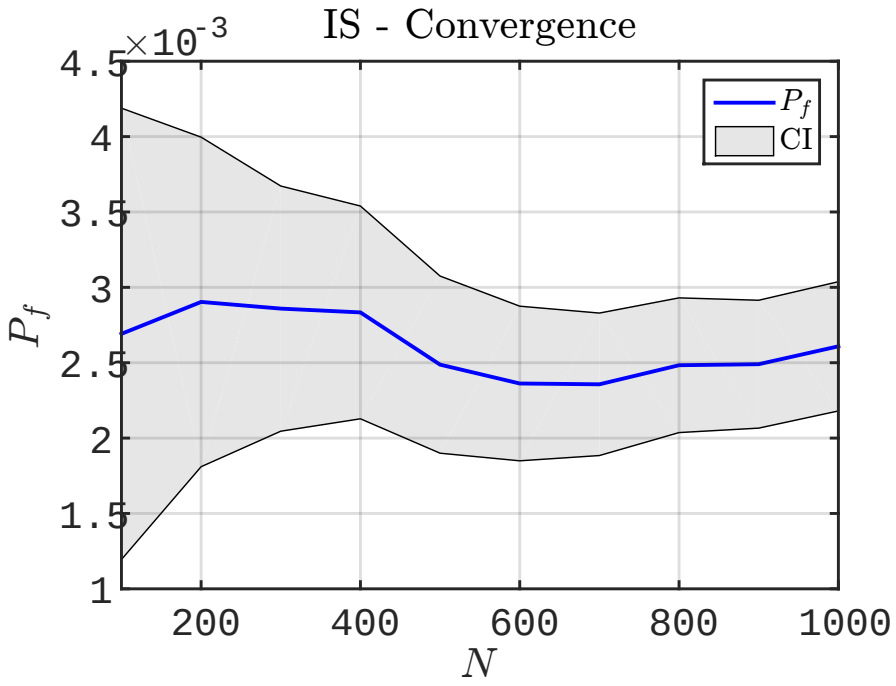

Figure 6.19: Importance sampling convergence.

Figure 6.20 shows the sample distribution around the FORM design point. The green samples represent the safe zone and the red, failure. Notice that the probability of failure estimated by FORM is out of the confidence level bounds of the importance sampling analysis. The limit-state function of the FORM algorithm has found a failure plane that is shifted upward to the right which increases FORM reliability index and therefore the probability of failure as well.

Since the importance sampling is not an approximated value, the probability of 0.26% is more accurate. The safety index is 2.7933, and the whole analysis from the surrogate model up to the importance sampling has taken 4 hours and 10 minutes.

Notice that for the probability of failure of 0.26% and covariance of 0.0838 it would take around 54400 samples for a Monte Carlos simulation which is computationally expensive.

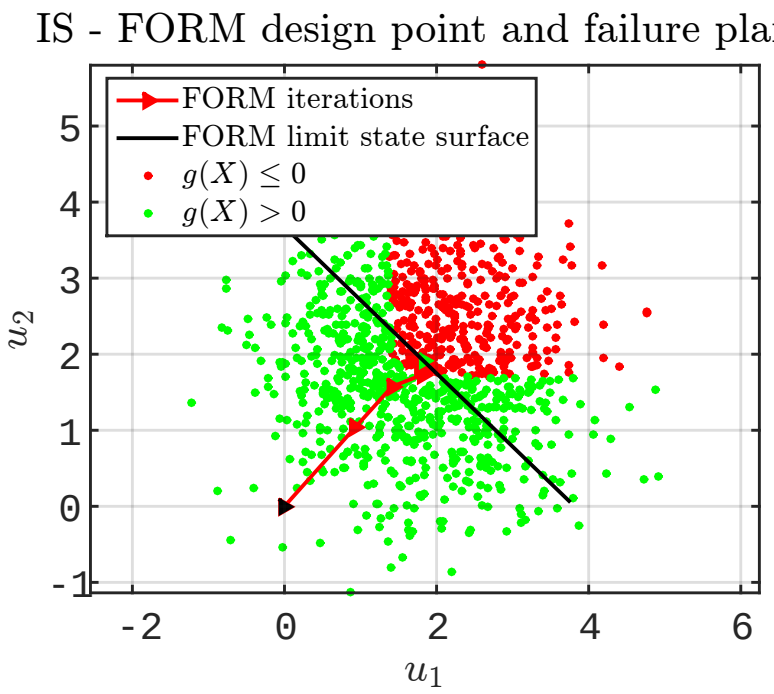

Figure 6.20: IS samples and FORM failure plane.

6.4 Reliability results analysis

The results of the reliability methods presented are in good agreement with Monte Carlos Simulations graphics displayed in chapter 4. The surrogate model construction solves the difficulty on dealing with asymmetric distributions and implicit functions as $G_1(\mathbf{x})$ and $G_2(\mathbf{x})$.

The FORM analysis which is less expensive than Importance Sampling is within confidence bounds for almost analyses which were carried out. Only to $G_2(\mathbf{x})$ which represents the probability of not meeting [4] separation margin criterion, the FORM analysis is out of 95% of the confidence bounds. Notice that FORM failure plane sometimes does not match with importance sampling fail samples. This difference relies on the nonlinearity of the limit-state functions. It stresses the application of Importance Sampling for low probability of failure instead of FORM analysis and Monte Carlo simulations.

Once the reliability analysis tools are available, it is possible to construct different scenarios of machine severity level in which the probability of failure is evaluated.

Chapter 7

Unbalance response scenarios

The compressors in oil and gas industry are supposed to run for at leat 20 years. The maximum allowable residual unbalance U_r is an API 617 [4] requirement for new compressors. The unbalance magnitude may vary along its life cycle which could compromise the mechanical integrity. In order to evaluate the impact of the imbalance, the reliability analyses will be applied to three scenarios of unbalance magnitudes on both compressors models built: $2 \times U_r$, $4 \times U_r$ and $8 \times U_r$.

7.1 Compressor I

7.1.1 Separation Margin

The first compressor model with uncertainties on bearing coefficients will focus the vibration limit and the separation margin from critical speed requirements. Figure 7.1, fig. 7.2 and fig. 7.3 shows the actual and required separation margin PDF's with low sensitivity to unbalance magnitude.

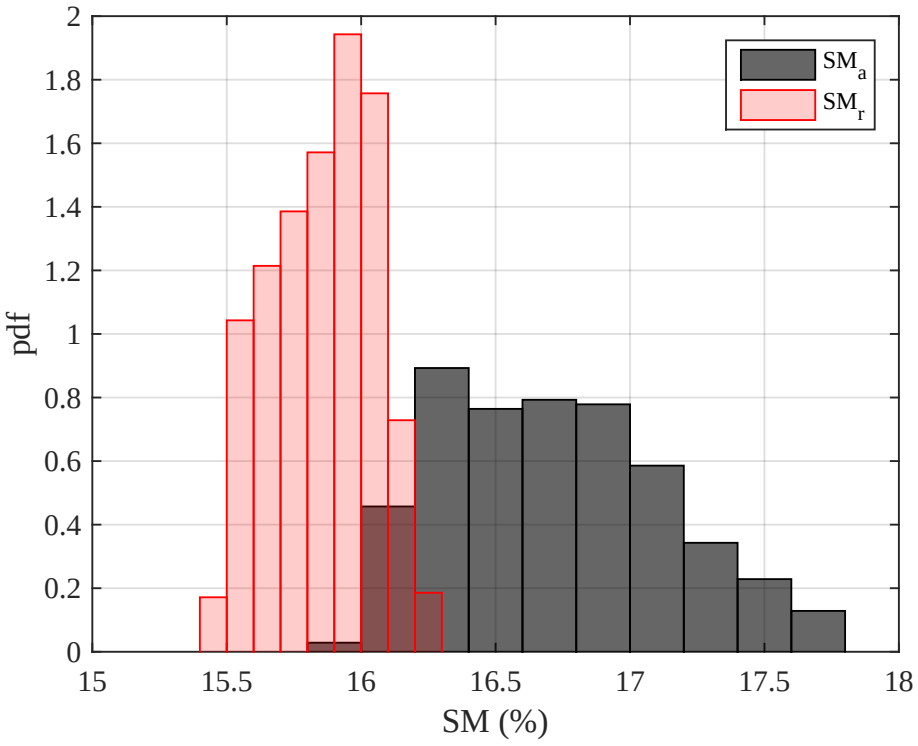

Figure 7.1: Required and actual separation margin PDF's for $2 \times U_r$.

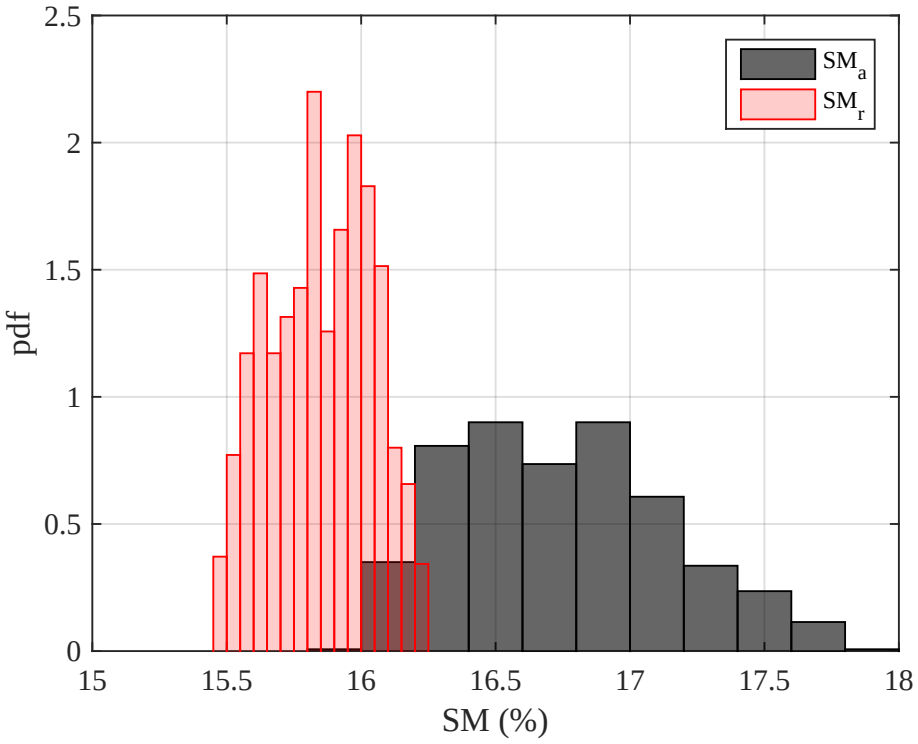

Figure 7.2: Required and actual separation margin PDF's for $4 \times U_r$.

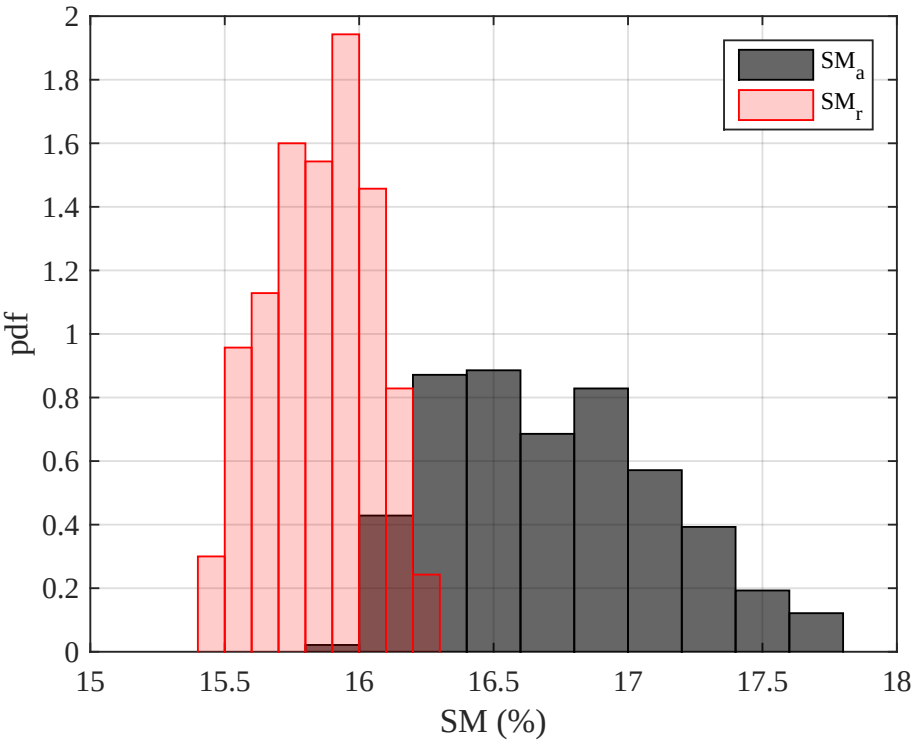

Figure 7.3: Required and actual separation margin PDF's for $8 \times U_r$.

Figure 7.4 shows the probability of failure for those unbalance magnitudes by First-Order Reliability Method and Importance Sampling. The FORM analysis depends on the accuracy of the surrogate model, and it is an approximation as well. The Importance Sampling estimates the probability of failure between 2.6×10^{-3} and 3.1×10^{-3} which means a coefficient of variation of 26.2%. The FORM estimates the probability of failure between 2.7×10^{-3} and 4.1×10^{-3} which is associated to a coefficient of variation between FORM and Importance Sampling of 15.6%, 30.9% and 9.1% to each unbalance magnitude. To decrease the deviation is possible to refine the surrogate model. For instance, a surrogate model for $4 \times U_r$ case built with 600 samples, i.e %20 more model evaluations yields 3.8×10^{-3} (FORM) and 2.5×10^{-3}(IS) which decreases the coefficient of variation to 29.2% . Note that the limit-state function does not have a linear output which increases the error to the probability of failure by FORM.

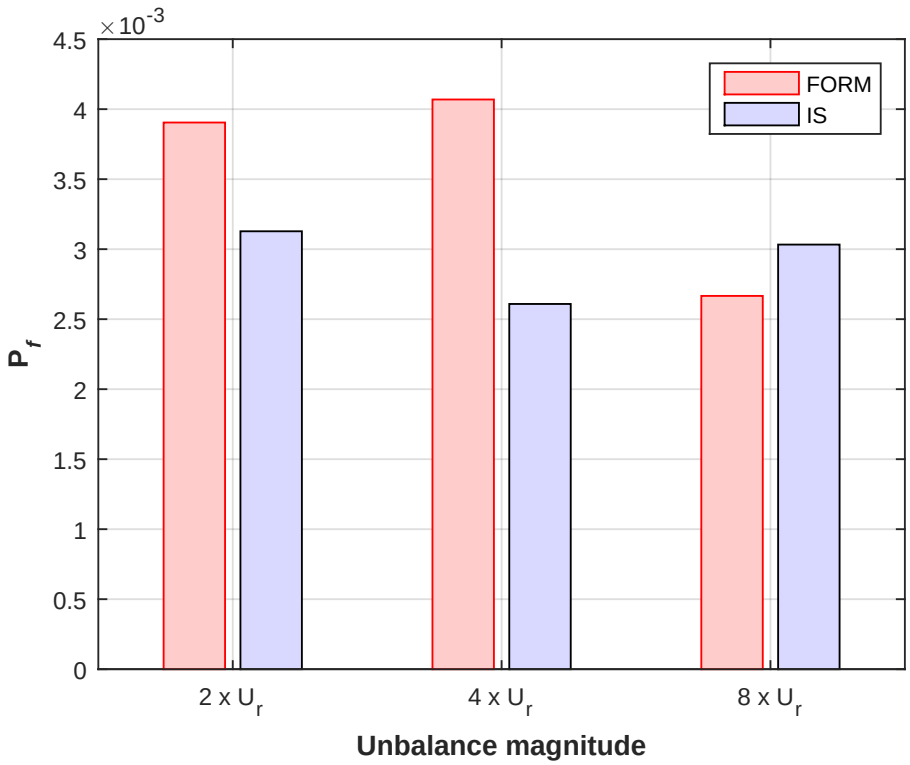

Figure 7.4: Failure probability based on separation margin × Unbalance magnitude.

The number of samples required for a Monte Carlos simulation to achieve a probability of failure with the same coefficient of variation to the Importance Sampling is plotted in fig. 7.5 as well as the number of samples carried out in FORM and Importance Sampling analysis. Despite being more expensive than FORM, Importance Sampling is effortlessly in comparison to a Monte Carlos simulation.

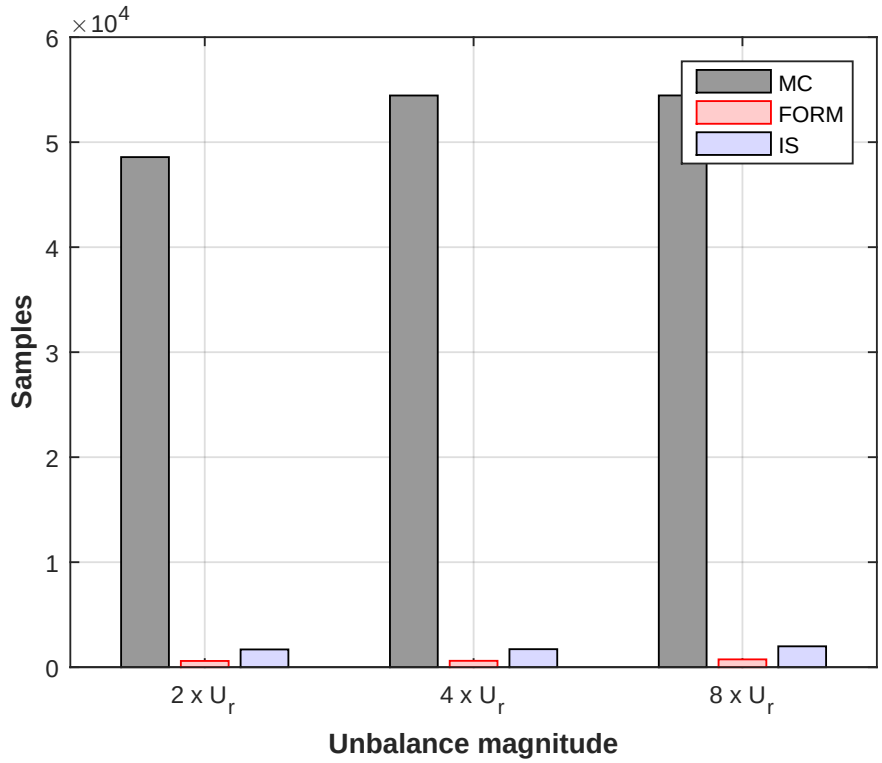

Figure 7.5: Number of samples required for each reliability method.

To understand the behavior of the probability of failure to different unbalance magnitude scenarios is not an easy task. The separation margin distributions shows that unbalance magnitude does not effect on the lateral critical speed. Notice that even four times the amount of unbalance changes the probability of failure from 0.31% to 0.27% by Importance Sampling analysis and the uncertainty propagation is not linear.

7.1.2 Vibration Limit

The maximum amplitude within operational speed sensitivity is shown in fig. 7.6 to fig. 7.8. The maximum response is quite below the vibration limit with the minimum unbalance, and the response exceeds the limit with maximum unbalance otherwise.

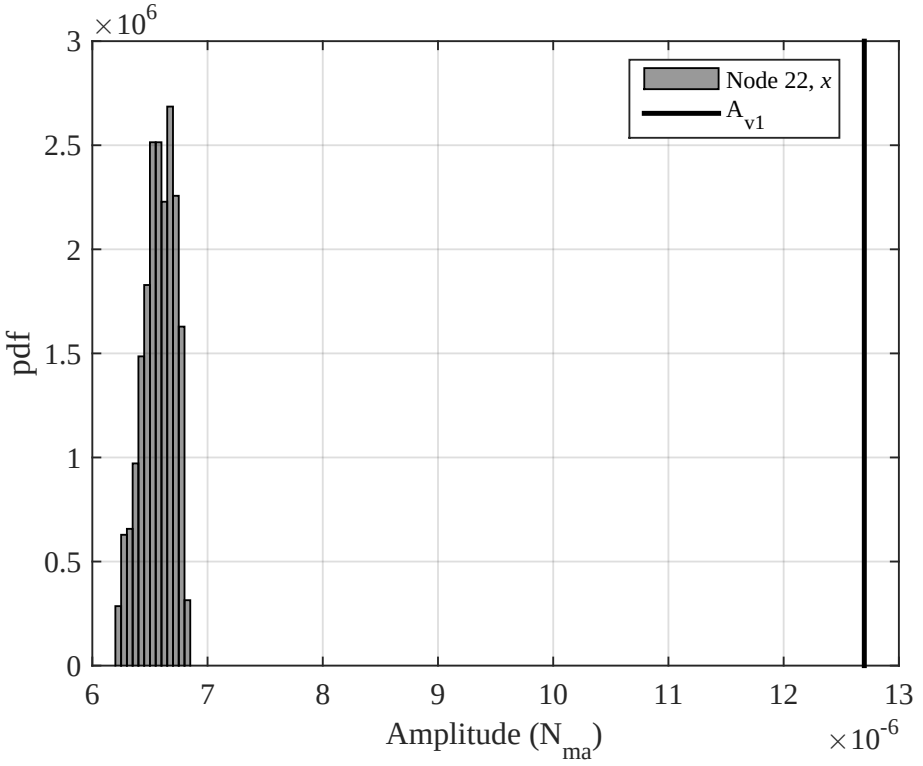

Figure 7.6: Maximum amplitude PDF within operational speed for $2 \times U_r$.

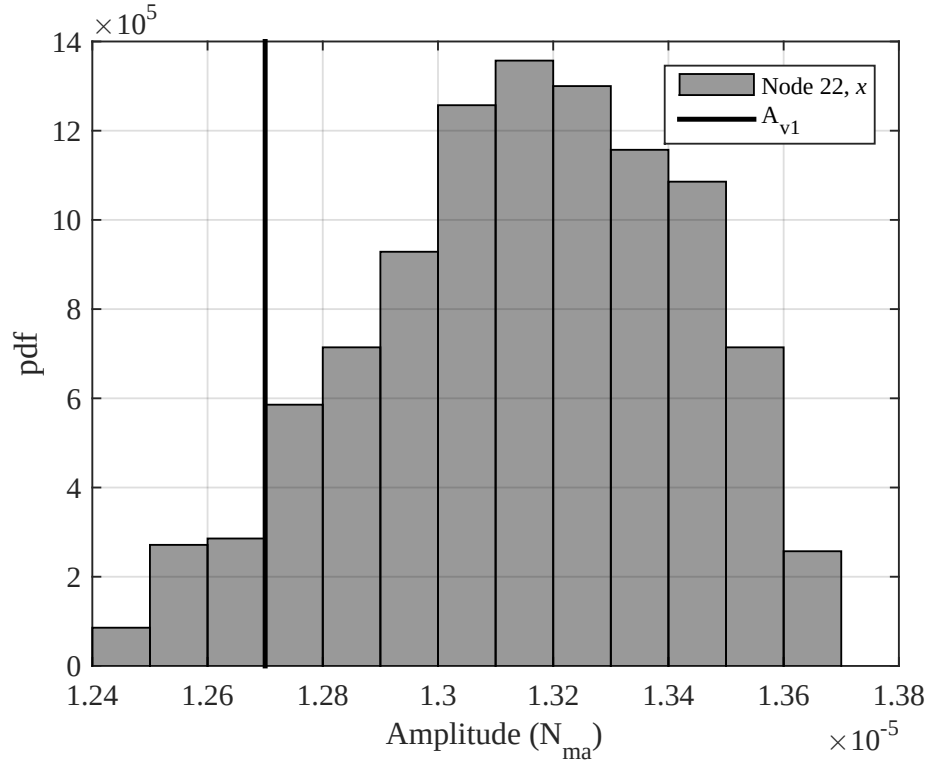

Figure 7.7: Maximum amplitude PDF within operational speed for $4 \times U_r$.

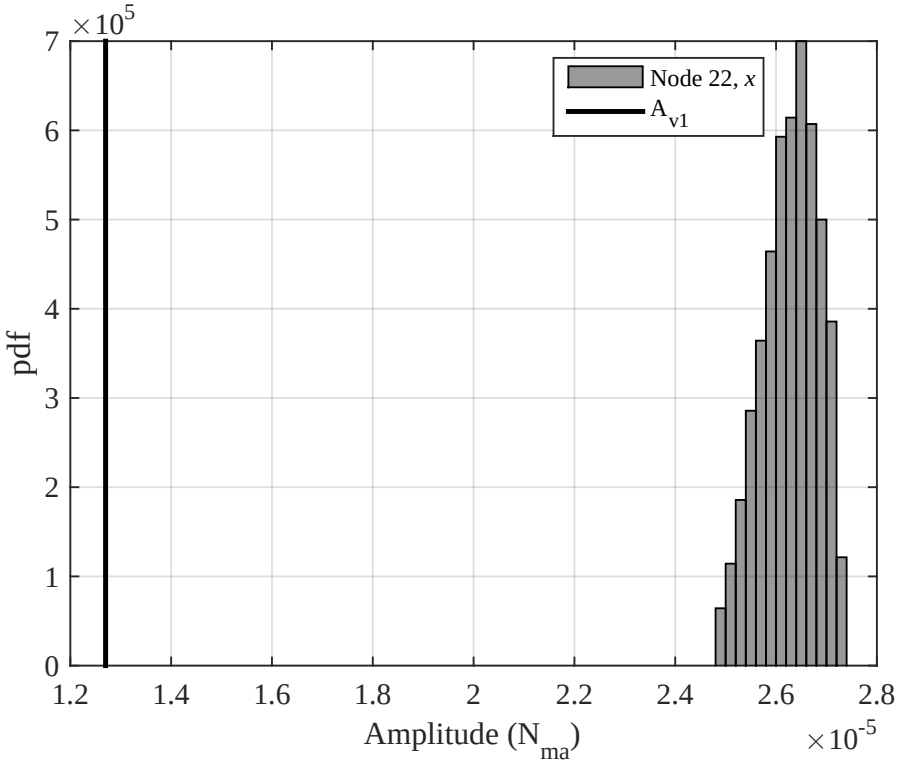

Figure 7.8: Maximum amplitude PDF within operational speed for $8 \times U_r$.

Figure 7.9 shows the probability of failure when the unbalance magnitude is $4 \times U_r$. The mean value from FORM and IS is 79.5% with a coefficient of variation from 7.7% which shows how critical is the control of the unbalance in the manufacturing process and during the operation. A drawback from Importance Sampling method occurs when the probability of failure is too high. Figure 7.10 shows that Monte Carlos is more effective than other reliability methods to evaluate a higher probability of failure.

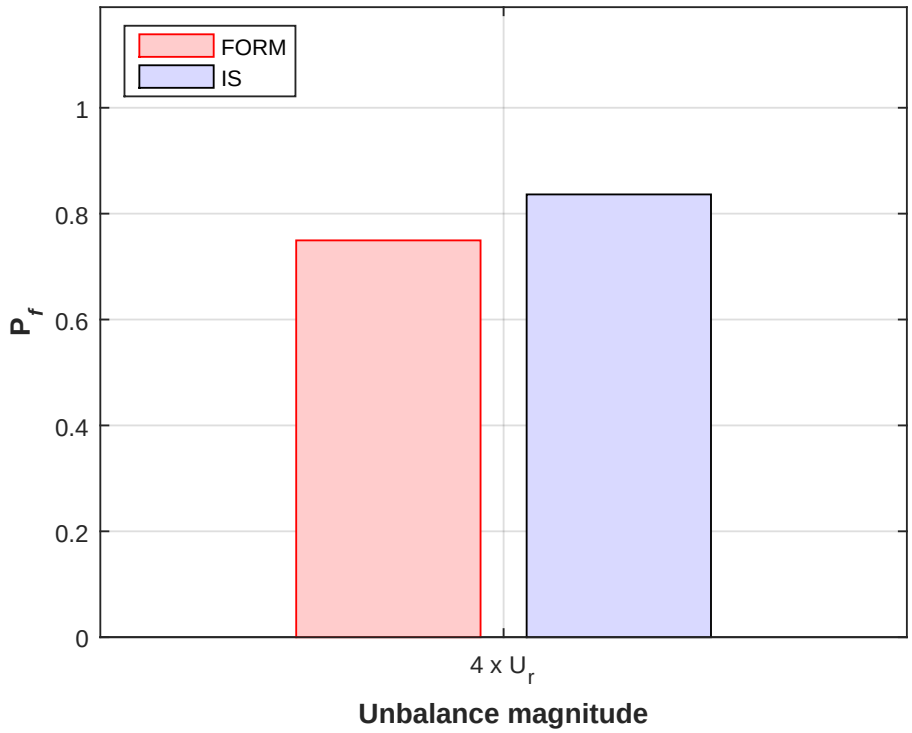

Figure 7.9: Failure probability based on vibration limit × Unbalance magnitude.

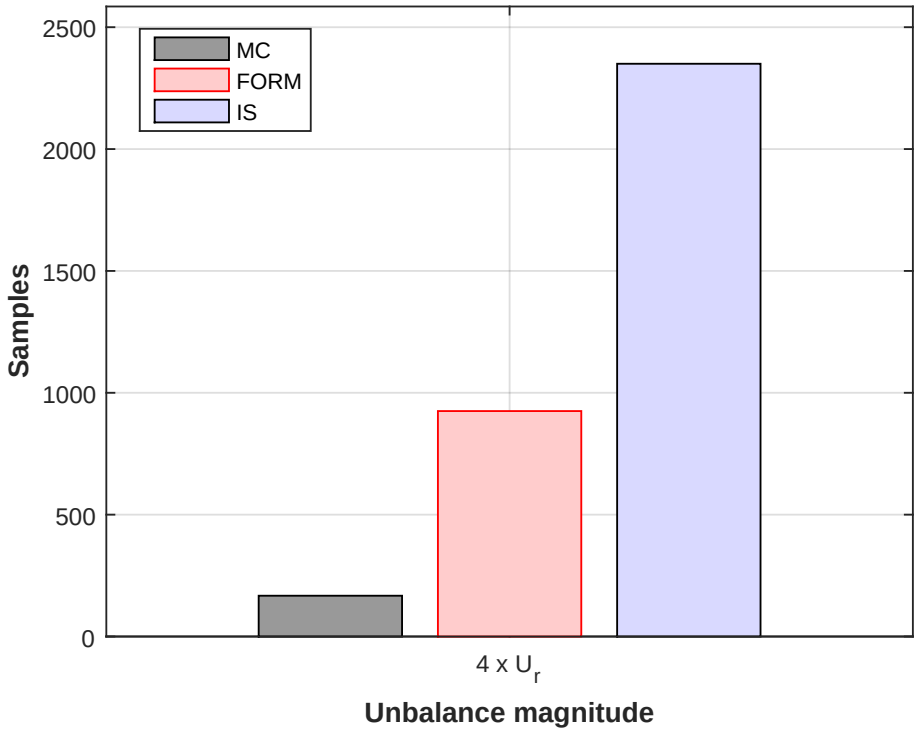

Figure 7.10: Number of samples required for each reliability method.

7.2 Compressor II

7.2.1 Minimum Clearance

The second analysed compressor is designed with the critical speeds far from operational speed and the amplitude within operational speed reasonably below the vibration limit. However, the bearing clearance when the second mode is excited is relative small with regard to uncertanties on bearings coefficients.

Figure 7.11 shows the scale response PDF for minimum unbalance magnitude which is clearly below the bearing clearance. Figure 7.12 shows scaled response PDF for $4 \times U_r$. When the unbalance raises to $8 \times U_r$ the maximum response is almost the same, only the deviation lowers. The scale factor S_{cc} lowers as the maximum amplitude approaches the minimum clearance and therefore the coefficient of variation of the scale response is lowered. The coefficients of variation for scale factor are 16.3%, 12.3% and 3.5% for $2 \times U_r$, $4 \times U_r$ and $8 \times U_r$, respectively.

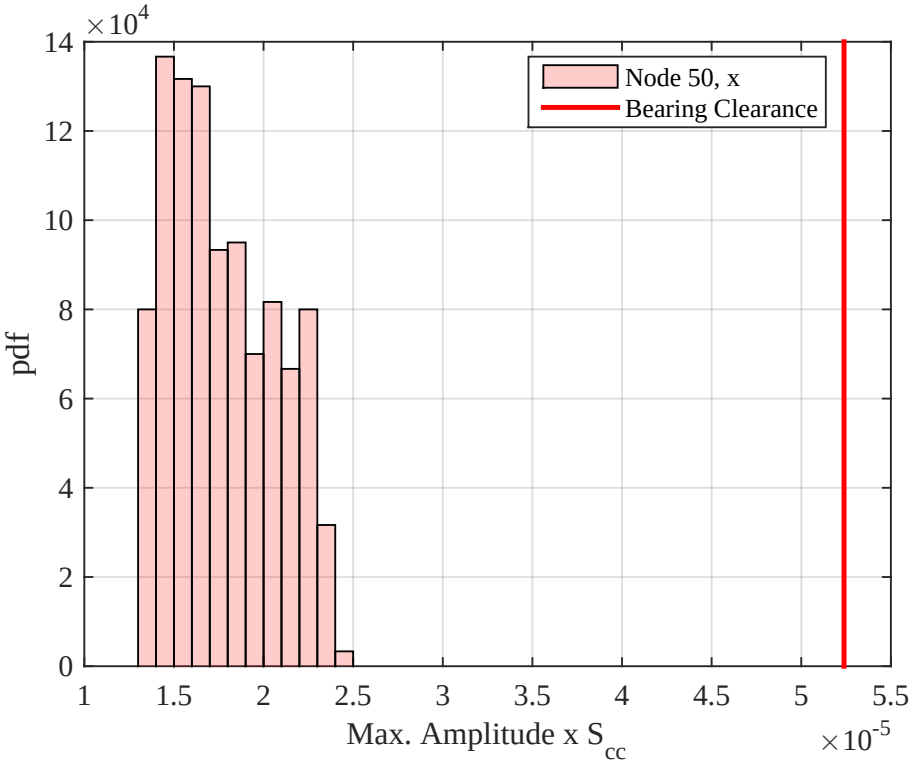

Figure 7.11: Scaled response PDF for $2 \times U_r$.

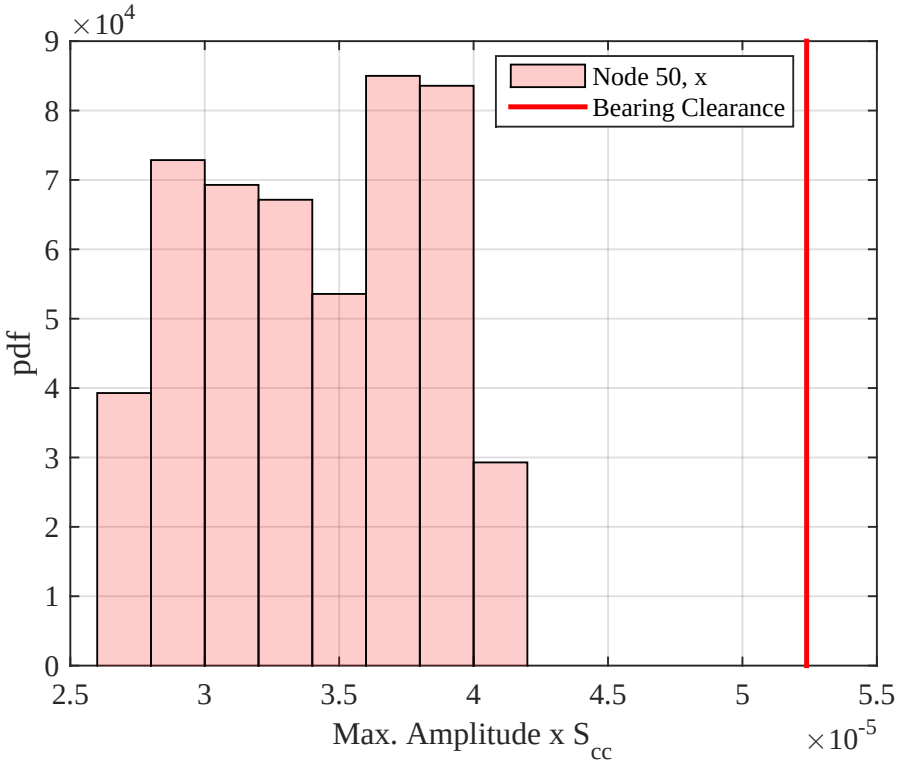

Figure 7.12: Scaled response PDF for $4 \times U_r$.

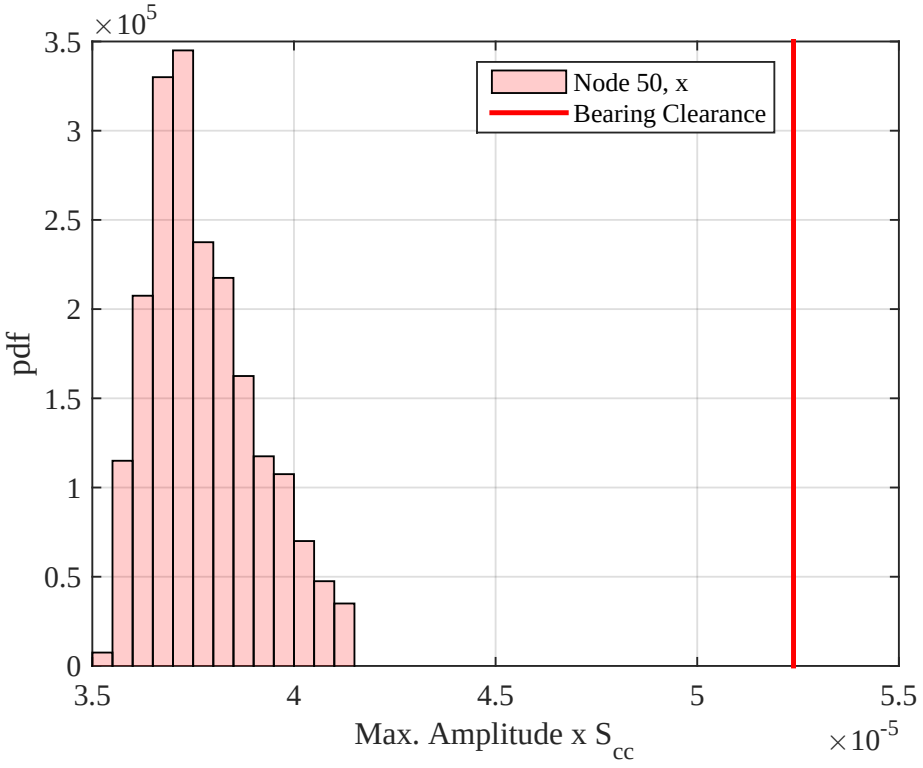

Figure 7.13: Scaled response PDF for $8 \times U_r$.

Chapter 8

Conclusions

8.1 Conclusions

The model of lateral rotor vibration helped to understand the behavior of gas reinjection compressors into oil reservoir and whether uncertainties on bearings coefficients impact on oil and gas design acceptance requirements. Above all, if uncertainties on these coefficients impact on safe conditions during the equipment life cycle. Both compressors operate at high speeds which require the machines to work after the first critical speed. The stochastic model to the forced response relied on uncertainties within experimental investigation on tilting pad bearings. For some compressors designed for gas reinjection as the compressor I in this dissertation, the first critical is close to the required separation margin, and the vibration limit within operational speed is a concern as well.

For other compressors as the second one in this dissertation, the design provides better margins to a safer operation. The higher bearing span and rotor mass tends to decrease the critical speeds. Therefore, the second critical speed has a higher impact on the rotordynamic design, and minimum clearance between stationary and rotary parts are a concern.

The reliability methods to calculate the probability of failure, i.e., not meeting API 617 [4] design requirements are potent tools. First-order reliability method and Importance Sampling for implicit limit-state functions requires a particular approach. The choose of the surrogate model instead of a direct approach or a finite difference scheme that require adaptations on the First-Order Reliability method algorithm proved to be effective on computational effort. High failure probability with lower accuracy makes FORM and Importance Sampling more expensive, and a Monte Carlos simulation may be used. However, a low probability of failure as for the required separation to the first compressor is a perfect case when Importance Sampling is a powerful tool.

The application of the reliability tools for different scenarios of unbalance magnitudes helped to understand that the response within operational speed is profoundly affected which compromises the vibration limit for the first compressor. The first compressor model shown that the unbalance magnitude impact is not an issue to the separation margin since the critical speed is more affected by rotor geometry, mass and bearing characteristics.

For the second compressor, the scaled response considers the linear behavior of the deterministic model and the maximum response up to 150% the maximum speed if the vibration limit within operational speed would be reached. Therefore, the scaled response was major affected by a decrease in the coefficient of variation and less by the upper limit of the envelope for severer unbalance scenarios.

As for the imbalance scenarios, the first compressor has a probability of failure less than 0.0% if the unbalance magnitude does not exceed twice the factory residual unbalance which demands higher investments on the operation, for instance, predictive maintenance. However, four times the factory residual imbalance leads the probability of failure to almost 84%. The second compressor operates with better margins to the available standards criteria regardless of the imbalance scenarios.

To summarize, this dissertation constructed a time efficient reliability analysis to different scenarios of a compressor life cycle that helps to evaluate how reliable is the machinery design with respect to lateral vibrations.

8.2 Future developments

This work acknowledges the important role that tilting pad bearing plays at oil and gas compressors design. In order to decrease the level of uncertainty on bearings coefficients, a validation through experimental tests would improve the accuracy of the model. A bayesian parameter estimation is a tool that could improve the distribution of the random variables within the bearing model and could be at further improvements on this subject.

Mechanical running test which does only with air and no pressure could be used to compare with the rotor-impellers-bearing system model output.

Further investigations on instabilities require seals to be assembled on the model and considerations of the gas density and aero cross-coupling effects as well. Since these compressors are subjected to high pressures the model evaluation and experimental validations are a subject itself which can be discussed on other projects and future developments.

Bibliography

[1] LÜDTKE, K. H. *Process centrifugal compressors: basics, function, operation, design, application*. Springer Science & Business Media, 2013.

[2] DIMOND, T. W. *Modeling of fluid film bearings and design of a fluid film bearing test rig*. Tese de Doutorado, University of Virginia School of Engineering and Applied Science, 2011.

[3] API 684, A. . "API 684, 2005", *Tutorial on Rotordynamics: Lateral Critical, Unbalance Response, Stability, Train Torsional and Rotor Balancing," Second Edition, American Petroleum Institute, Washington, DC*, 2005.

[4] API 617, A. . "API 617, 2014", *Axial and Centrifugal Compressors and Expander-Compressors" Eighth Edition, American Petroleum Institute, Washington, DC*, 2014.

[5] MELCHERS, R. E. *Structural reliability analysis and prediction*. John Wiley & Sons, 1999.

[6] NIKOLAIDIS, E., GHIOCEL, D. M., SINGHAL, S. *Egineering Design Reliability Handbook*. CRC Press LLC, 2000.

[7] MARELLI, S., SCHÖBI, R., SUDRET, B. *UQLab user manual – Reliability analysis*. Relatório técnico, Chair of Risk, Safety & Uncertainty Quantification, ETH Zurich, 2018. Report # UQLab-V1.1-107.

[8] DMOCHOWSKI, W., BROCKWELL, K. "Dynamic testing of the tilting pad journal bearing", *STLE Tribology transactions*, v. 38, n. 2, pp. 250–256, 1995.

[9] WYGANT, K. D., BARRET, L. E., FLACK, R. D. "Influence of Pad Pivot friction on tilting-pad journal bearing measurements - Part II: Dynamic coefficients", *STLE Tribology transactions*, v. 42, n. 1, pp. 250–256, 1999.

[10] ISO 21940-11, I. .-. "ISO 21940-11, 2016", *Mechanical vibration — Rotor balancing — Part 11: Procedures and tolerances for rotors with rigid be-*

haviour" First Edition, International Organization for Standardization, Geneva, Switzerland, 2016.

[11] MEIROVITCH, L. *Elements of vibration analysis*. McGraw-Hill, 1986.

[12] LALANNE, M., FERRARIS, G. *Rotordynamics prediction in engineering*. John Wiley & Sons, 1998.

[13] FRISWELL, M. I. *Dynamics of rotating machines*. Cambridge University Press, 2010.

[14] HE, M., ALLAIRE, P. *Analysis of fluid film journal bearings*. Relatório técnico, University of Virginia School of Engineering and Applied Science, 2003. Report No. UVA/643092/MAE03/595.

[15] HE, M. *A manual for use with the fluid film journal bearing code MAXBRG BETA 1.0*. University of Virginia School of Engineering and Applied Science, 2001.

[16] INMAN, D. J. *Engineering Vibration*. Pearson, 2014.

[17] SHANNON, C. E. "A Mathematical Theory of Communication", *The Bell System Technical Journal*, v. 27, n. 1, pp. 379–423, 623–656, 1948.

[18] RUBINSTEIN, G. R. Y., KROESE, D. P. *Simulation and the Monte Carlo Method*. John Wiley & Sons, 2016.

[19] SILVA, R. T. *Impact of damper seal coefficients uncertainties in rotor dynamics*. Tese de Mestrado, Universidade Federal do Rio de Janeiro, 2018.

[20] KIUREGHIAN, A. D., KE, J.-B. "The stochastic finite element method in structural reliability", *Probabilistic Engineering Mechanics*, v. 3, n. 2, 1988.

[21] ROSENBLATT, M. "Remarks on a multivariate transformation", *The Annals of Mathematical Statistics*, v. 23, pp. 470–472, 1952.

[22] HASOFER, A. M., LIND, N. C. "Exact and invariant second moment code format", *The Annals of Mathematical Statistics*, v. 100, n. 1, pp. 111—-121, 1974.

[23] RACKWITZ, R., FIESSLER, B. "Structural reliability under combined load sequences", *Computers & Structures*, v. 9, pp. 489—-494, 1978.

[24] LIU, P. L., DER KIUREGHIAN, A. "Optimization algorithms for structural reliability", *tructural Safety*, v. 9, n. 3, pp. 161—-177, 1991.

[25] ZHANG, Y., DER KIUREGHIAN, A. "Two improved algorithms for reliability analysis", *In Reliability and Optimization of Structural Systems, Proceedings of the 6th IFIP WG 7.5 Working Conference on Reliability and Optimization of Structural Systems, 1994, (R. Rackwitz, G. Augusti, and A. Borri, Eds.)*, pp. 297—-304, 1995.

[26] SUDRET, B., KIUREGHIAN, A. D. "Comparison of finite element reliability methods", *Probabilistic Engineering Mechanics*, v. 17, pp. 337–348, 2002.

[27] SUDRET, B., KIUREGHIAN, A. D. *Stochastic Finite Element Methods and Reliability – A State-of-the-Art Report*. Relatório técnico, Department of Civil & Environmental Engineering University of California, Berkley, 2000. Report No. UCB/SEMM-2000/08.

[28] MARELLI, S., SUDRET, B. *UQLab user manual – Polynomial chaos expansions*. Relatório técnico, Chair of Risk, Safety & Uncertainty Quantification, ETH Zurich, 2018. Report # UQLab-V1.1-104.

Appendix A

Model Development

A.1 Elements

A.1.1 Disk

Modeling the disk from the energy point of view begins with the assumption of a rigid behavior. Therefore, it has only kinetic energy.

The kinetic energy equation of the disk is:

$$T_d = \frac{1}{2}m_d(\dot{u}^2 + \dot{u}^2) + \frac{1}{2}I_{d_x}(\omega_x^d)^2 + \frac{1}{2}I_{d_y}(\omega_y^d)^2 + \frac{1}{2}I_{d_z}(\omega_z^d)^2 \tag{A.1}$$

where I_{d_x} is the moment of inertia about axis x, I_{d_y} the moment of inertia about axis y, and I_{d_z} about axis z ; m_d the disk mass; and angles with respective angular velocities as shown by fig. A.1.

Figure A.1a shows the inertial frame $R_0(XYZ)$ and the rotation by ψ around Y axis. Figure A.1a shows the rotation by θ around new X_1 axis. Finally, fig. A.1a shows the rotation by ϕ around new x axis which leads to the frame $R(xyz)$ fixed in the disk.

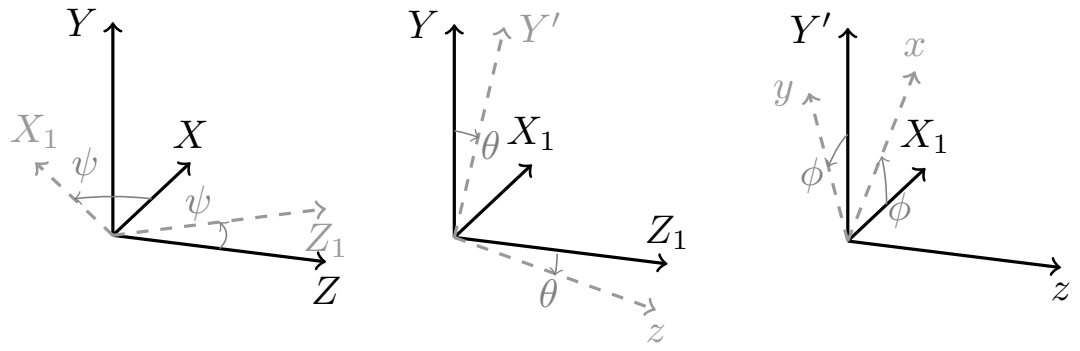

(a) Disk rotation by ψ around Y axis (b) Disk rotation by θ around X_1 axis (c) Disk rotation by ϕ around y axis

Figure A.1: Disk rotations with reference frames

The angular velocity of the disk is then,

$$\omega^d = \dot{\phi}\hat{z} + \dot{\theta}\hat{X}_1 + \dot{\psi}\hat{Y} \tag{A.2}$$

The projections of axis X_1 and Y onto the disk frame $R(xyz)$ are:

$$\hat{X}_1 = \cos\phi\hat{x} - \sin\phi\hat{y} \tag{A.3}$$

$$\begin{aligned}\hat{Y} &= \cos\theta\hat{Y'} - \sin\theta\hat{z} \\ &= \cos\theta(\cos\phi\hat{y} + \sin\phi\hat{x}) - \sin\theta\hat{z}\end{aligned} \tag{A.4}$$

The substitution of eq. (A.3) and eq. (A.4) in eq. (A.2) leads to the angular velocity expression in $R(xyz)$. Thus,

$${}^R\omega^d = \begin{bmatrix}\omega_x^d \\ \omega_y^d \\ \omega_z^d\end{bmatrix} = \begin{bmatrix}\dot{\theta}\cos\phi + \dot{\psi}\cos\theta\sin\phi \\ \dot{\psi}\cos\theta\cos\phi - \dot{\theta}\sin\phi \\ \dot{\phi} - \dot{\psi}\sin\theta\end{bmatrix} \tag{A.5}$$

For a symmetric disk ($I_{d_x} = I_{d_y}$), small angles θ and ψ, and a constant angular velocity $\dot{\phi} = \Omega$, the kinetic energy in eq. (A.1) may be recast by the substitution of eq. (A.5) as:

$$T_d = \frac{1}{2}m_d(\dot{u}^2 + \dot{v}^2) + \frac{1}{2}I_d(\dot{\theta}^2 + \dot{\psi}^2) + \frac{1}{2}I_p(\Omega^2 - 2\Omega\dot{\psi}\theta) \tag{A.6}$$

where I_p is the polar moment of inertia about the shaft and I_d is the diametral moment of inertia about an axis perpendicular to the shaft line. The last term $I_p\Omega\dot{\psi}\theta$ represents the gyroscopic effect.

Thus, applying Lagrange's equations:

$$\begin{bmatrix}\frac{d}{dt}\left(\frac{\partial T_d}{\partial \dot{u}}\right) - \frac{\partial T_d}{\partial u} \\ \vdots \\ \frac{d}{dt}\left(\frac{\partial T_d}{\partial \dot{\psi}}\right) - \frac{\partial T_d}{\partial \psi}\end{bmatrix} = \begin{bmatrix}m_d & 0 & 0 & 0 \\ 0 & m_d & 0 & 0 \\ 0 & 0 & I_d & 0 \\ 0 & 0 & 0 & I_d\end{bmatrix}\begin{bmatrix}\ddot{u} \\ \ddot{v} \\ \ddot{\theta} \\ \ddot{\psi}\end{bmatrix} + \Omega\begin{bmatrix}0 & 0 & 0 & 0 \\ 0 & 0 & 0 & 0 \\ 0 & 0 & 0 & I_p \\ 0 & 0 & -I_p & 0\end{bmatrix}\begin{bmatrix}\dot{u} \\ \dot{v} \\ \dot{\theta} \\ \dot{\psi}\end{bmatrix} \tag{A.7}$$

Hence, the mass matrix for the disk is

$$\mathbf{M}_e = \begin{bmatrix}m_d & 0 & 0 & 0 \\ 0 & m_d & 0 & 0 \\ 0 & 0 & I_d & 0 \\ 0 & 0 & 0 & I_d\end{bmatrix} \tag{A.8}$$

and the gyroscopic matrix yields

$$\mathbf{G}_e = \begin{bmatrix} 0 & 0 & 0 & 0 \\ 0 & 0 & 0 & 0 \\ 0 & 0 & 0 & I_p \\ 0 & 0 & -I_p & 0 \end{bmatrix} \tag{A.9}$$

A.1.2 Shaft

The shaft elements are modeled based on Timoshenko beam, i.e., shear effect and rotary inertia are included. Figure A.2 shows the angle β_e which represents the difference between the plane of the beam cross-section and the normal to the beam centerline after deformation. The angle which the beam cross-section rotates due to deformation, ψ_e, the shear angle β_e and the slope of the centerline $\partial u_e/\partial\xi$ are related by the equation:

$$\psi_e(\xi, t) = \frac{\partial u_e(\xi, t)}{\partial \xi} + \beta_e(\xi, t) \tag{A.10}$$

where u_e is the lateral displacement.

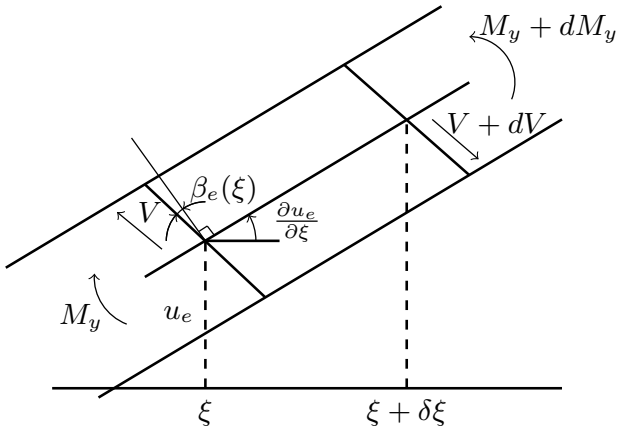

Figure A.2: Small section of a Timoshenko beam at plane XZ.

The bending moment is given by

$$E_e I_{e_y} \frac{\partial \psi_e(\xi, t)}{\partial \xi} = M_{e_y}(\xi, t) \tag{A.11}$$

and the shear force,

$$\kappa_e A_e G_e \left[\psi_e(\xi, t) - \frac{\partial u_e(\xi, t)}{\partial \xi} \right] = V_e(\xi, t) \tag{A.12}$$

where I_{e_y} is the cross-sectional area moment of inertia about the Y axis, A_e the

cross section area, κ_e the shear constant that depends on the shape of the cross section of the beam and G_e is the shear modulus, with $G_e = E_e/2(1+\nu_e)$, where ν_e is Poisson's ratio. This shear constant compensates the model assumption that a plane section remains plane after displacement. For circular solid shaft shear constant may be given by A.13 (FRISWELL [13]).

$$\kappa_e = \frac{6(1+\nu_e)}{(7+6\nu_e)} \tag{A.13}$$

The moment balance for the element shown in fig. A.2 yields

$$\rho_e I_{e_y} d\xi \frac{\partial^2 \psi_e(\xi,t)}{\partial t^2} = \left[M_{e_y}(\xi,t) + \frac{\partial M_{e_y}(\xi,t)}{\partial \xi} d\xi \right] - M_{e_y}(\xi,t) - \left[V_e(\xi,t) + \frac{\partial V_e(\xi,t)}{\partial \xi} d\xi \right] d\xi \tag{A.14}$$

For a symmetric element ($I_{e_y} = I_{e_x} = I_e$) the substitution of eq. (A.11) and eq. (A.12) into eq. (A.14) and neglecting inertia terms yields

$$\frac{\partial}{\partial \xi}\left(E_e I_e(\xi) \frac{\partial \psi_e(\xi,t)}{\partial \xi} \right) = \kappa_e G_e A_e \beta_e(\xi,t) \tag{A.15}$$

Shape function

In order to find suitable shape functions which relate the degrees of freedom $u_{e1}(t)$, $\psi_{e1}(t)$, $u_{e2}(t)$, $\psi_{e2}(t)$ shown in fig. A.3 the lateral displacement, u_e, is assumed to be cubic (FRISWELL [13]) and hence

$$u_e(\xi,t) = a_o(t) + a_1(t)\xi + a_2(t)\xi^2 + a_3(t)\xi^3 \tag{A.16}$$

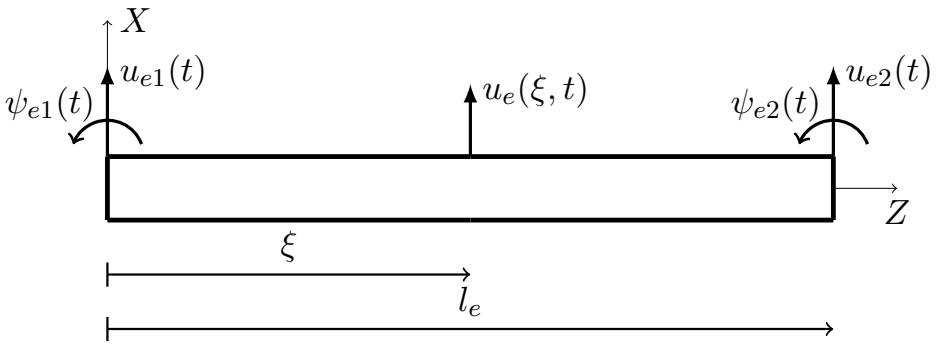

Figure A.3: Local coordinates for beam element at plane XZ.

The substitution of eq. (A.10) into eq. (A.15) from Timoshenko beam theory and the assumption of an uniform element cross section yields

$$\frac{\partial^3 u_e(\xi,t)}{\partial \xi^3} + \frac{\partial^2 \beta_e(\xi,t)}{\partial \xi^2} = \frac{\kappa_e G_e A_e}{E_e I_e}\beta_e(\xi,t) \tag{A.17}$$

The polynomyal in eq. (A.16) is applied to the beam moment equilibrium eq. (A.17) which yields

$$6a_3(t)\xi + \frac{\partial^2 \beta_e(\xi,t)}{\partial \xi^2} = \frac{\kappa_e G_e A_e}{E_e I_e}\beta_e(\xi,t) \tag{A.18}$$

For a constant shear angle across the element, i.e, $\partial\beta_e/\partial\xi = 0$ yields

$$\beta_e(\xi,t) = \frac{6E_eI_e}{k_eA_eG_e}a_3(t) = \frac{E_eI_e}{k_eA_eG_e}\frac{\partial^3 u_e(\xi,t)}{\partial \xi^3} \tag{A.19}$$

$$= \frac{\Phi_e l_e^2}{12}\frac{\partial^3 u_e(\xi,t)}{\partial \xi^3} \tag{A.20}$$

where

$$\Phi_e = \frac{12E_eI_e}{\kappa_eG_eA_el_e^2} \tag{A.21}$$

The degrees of freedom $u_{e1}(t)$, $\psi_{e1}(t)$, $u_{e2}(t)$, $\psi_{e2}(t)$ shown in fig. A.3 provide the boundary conditions:

$$u_{e1}(t) = u_e(0,t) \tag{A.22}$$

$$u_{e2}(t) = u_e(l_e,t) \tag{A.23}$$

$$\psi_{e1}(t) = \left.\frac{\partial u_e}{\partial \xi}\right|_{\xi=0} + \beta_e(0,t) \tag{A.24}$$

$$\psi_{e2}(t) = \left.\frac{\partial u_e}{\partial \xi}\right|_{\xi=l_e} + \beta_e(l_e,t) \tag{A.25}$$

$$\tag{A.26}$$

Substitutions of shear angle in eq. (A.20) and the polynomyal in eq. (A.16) into boundary conditions eq. (A.22), eq. (A.23), eq. (A.24) and eq. (A.25) yields

$$u_{e1}(t) = a_0(t) \tag{A.27}$$

$$u_{e2}(t) = a_0(t) + a_1(t)l_e + a_2(t)l_e^2 + a_3(t)l_e^3 \tag{A.28}$$

$$\psi_{e1}(t) = a_1(t) + a_3(t)\frac{\Phi_e l_e^2}{2} \tag{A.29}$$

$$\psi_{e2} = a_1(t) + 2a_2(t)l_e + a_3(t)\left(3l_e^2 + \frac{\Phi_e l_3^2}{2}\right) \tag{A.30}$$

The solution of eq. (A.27), eq. (A.28), eq. (A.29) and eq. (A.30) for $a_i(t)$ gives $a_i = a_i(u_{e1}(t), u_{e2}(t), \psi_{e1}(t), \psi_{e2}(t), \phi, l_e)$.

The substitution of a_i back into eq. (A.16) yields

$$\mathbf{u}_e(\xi, t) = [N_{e1}(\xi)N_{e2}(\xi)N_{e3}(\xi)N_{e4}(\xi)] \begin{bmatrix} u_{e1}(t) \\ \psi_{e1}(t) \\ u_{e2}(t) \\ \psi_{e2}(t) \end{bmatrix} \tag{A.31}$$

where the shape functions are

$$N_{e1}(\xi) = \frac{1}{1+\Phi_e}\left(1 + \Phi_e - \Phi_e\frac{\xi}{l_e} - 3\frac{\xi^2}{l_e^2} + 2\frac{\xi^3}{l_e^3}\right) \tag{A.32}$$

$$N_{e2}(\xi) = \frac{l_e}{1+\Phi_e}\left(\frac{2+\Phi_e}{2}\frac{\xi}{l_e} - \frac{4+\Phi_e}{2}\frac{\xi^2}{l_e^2} + \frac{\xi^3}{l_e^3}\right) \tag{A.33}$$

$$N_{e3}(\xi) = \frac{1}{1+\Phi_e}\left(\Phi_e\frac{\xi}{l_e} + 3\frac{\xi^2}{l_e^2} - 2\frac{\xi^3}{l_e^3}\right) \tag{A.34}$$

$$N_{e4}(\xi) = \frac{l_e}{1+\Phi_e}\left(-\frac{\Phi_e}{2}\frac{\xi}{l_e} - \frac{2-\Phi_e}{2}\frac{\xi^2}{l_e^2} + \frac{\xi^3}{l_e^3}\right) \tag{A.35}$$

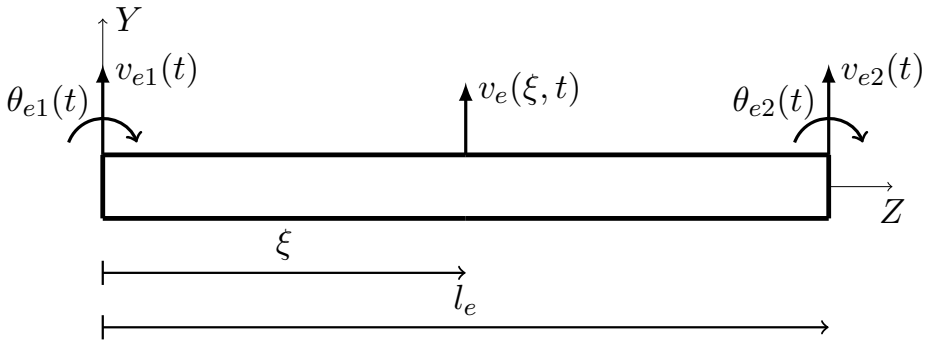

Figure A.4: Local coordinates for beam element at plane YZ.

Figure A.4 shows the degrees of freedom $v_{e1}(t)$, $\theta_{e1}(t)$, $v_{e2}(t)$, $\theta_{e2}(t)$ for the YZ plane. Since nodal rotations in this plane are clockwise the shape functions become:

$$\mathbf{v}_e(\xi, t) = [P_{e1}(\xi)P_{e2}(\xi)P_{e3}(\xi)P_{e4}(\xi)] \begin{bmatrix} v_{e1}(t) \\ \theta_{e1}(t) \\ v_{e2}(t) \\ \theta_{e2}(t) \end{bmatrix} \tag{A.36}$$

where

$$P_{e1}(\xi) = N_{e1}(\xi) \tag{A.37}$$
$$P_{e2}(\xi) = -N_{e2}(\xi) \tag{A.38}$$
$$P_{e3}(\xi) = N_{e3}(\xi) \tag{A.39}$$
$$P_{e4}(\xi) = -N_{e4}(\xi) \tag{A.40}$$

In order to simplify the notation, both displacements may be written as

$$u_e(\xi, t) = N_e(\xi)\mathbf{q}_{e_u}(t) \tag{A.41}$$
$$v_e(\xi, t) = P_e(\xi)\mathbf{q}_{e_v}(t) \tag{A.42}$$

where $\mathbf{q}_{e_u}(t) = [u_{e1}(t)\ \psi_{e1}(t)\ u_{e2}(t)\ \psi_{e2}(t)]^T$ and $\mathbf{q}_{e_v}(t) = [v_{e1}(t)\ \theta_{e1}(t)\ v_{e2}(t)\ \theta_{e2}(t)]^T$.

Thus, the slopes across the element $d\xi$ become

$$\psi_e(\xi, t) = \frac{\partial u_e(\xi, t)}{\partial \xi} + \beta_e(\xi, t) \tag{A.43}$$
$$\theta_e(\xi, t) = -\frac{\partial v_e(\xi, t)}{\partial \xi} - \beta'_e(\xi, t) \tag{A.44}$$

where β'_e is the shear angle in YZ plane which yields:

$$\beta'_e(\xi, t) = \frac{\Phi_e l_e^2}{12}\frac{\partial^3 v_e(\xi, t)}{\partial \xi^3} \tag{A.45}$$

Substitutions of eq. (A.41), eq. (A.42), eq. (A.20) and eq. (A.45) into the slopes in eq. (A.43) and eq. (A.44) yields

$$\psi_e(\xi, t) = \frac{d\mathbf{N}_e(\xi)}{d\xi} \cdot \mathbf{q}_{e_u}(t) + \frac{\Phi_e l_e^2}{12}\frac{d^3\mathbf{N}_e(\xi)}{d\xi^3} \cdot \mathbf{q}_{e_u}(t) \tag{A.46}$$
$$\theta_e(\xi, t) = -\frac{d\mathbf{P}_e(\xi)}{d\xi} \cdot \mathbf{q}_{e_v}(t) - \frac{\Phi_e l_e^2}{12}\frac{d^3\mathbf{P}_e(\xi)}{d\xi^3} \cdot \mathbf{q}_{e_v}(t) \tag{A.47}$$

Strain energy

The strain energy for the element of a Timoshenko beam with symmetric and uniform cross-section along the Z axis is (LALANNE and FERRARIS [12])

$$U_e = \frac{1}{2}E_eI_e\int_0^{l_e}\left(\frac{\partial u_e(\xi,t)}{\partial\xi}\right)^2 d\xi + \frac{1}{2}\kappa_e^2 G_eA_e\int_0^{l_e}\beta_e^2(\xi,t)\,d\xi$$
$$+\frac{1}{2}E_eI_e\int_0^{l_e}\left(\frac{\partial v_e(\xi,t)}{\partial\xi}\right)^2 d\xi + \frac{1}{2}\kappa_e^2 G_eA_e\int_0^{l_e}\beta_e'^2(\xi,t)\,d\xi \tag{A.48}$$

where the first and fourth terms are the energy contribution due to normal stress; and the second and fourth terms (FRISWELL [13]) are due to shear stress, and β_e' which assumes the expression of β_e except from being a clockwise rotation at plane YZ.

Substitution of eq. (A.20) into eq. (A.48) becomes

$$U_e = \frac{1}{2}E_eI_e\int_0^{l_e}\left(\frac{\partial u_e(\xi,t)}{\partial\xi}\right)^2 d\xi + \frac{E_eI_e\Phi_el_e^2}{24}\int_0^{l_e}\left(\frac{\partial^3 u_e(\xi,t)}{\partial\xi^3}\right)^2 d\xi$$
$$+\frac{1}{2}E_eI_e\int_0^{l_e}\left(\frac{\partial v_e(\xi,t)}{\partial\xi}\right)^2 d\xi + \frac{E_eI_e\Phi_el_e^2}{24}\int_0^{l_e}\left(\frac{\partial^3 v_e(\xi,t)}{\partial\xi^3}\right)^2 d\xi \tag{A.49}$$

Thus, substitution of the notation eq. (A.41) and eq. (A.41) into eq. (A.49) yields

$$\begin{aligned} U_e = \frac{1}{2}E_eI_e\int_0^{l_e}\Bigg[&\mathbf{q}_{e_u}^T(t)\cdot\frac{d^2\mathbf{N}_e^T(\xi)}{d\xi^2}\cdot\frac{d^2\mathbf{N}_e(\xi)}{d\xi^2}\cdot\mathbf{q}_{e_u}(t)\\ &+\frac{\Phi_el_e^2}{12}\mathbf{q}_{e_u}^T(t)\cdot\frac{d^3\mathbf{N}_e^T(\xi)}{d\xi^3}\cdot\frac{d^3\mathbf{N}_e(\xi)}{d\xi^3}\cdot\mathbf{q}_{e_u}(t)\\ &+\mathbf{q}_{e_v}^T(t)\cdot\frac{d^2\mathbf{P}_e^T(\xi)}{d\xi^2}\cdot\frac{d^2\mathbf{P}_e(\xi)}{d\xi^2}\cdot\mathbf{q}_{e_v}(t)\\ &+\frac{\Phi_el_e^2}{12}\mathbf{q}_{e_v}^T(t)\cdot\frac{d^3\mathbf{P}_e^T(\xi)}{d\xi^3}\cdot\frac{d^3\mathbf{P}_e(\xi)}{d\xi^3}\cdot\mathbf{q}_{e_v}(t)\Bigg]d\xi \end{aligned} \tag{A.50}$$

Then, applying Lagrange's equations to strain energy in eq. (A.50):

$$\frac{d}{dt}\left(\frac{\partial U_e}{\partial \dot{q}_{e_i}}\right) - \frac{\partial U_e}{\partial q_{e_i}} = E_e I_e \int_0^{l_e} \Bigg[\Bigg(\frac{d^2\mathbf{N}_e^T(\xi)}{d\xi^2} \cdot \frac{d^2\mathbf{N}_e(\xi)}{d\xi^2} + \frac{\Phi_e l_e^2}{12} \frac{d^3\mathbf{N}_e^T(\xi)}{d\xi^3} \cdot \frac{d^3\mathbf{N}_e(\xi)}{d\xi^3} \Bigg) \cdot \mathbf{q}_{e_u}(t) + \Bigg(\frac{d^2\mathbf{P}_e^T(\xi)}{d\xi^2} \cdot \frac{d^2\mathbf{P}_e(\xi)}{d\xi^2} + \frac{\Phi_e l_e^2}{12} \frac{d^3\mathbf{P}_e^T(\xi)}{d\xi^3} \cdot \frac{d^3\mathbf{P}_e(\xi)}{d\xi^3} \Bigg) \cdot \mathbf{q}_{e_v}(t) \Bigg] d\xi = \mathbf{K}_e \mathbf{q}_e \tag{A.51}$$

where $\mathbf{K}_e$ is the stiffness for the displacement vector $\mathbf{q}_e = [u_{e1}(t)\ v_{e1}(t)\ \theta_{e1}(t)\ \psi_{e1}(t)\ u_{e2}(t)\ v_{e2}(t)\ \theta_{e2}(t)\ \psi_{e2}(t)]^T$.

Since the shape functions $\mathbf{P}_e$ differs from $\mathbf{N}_e$ in the second and third elements due to the opposite sense of the angles θ_{e1} and θ_{e2} in the YZ plane to the angles ψ_{e1} and ψ_{e2} in the XZ plane the stiffness matrix is:

$$\mathbf{K}_e = \begin{bmatrix} K_{u_{11}} & 0 & 0 & K_{u_{12}} & K_{u_{13}} & 0 & 0 & K_{u_{14}} \\ 0 & K_{u_{11}} & -K_{u_{12}} & 0 & 0 & K_{u_{13}} & -K_{u_{14}} & 0 \\ 0 & -K_{u_{21}} & K_{u_{22}} & 0 & 0 & -K_{u_{23}} & K_{u_{24}} & 0 \\ K_{u_{21}} & 0 & 0 & K_{u_{22}} & K_{u_{23}} & 0 & 0 & K_{u_{24}} \\ K_{u_{31}} & 0 & 0 & K_{u_{32}} & K_{u_{33}} & 0 & 0 & K_{u_{34}} \\ 0 & K_{u_{31}} & -K_{u_{32}} & 0 & 0 & K_{u_{33}} & -K_{u_{34}} & 0 \\ 0 & -K_{u_{41}} & K_{u_{42}} & 0 & 0 & -K_{u_{43}} & K_{u_{44}} & 0 \\ K_{u_{41}} & 0 & 0 & K_{u_{42}} & K_{u_{43}} & 0 & 0 & K_{u_{44}} \end{bmatrix} \tag{A.52}$$

where the elements for the stiffness matrix are

$$K_{u_{ij}} = E_e I_e \int_0^{l_e} \left[\frac{d^2 N_{ei}(\xi)}{d\xi^2} \frac{d^2 N_{ej}(\xi)}{d\xi^2} + \frac{E_e I_e \Phi_e l_e^2}{12} \frac{d^3 N_{ei}(\xi)}{d\xi^3} \frac{d^3 N_{ej}(\xi)}{d\xi^3} \right] d\xi \tag{A.53}$$

The solution of each integral in eq. (A.53) yields the stiffness matrix

$$\mathbf{K}_e = \frac{E_e I_e}{(1+\Phi_e) l_e^3} \begin{bmatrix} 12 & 0 & 0 & 6l_E & -12 & 0 & 0 & 6l_e \\ 0 & 12 & -6l_e & 0 & 0 & -12 & -6l_e & 0 \\ 0 & -6l_e & l_e^2(4+\Phi_e) & 0 & 0 & 6l_e & l_e^2(2-\Phi_e) & 0 \\ 6l_e & 0 & 0 & l_e^2(4+\Phi_e) & -6l_e & 0 & 0 & l_e^2(2-\Phi_e) \\ -12 & 0 & 0 & -6l_e & 12 & 0 & 0 & -6l_e \\ 0 & -12 & 6l_e & 0 & 0 & 12 & 6l_e & 0 \\ 0 & -6l_e & l_e^2(2-\Phi_e) & 0 & 0 & 6l_e & l_e^2(4+\Phi_e) & 0 \\ 6l_e & 0 & 0 & l_e^2(2-\Phi_e) & -6l_e & 0 & 0 & l_e^2(4+\Phi_e) \end{bmatrix} \tag{A.54}$$

Kinetic energy

The kinetic energy for a Timoshenko beam element is similar to the disk in eq. (A.6). It applies a translational term, rotary inertia, a constant term and a gyroscopic as shown in eq. (A.55)

$$T_{Se} = \frac{\rho_e A_e}{2} \int_0^{l_e} (\dot{u}_e^2 + \dot{v}_e^2) d\xi + \frac{\rho_e I_e}{2} \int_0^{l_e} (\dot{\psi}_e^2 + \dot{\theta}_e^2) d\xi + \rho_e I_e l_e \Omega^2 - 2\rho_e I_e \Omega \int_0^{l_e} \dot{\psi}_e \theta_e d\xi \tag{A.55}$$

Substitutions of displacements and slopes along the element $d\xi$ in eq. (A.41), eq. (A.42), eq. (A.46) and eq. (A.47) into the translational, rotary inertia and the constant term in eq. (A.55) yields:

$$\begin{aligned} T_{Se} =& \frac{\rho_e A_e}{2} \int_0^{l_e} \left[\dot{\mathbf{q}}_{e_u}^T(t) \cdot \mathbf{N}_e^T(\xi) \cdot \mathbf{N}_e(\xi) \cdot \dot{\mathbf{q}}_{e_u}(t) + \dot{\mathbf{q}}_{e_v}^T(t) \cdot \mathbf{P}_e^T(\xi) \cdot \mathbf{P}_e(\xi) \cdot \dot{\mathbf{q}}_{e_v}(t) \right] d\xi \\ &+ \frac{\rho_e I_e}{2} \int_0^{l_e} \left[\dot{\mathbf{q}}_{e_u}^T(t) \cdot \left(\frac{d\mathbf{N}_e(\xi)}{d\xi} + \frac{\Phi_e l_e^2}{12} \frac{d^3\mathbf{N}_e(\xi)}{d\xi^3} \right)^T \cdot \left(\frac{d\mathbf{N}_e(\xi)}{d\xi} + \frac{\Phi_e l_e^2}{12} \frac{d^3\mathbf{N}_e(\xi)}{d\xi^3} \right) \cdot \dot{\mathbf{q}}_{e_u}(t) \right] d\xi \\ &+ \frac{\rho_e I_e}{2} \int_0^{l_e} \left[\dot{\mathbf{q}}_{e_v}^T(t) \cdot \left(\frac{d\mathbf{P}_e(\xi)}{d\xi} + \frac{\Phi_e l_e^2}{12} \frac{d^3\mathbf{P}_e(\xi)}{d\xi^3} \right)^T \cdot \left(\frac{d\mathbf{P}_e(\xi)}{d\xi} + \frac{\Phi_e l_e^2}{12} \frac{d^3\mathbf{P}_e(\xi)}{d\xi^3} \right) \cdot \dot{\mathbf{q}}_{e_v}(t) \right] d\xi \\ &+ \rho_e I_e l_e \Omega^2 \end{aligned} \tag{A.56}$$

Notice that only gyroscopic effect is excluded from eq. (A.56).

Thus, applying Lagrange's equations to kinetic energy in eq. (A.56) yields:

$$\frac{d}{dt}\left(\frac{\partial T_{Se}}{\partial \dot{q}_{e_i}}\right) - \frac{\partial T_{Se}}{\partial q_{e_i}} = \int_0^{l_e} \Bigg[\rho_e A_e \mathbf{N}_e^T(\xi) \cdot \mathbf{N}_e(\xi) + \rho_e I_e \left(\frac{d\mathbf{N}_e(\xi)}{d\xi} + \frac{\Phi_e l_e^2}{12} \frac{d^3\mathbf{N}_e(\xi)}{d\xi^3} \right)^T \cdot \left(\frac{d\mathbf{N}_e(\xi)}{d\xi} + \frac{\Phi_e l_e^2}{12} \frac{d^3\mathbf{N}_e(\xi)}{d\xi^3} \right) \Bigg] d\xi \cdot \ddot{\mathbf{q}}_{e_u}(t)$$
$$+ \int_0^{l_e} \Bigg[\rho_e A_e \mathbf{P}_e^T(\xi) \cdot \mathbf{P}_e(\xi) + \rho_e I_e \left(\frac{d\mathbf{P}_e(\xi)}{d\xi} + \frac{\Phi_e l_e^2}{12} \frac{d^3\mathbf{P}_e(\xi)}{d\xi^3} \right)^T \cdot \left(\frac{d\mathbf{P}_e(\xi)}{d\xi} + \frac{\Phi_e l_e^2}{12} \frac{d^3\mathbf{P}_e(\xi)}{d\xi^3} \right) \Bigg] d\xi \cdot \ddot{\mathbf{q}}_{e_v}(t)$$
$$= \mathbf{M}_{e_u} \ddot{\mathbf{q}}_{e_u} + \mathbf{M}_{e_v} \ddot{\mathbf{q}}_{e_v}(t)$$
$$= \mathbf{M}_e \ddot{\mathbf{q}}_e(t) \tag{A.57}$$

where $\mathbf{M}_{e_u}$ is the stiffness for the displacement vector $\mathbf{q}_{e_u}$, $\mathbf{M}_{e_v}$ the stiffness for the displacement vector $\mathbf{q}_{e_v}$ and $\mathbf{M}_e$ is the stiffness for the displacement vector $\mathbf{q}_e = [u_{e1}(t)\ v_{e1}(t)\ \theta_{e1}(t)\ \psi_{e1}(t)\ u_{e2}(t)\ v_{e2}(t)\ \theta_{e2}(t)\ \psi_{e2}(t)]^T$.

Notice that the shape functions $\mathbf{P}_e$ differs from $\mathbf{N}_e$ in the second and third elements due to the opposite sense of the angles θ_{e1} and θ_{e2} (YZ plane) to the angles ψ_{e1} and ψ_{e2} (XZ plane). Therefore, the mass matrix is:

$$\mathbf{M}_e = \begin{bmatrix} M_{u_{11}} & 0 & 0 & M_{u_{12}} & M_{u_{13}} & 0 & 0 & M_{u_{14}} \\ 0 & M_{u_{11}} & -M_{u_{12}} & 0 & 0 & M_{u_{13}} & -M_{u_{14}} & 0 \\ 0 & -M_{u_{21}} & M_{u_{22}} & 0 & 0 & -M_{u_{23}} & M_{u_{24}} & 0 \\ M_{u_{21}} & 0 & 0 & M_{u_{22}} & M_{u_{23}} & 0 & 0 & M_{u_{24}} \\ M_{u_{31}} & 0 & 0 & M_{u_{32}} & M_{u_{33}} & 0 & 0 & M_{u_{34}} \\ 0 & M_{u_{31}} & -M_{u_{32}} & 0 & 0 & M_{u_{33}} & -M_{u_{34}} & 0 \\ 0 & -M_{u_{41}} & M_{u_{42}} & 0 & 0 & -M_{u_{43}} & M_{u_{44}} & 0 \\ M_{u_{41}} & 0 & 0 & M_{u_{42}} & M_{u_{43}} & 0 & 0 & M_{u_{44}} \end{bmatrix} \tag{A.58}$$

where the elements for the mass matrix are

$$M_{u_{ij}} = \int_0^{l_e} \left[\rho_e A_e N_{ei}(\xi) N_{ej}(\xi) + \rho_e I_e \left(\frac{dN_{ei}(\xi)}{d\xi} + \frac{\Phi_e l_e^2}{12} \frac{d^3 N_{ei}(\xi)}{d\xi^3} \right) \left(\frac{dN_{ej}(\xi)}{d\xi} + \frac{\Phi_e l_e^2}{12} \frac{d^3 N_{ej}(\xi)}{d\xi^3} \right) \right] d\xi \tag{A.59}$$

The solution of each integral in eq. (A.59) yields the mass matrix

$$\mathbf{M}_e = \frac{\rho_e A_e l_e}{840(1+\Phi_e)^2}\begin{bmatrix} m_1 & 0 & 0 & m_2 & m_3 & 0 & 0 & m_4 \\ 0 & m_1 & -m_2 & 0 & 0 & m_3 & -m_4 & 0 \\ 0 & -m_2 & m_5 & 0 & 0 & +m_4 & m_6 & 0 \\ m_2 & 0 & 0 & m_5 & -m_4 & 0 & 0 & m_6 \\ m_3 & 0 & 0 & -m_4 & m_1 & 0 & 0 & -m_2 \\ 0 & m_3 & m_4 & 0 & 0 & m_1 & m_2 & 0 \\ 0 & -m_4 & m_6 & 0 & 0 & m_2 & m_5 & 0 \\ m_4 & 0 & 0 & m_6 & -m_2 & 0 & 0 & m_5 \end{bmatrix}$$

$$+\frac{\rho_e I_e}{30(1+\Phi_e)^2 l_e}\begin{bmatrix} m_7 & 0 & 0 & m_8 & -m_7 & 0 & 0 & m_8 \\ 0 & m_7 & -m_8 & 0 & 0 & -m_7 & -m_8 & 0 \\ 0 & -m_8 & m_9 & 0 & 0 & m_8 & m_{10} & 0 \\ m_8 & 0 & 0 & m_9 & -m_8 & 0 & 0 & m_{10} \\ -m_7 & 0 & 0 & -m_8 & m_7 & 0 & 0 & -m_8 \\ 0 & -m_7 & m_8 & 0 & 0 & m_7 & m_8 & 0 \\ 0 & -m_8 & m_{10} & 0 & 0 & m_8 & m_9 & 0 \\ m_8 & 0 & 0 & m_{10} & -m_8 & 0 & 0 & m_9 \end{bmatrix} \tag{A.60}$$

where

$$m_1 = 312 + 588\Phi_e + 280\Phi_e^2 \tag{A.61}$$
$$m_2 = (44 + 77\Phi_e + 35\Phi_e^2)l_e \tag{A.62}$$
$$m_3 = 108 + 252\Phi_e + 140\Phi_e^2 \tag{A.63}$$
$$m_4 = -(26 + 63\Phi_e + 35\Phi_e^2)l_e \tag{A.64}$$
$$m_5 = (8 + 14\Phi_e + 7\Phi_e^2)l_e^2 \tag{A.65}$$
$$m_6 = -(6 + 14\Phi_e + 7\Phi_e^2)l_e^2 \tag{A.66}$$
$$m_7 = 36 \tag{A.67}$$
$$m_8 = (3 - 15\Phi_e)l_e \tag{A.68}$$
$$m_9 = (4 + 5\Phi_e + 10\Phi_e^2)l_e^2 \tag{A.69}$$
$$m_{10} = (-1 - 5\Phi_e + 5\Phi_e^2)l_e^2 \tag{A.70}$$

The increment in kinetic energy of the beam element due to gyroscopic effects is

$$T_{Ge} = -2\rho_e I_e \Omega \int_0^{l_e} \dot{\psi}_e \theta_e d\xi \tag{A.71}$$

which is the last term in eq. (A.55).

Substitutions of slopes along the element $d\xi$ in eq. (A.46) and eq. (A.47) into eq. (A.71) yields:

$$T_{Ge} = -2\rho_e I_e \Omega \int_0^{l_e} \left[\dot{\mathbf{q}}_{e_u}^T(t) \cdot \left(\frac{d\mathbf{N}_e(\xi)}{d\xi} + \frac{\Phi_e l_e^2}{12} \frac{d^3\mathbf{N}_e(\xi)}{d\xi^3} \right)^T \cdot (-1) \left(\frac{d\mathbf{P}_e(\xi)}{d\xi} + \frac{\Phi_e l_e^2}{12} \frac{d^3\mathbf{P}_e(\xi)}{d\xi^3} \right) \cdot \mathbf{q}_{e_v}(t) \right] d\xi \tag{A.72}$$

Then, from Lagrange's equations:

$$\begin{aligned}
\frac{d}{dt}\left(\frac{\partial T_{Ge}}{\partial \dot{\mathbf{q}}_e}\right) - \frac{\partial T_{Ge}}{\partial \mathbf{q}_e} =& 2\rho_e I_e \Omega \int_0^{l_e} \left(\frac{d\mathbf{N}_e(\xi)}{d\xi} + \frac{\Phi_e l_e^2}{12} \frac{d^3\mathbf{N}_e(\xi)}{d\xi^3} \right)^T \cdot \left(\frac{d\mathbf{P}_e(\xi)}{d\xi} + \frac{\Phi_e l_e^2}{12} \frac{d^3\mathbf{P}_e(\xi)}{d\xi^3} \right) d\xi \cdot \dot{\mathbf{q}}_{e_v}(t) \\
& - \dot{\mathbf{q}}_{e_u}^T(t) \cdot 2\rho_e I_e \Omega \int_0^{l_e} \left(\frac{d\mathbf{N}_e(\xi)}{d\xi} + \frac{\Phi_e l_e^2}{12} \frac{d^3\mathbf{N}_e(\xi)}{d\xi^3} \right)^T \cdot \left(\frac{d\mathbf{P}_e(\xi)}{d\xi} + \frac{\Phi_e l_e^2}{12} \frac{d^3\mathbf{P}_e(\xi)}{d\xi^3} \right) d\xi \\
=& \Omega \big(\mathbf{A} \cdot \dot{\mathbf{q}}_{e_v}(t) - \dot{\mathbf{q}}_{e_u}^T(t) \cdot \mathbf{A} \big) \\
=& \Omega \big(\mathbf{A} \cdot \dot{\mathbf{q}}_{e_v}(t) - \mathbf{A}^T \cdot \dot{\mathbf{q}}_{e_u}(t) \big) \\
=& \Omega \mathbf{G}_e \dot{\mathbf{q}}_e(t)
\end{aligned} \tag{A.73}$$

where $\mathbf{G}_e$ is the gyroscopic matrix and $\dot{\mathbf{q}}_e = [\dot{u}_{e1}(t)\ \dot{v}_{e1}(t)\ \dot{\theta}_{e1}(t)\ \dot{\psi}_{e1}(t)\ \dot{u}_{e2}(t)\ \dot{v}_{e2}(t)\ \dot{\theta}_{e2}(t)\ \dot{\psi}_{e2}(t)]^T$ and

$$A_{ij} = 2\rho_e I_e \int_0^{l_e} \left(\frac{dN_{ei}(\xi)}{d\xi} + \frac{\Phi_e l_e^2}{12} \frac{d^3N_{ei}(\xi)}{d\xi^3} \right) \left(\frac{dP_{ej}(\xi)}{d\xi} + \frac{\Phi_e l_e^2}{12} \frac{d^3P_{ej}(\xi)}{d\xi^3} \right) d\xi \tag{A.74}$$

The solution o each integral in eq. (A.74) yields the gyroscopic matrix:

$$\mathbf{G}_e = \frac{\rho_e I_e}{15(1+\Phi_e)^2 l_e} \begin{bmatrix} 0 & g_1 & -g_2 & 0 & 0 & -g_1 & -g_2 & 0 \\ -g_1 & 0 & 0 & -g_2 & g_1 & 0 & 0 & -g_2 \\ g_2 & 0 & 0 & g_3 & -g_2 & 0 & 0 & g_4 \\ 0 & g_2 & -g_3 & 0 & 0 & -g_2 & -g_4 & 0 \\ 0 & -g_1 & g_2 & 0 & 0 & g_1 & g_2 & 0 \\ g_1 & 0 & 0 & g_2 & -g_1 & 0 & 0 & g_2 \\ g_2 & 0 & 0 & g_4 & -g_2 & 0 & 0 & g_3 \\ 0 & g_2 & -g_4 & 0 & 0 & -g_2 & -g_3 & 0 \end{bmatrix} \tag{A.75}$$

where

$$g_1 = 36 \tag{A.76}$$

$$g_2 = (3 - 15\Phi_e)l_e \tag{A.77}$$

$$g_3 = (4 + 5\phi_e + 10\phi_e^2)l_e^2 \tag{A.78}$$

$$g_4 = (-1 - 5\phi_e + 5\phi_e^2)l_e^2 \tag{A.79}$$

$$\tag{A.80}$$

Appendix B

UQlab code

This appendix is a step-by-step for a reliability analysis done on this dissertation through UQlab software. The main code is written on Matlab as wells as the limit-state function whose code uses many functions and is not transcripted here.

1. The first step is to initialize UQLAB software.

```
% INITIALIZE THE UQLAB FRAMEWORK AND CLEAR THE WORKSPACE
clearvars
close all
clc
uqlab
```

2. Provide the limit-state function whose input are the random variables.

```
%COMPUTATIONAL MODEL
Model.mFile = 'rotordynamic_limit_state_function';
Model.isVectorized = false;
%Model.isVectorized = 1;
myModel = uq_createModel(Model);
```

3. Specify the probailistic density functions of the input variables of the limit-state function.

```
%PROBABILISTIC INPUT MODEL

% Specify the marginals.
Input.Marginals(1).Name = 'k';
Input.Marginals(1).Type = 'Uniform';
```

```
Input.Marginals(1).Parameters = [1 1.45];

Input.Marginals(2).Name = 'c';
Input.Marginals(2).Type = 'Uniform';
Input.Marginals(2).Parameters = [1 1.82];

% Create and add the resulting input object to UQLab
myInput = uq_createInput(Input);
```

4. Find a surrogate model when the limit-state function is implicit to the random variables.

```
% POLYNOMIAL CHAOS EXPANSION METAMODEL

metaopts.Type = 'Metamodel';
metaopts.MetaType = 'PCE';
metaopts.FullModel = myModel;

% Least-square calculation of the coefficients
metaopts.Method = 'OLS' ;

% Least-square methods allow for degree-adaptive calculation of the PCE
% coefficients based on the lowest Leave-One-Out cross-validation error (LOO e
metaopts.Degree = 3:15;

% Number of samples based on a latin hypercube sampling of the limit-state fun
metaopts.ExpDesign.NSamples = 500;
metaopts.ExpDesign.Sampling = 'LHS';

% Create and add the OLS-based PCE model to UQLab
myPCE_OLS = uq_createModel(metaopts);

% Print a summary of the calculated coefficients and display %them
% graphically:
uq_print(myPCE_OLS);
uq_display(myPCE_OLS);
```

5. Use the surrogate model to run the First-Order Reliability Method.

```
% FORM
```

```
%  Select the reliability tool
FORMOptions.Type = 'Reliability';
FORMOptions.Method = 'FORM';

%  Run the FORM analysis
FORMAnalysis = uq_createAnalysis(FORMOptions);

%  Print out a report of the results
uq_print(FORMAnalysis);

%  Create a graphical representation of the results
uq_display(FORMAnalysis);
```

6. Set up the original limit-state function as the model to run the Importance Sampling analysis.

```
% COMPUTATIONAL MODEL
Model.mFile = 'rotordynamic_limit_state_function';
Model.isVectorized = false;
myModel = uq_createModel(Model);
```

7. Specify the probailistic density functions of the input variables of the limit-state function.

```
%PROBABILISTIC INPUT MODEL

Input.Marginals(1).Name = 'k';
Input.Marginals(1).Type = 'Uniform';
Input.Marginals(1).Parameters = [1 1.45];

Input.Marginals(2).Name = 'c';
Input.Marginals(2).Type = 'Uniform';
Input.Marginals(2).Parameters = [1 1.82];

% Create and add the resulting input object to UQLab
myInput = uq_createInput(Input);
```

8. Select and run an Importance Sampling Analysis.

```
ISOptions.Type = 'Reliability';
ISOptions.Method = 'IS';
ISOptions.IS.FORM = FORMResults;

% Run the Importance Sampling analysis
ISAnalysis = uq_createAnalysis(ISOptions);

%  Print on the screen a report of the results
ISAnalysis.Results.FORM.Ustar;
uq_print(ISAnalysis);

%  Create a graphical representation of the results
uq_display(ISAnalysis);
```